



Forschungszentrum Karlsruhe
in der Helmholtz-Gemeinschaft

Wissenschaftliche Berichte
FZKA 7205

Nonequilibrium Processing of Amorphous and Nanostructured Materials

G. P. Dinda
Institut für Nanotechnologie

März 2006

Forschungszentrum Karlsruhe
in der Helmholtz–Gemeinschaft

Wissenschaftliche Berichte
FZKA 7205

Nonequilibrium Processing of Amorphous
and Nanostructured Materials

Guru Prasad Dinda

Institut für Nanotechnologie

von der der Naturwissenschaftlich–Technischen Fakultät
der Universität des Saarlandes
genehmigte Dissertation

Forschungszentrum Karlsruhe GmbH, Karlsruhe
2006

Für diesen Bericht behalten wir uns alle Rechte vor

Forschungszentrum Karlsruhe GmbH
Postfach 3640, 76021 Karlsruhe

Mitglied der Hermann von Helmholtz-Gemeinschaft
Deutscher Forschungszentren (HGF)

ISSN 0947-8620

urn:nbn:de:0005-072055

Nonequilibrium Processing of Amorphous and Nanostructured Materials

*(Prozessieren von amorphen und nanokristallinen
Materialien fern vom thermodynamischen Gleichgewicht)*



Dissertation

**zur Erlangung des Grades
des Doktors der Naturwissenschaften
der Naturwissenschaftlich– Technischen Fakultät
der Universität des Saarlandes**

von

Guru Prasad Dinda

aus Kolkata, Indien

**Universität des Saarlandes
und
Forschungszentrum Karlsruhe, Institut für Nanotechnologie**

2006

Eidesstattliche Erklärung

Hiermit versichere ich an Eides statt, dass ich die vorliegende Arbeit selbständig und ohne Benutzung anderer als der angegebenen Hilfsmittel angefertigt habe. Die aus anderen Quellen oder indirekt übernommenen Daten und Konzepte sind unter Angabe der Quelle gekennzeichnet.

Die Arbeit wurde bisher weder im In- noch im Ausland in gleicher oder ähnlicher Form in einem Verfahren zur Erlangung eines akademischen Grades vorgelegt.

Saarbrücken, den 17.10.2005

Tag des Kolloquiums: 10. Januar 2006

Dekan: Univ.-Prof. Dr. rer. nat. Thomas Wichert

Prüfungsausschuss:

Vorsitzender: Univ.-Prof. Dr. rer. nat. Heiko Rieger
1. Berichterstatter: Priv.-Doz. Dr.-Ing. Jörg Weissmüller
2. Berichterstatter: Univ.-Prof. Dr. rer. nat. Uwe Hartmann
Akad. Mitarbeiter: Dr. rer. nat. Patrick Huber

Abstract

Nanostructured materials have attracted great interest in recent years because of the unusual mechanical, electrical and optical properties endowed by confining the dimensions of such materials and because of the combination of bulk and surface properties to the overall behaviour. There is continued interest in finding cost effective and simpler ways to fabricate nanostructured materials, even though research groups have been investigating possibilities for the past three decades. Here we describe a simple but very useful approach – so-called repeated cold-rolling – to synthesize large quantities of nanostructured materials at ambient temperature.

In the present work, massive nanocrystalline samples of Ti, Zr and Pd with average grain sizes below 100 nm and Ni with a grain size less than 10 nm have been synthesized at ambient temperature by repeated cold-rolling. Such small grain sizes have not been obtained for pure metals by any other severe plastic deformation technique. The development of the microstructure in dependence of deformation was investigated by X-ray diffraction, followed by the characterization of their morphology in cross section by scanning electron microscopy and transmission electron microscopy and the grain refinement mechanisms were analyzed. The mechanical responses of the nanostructured materials produced by repeated cold-rolling are studied by nanoindentation and Vickers hardness test. The highest hardness was observed for severely cold-rolled Ni of grain sizes less than 50 nm.

Aside from the opportunity to obtain nanocrystalline bulk samples, the processing pathway also allows for synthesizing bulk amorphous materials. Since the discovery of solid state amorphization reactions, mechanical alloying processes have been extensively investigated. However, the exact mechanisms of mechanically induced amorphization are not yet firmly established. By repeated cold-rolling, we were able to synthesize fully amorphous samples of different binary Cu-Zr, Cu-Ti, Ni-Zr, ternary Ti-Zr-Cu and quaternary Ti-Zr-Cu-Ni and Zr-Al-Cu-Ni alloy systems at ambient temperature starting from pure elemental foils. The key issue to synthesize fully amorphous samples by repeated cold-rolling are discussed. In addition, the progress of the solid state amorphization reaction and especially the early stages of phase formation at internal heterophase interfaces are studied systematically. In addition to the analyses of the amorphization mechanism, the present results indicate that repeated cold-rolling is a useful technique to obtain large quantities of amorphous samples over an extended range of glass forming composition.

Prozessieren von amorphen und nanokristallinen Materialien fern vom thermodynamischen Gleichgewicht

Zusammenfassung

Nanostrukturierte Materialien haben in den vergangenen Jahren aufgrund ihrer ungewöhnlichen mechanischen, elektrischen und optischen Eigenschaften ein weltweites, großes Interesse hervorgerufen. Die ungewöhnlichen Eigenschaften sind eng mit der räumlichen Beschränkung in einer oder mehrerer Dimensionen oder mit der Verknüpfung von Volumen- und Grenzflächeneigenschaften verbunden. In diesem Zusammenhang besteht ein fortgesetztes und bislang nicht befriedigtes Interesse an der Entwicklung kostengünstiger und einfach zu handhabender Methoden zur Herstellung nanokristalliner Materialien. Hier beschreiben wir einen neuartigen und einfachen jedoch gleichzeitig sehr wirkungsvollen Ansatz – das sogenannte „wiederholte Kaltwalzen“ – um massive nanokristalline Materialien bei Raumtemperatur und in Mengen im Gramm-Bereich herzustellen.

In dieser Arbeit wurden die reinen Metalle Ti, Zr und Pd mit einer mittleren Korngröße unter 100 nm und Ni sogar mit einer Korngröße unter 10 nm hergestellt. Derartig geringe Korngrößen konnten für diese reinen Metalle mit keiner anderen Deformationsmethode hergestellt werden. Die Entwicklung der Mikrostruktur als Funktion des Verformungsgrades wurde mit Röntgendiffraktion, Raster- und Transmissionselektronenmikroskopie in Aufsicht und im Querschnitt untersucht. Die Bildung einer nanokristallinen Mikrostruktur während der intensiven Walzverformung wird durch Versetzungsgeneration und durch Anordnung der Versetzungen zu Zell- oder Subkorn Grenzen und nachfolgende Ausbildung von Korngrenzen erklärt. Die weitere Deformation wird dann – mit abnehmender Korngröße – zunehmend durch alternative Deformationsmechanismen wie Kornrotation oder Korngrenzgleiten getragen. Die vorliegenden Ergebnisse zeigen darüber hinaus an, dass eine große plastische Dehnung und nicht notwendigerweise ein hoher hydrostatischer Druck wie bei der Hochdruck-Torsionsverformung zur Synthese nanokristalliner Mikrostrukturen notwendig ist. Dabei gilt einfach, dass umso mehr Korngrenzen gebildet werden können, je mehr Versetzungen durch plastische Verformung gebildet werden. Dieser Mechanismus und damit die minimale Korngröße ist begrenzt einerseits durch die minimale Kristallitgröße, welche noch eine Versetzung aufnehmen kann, und andererseits durch dynamische Erholung und Vergrößerung während der kontinuierlichen Deformation. Diese Analyse wird gestützt durch Verformungsexperimente an Zr bei Temperaturen deutlich unterhalb von Raumtemperatur. Bei tiefen Temperaturen läuft

die Erholung und Vergrößerung der Mikrostruktur mit verringerter Geschwindigkeit ab, so dass die Versetzungsdichte erhöht ist. Daher benötigt die Korngrößenverkleinerung bei tiefer Temperatur geringere Dehnungen. Dieses Ergebnis weist darauf hin, dass Synthesewege, welche bei niedrigen Temperaturen große Dehnungen in ein Material eintragen können, eine effiziente Option zur Herstellung nanokristalliner Materialien in anwendungsrelevanten Mengen darstellen können. Zusätzlich bietet die sequentielle Kombination unterschiedlicher Deformationsprozesse alternative und noch weitgehend unerforschte Möglichkeiten zur Nanostrukturbildung. Dabei zeigen bereits die hier erhaltenen ersten Ergebnisse hinsichtlich der mechanischen Eigenschaften von nanokristallinem Ni eine enorme Verbesserung aufgrund der Kornverkleinerung. Das hier hergestellte Ni beispielsweise zeigt die höchste jemals für Ni gemessene Härte von 7 GPa.

Neben der Möglichkeit zur Erzeugung massiver nanokristalliner Materialien kann die hier entwickelte Synthesemethode auch zusätzlich zur Festkörperamorphisierung benutzt werden. Dieser Ansatz bietet den Vorteil, dass die Geometrie der Schichten und damit der interessierenden Heterophasen-Grenzflächen deutlich definierter sind als beim Kugelmahlen, und somit die Analyse der zugrundeliegenden Mechanismen erleichtert. Darüber hinaus läuft die Verformung hier mit vergleichbar geringen Dehnraten ab, so dass eine starke Erhöhung der Temperatur an den Grenzflächen – wie typischerweise für das Kugelmahlen beobachtet – hier vermieden wird. Hier wurden unterschiedliche binäre, ternäre und quaternäre Systeme auf Zr – und Ti-Basis ausgehend von elementaren Folien durch intensive Deformation bei Raumtemperatur amorphisiert. Dabei trägt die Zwangsmischung von Legierungselementen und die dadurch erreichte Übersättigung den Hauptanteil der Amorphisierungsreaktion: wird die Übersättigung so weit erhöht, dass die Stabilitätsgrenze für polymorphe Umwandlungen überschritten wird, so wird die feste Lösung thermodynamisch instabil und kann unter Energiegewinn in eine metastabile, amorphe Phase umwandeln. Zusätzlich erschweren oder verhindern Konzentrationsgradienten an den Heterophasen-Grenzflächen die Nukleation der intermetallischen Konkurrenzphasen und erleichtern so die Amorphisierung. Dabei weisen die vorliegenden Ergebnisse darauf hin, dass die Zwangsmischung von Legierungselementen zur Erzielung hoher Übersättigungen durch die Erzeugung von „willkürlichen Gleitsystemen“ in den kristallinen Bereichen und durch Bildung von Scherbändern in der amorphen Phase kontrolliert wird, und nicht durch thermische Diffusionsprozesse allein zu erklären ist. Zu Beginn der Festkörperreaktion, bei geringen Dehnungen, bildet sich die amorphe Phase zunächst an den Heterophasen-Grenzflächen, sobald lokal die Übersättigung den kritischen Wert übersteigt. Diese amorphe Zwischenschicht wächst mit zunehmender Deformation durch mechanisches Mischen, Grenzflächenaufrauung und thermische Diffusion. Die experimentelle Beobachtung einer kontinuierlich und inkrementell wachsenden Dicke der amorphen Lage weist darauf hin, dass die Festkörperamorphisierung ähnlich wie eine konventionelle diffusionskontrollierte Phasenumwandlung abläuft, mit der Besonderheit, dass das Material vor der Wachstumsfront zuerst einen thermodynamisch instabilen Zustand annehmen muss, bevor die Umwandlung fortschreiten kann.

Contents

1	Introduction	1
2	The state of the art	3
2.1	Synthesis of nanostructured materials by severe plastic deformation	3
2.1.1	Introduction	3
2.1.2	High Pressure Torsion (HPT)	5
2.1.3	Equal Channel Angular Pressing (ECAP)	5
2.1.4	Continuous Confined Strip Shearing (C2S2)	6
2.2	Plastic deformation mechanisms of micro- and nano- crystalline materials	8
2.2.1	Deformation by slip	8
2.2.2	Deformation by twinning	9
2.2.3	Dislocation plasticity of microcrystalline materials	9
2.2.4	Deformation of nanocrystalline materials	9
2.2.5	Grain-boundary based deformation mechanisms: crossover from `normal' to `inverse' Hall-Petch behaviour	12
2.3	Mechanical alloying and solid-state amorphization	14
2.3.1	Introduction	14
2.3.2	Mechanically activated solid-state amorphization	15
2.3.3	Enhanced solid-state amorphization by sharp concentration gradients	19
3	Experimental Procedure	22
3.1	Repeated Cold-Rolling (Folding and Rolling)	22
3.2	Materials Selection	23
3.3	X-ray Diffraction (XRD)	24
3.4	Scanning Electron Microscopy (SEM)	24
3.5	Transmission Electron Microscopy (TEM)	25
3.6	Differential Scanning Calorimetry (DSC)	25
3.7	Setting up of a Rapid Thermal Annealing Furnace (RTA)	25
4	Nanostructured materials from repeated cold-rolling	27
4.1	Synthesis of nanocrystalline metals	27
4.1.1	Elemental Ni (fcc)	27
4.1.1.1	Sequential combination of SPD methods	34
4.1.1.2	The Hall-Petch plot of hardness of Ni	37
4.1.1.3	Thermal stability	38
4.1.2	Elemental Pd (fcc)	39
4.1.3	Elemental Ti (hcp) & Zr (hcp)	42
4.1.4	Cold-rolling of Zr at low (below -100°C) temperature	45
4.2	Discussion	47
4.2.1	Mechanisms for formation of nanocrystalline microstructures by repeated cold-rolling	48

4.3	Synthesis of nanocrystalline alloys	50
4.3.1	Grain refinement of Ni ₅₀ Ti ₅₀ elemental multilayers	50
4.3.2	Grain refinement of Ni ₅₀ Ti ₅₀ shape memory alloys	51
4.3.3	Discussion	53
4.4	Interface reaction between Al and Ni	53
5	Amorphous materials from repeated cold-rolling	58
5.1	Binary Cu-Zr elemental multilayer	58
5.2	Amorphous phase forming abilities of Binary, Ternary and Quaternary systems	62
5.3	Progress of solid-state amorphization reaction by repeater cold-rolling	64
5.4	Mechanical alloying processes	66
5.5	Suppression of crystal nucleation in amorphous layers with sharp concentration gradients	69
6	Summary and Outlook	71
A	Appendix	73
A.1	Estimation of the strain in High Pressure Torsion (HPT)	74
A.2	Estimation of the strain in Equal Channel Angular Pressing (ECAP)	74
A.3	Strain in the rolling and folding (F&R) process	75
	References	76

Chapter 1

Introduction

Nanoscience and nanotechnology deal with the making of objects that measure between 1 to 100 nanometers (nm) and with the study of their properties. These objects will serve as a basis for the development of high technology in the fields of advanced materials, microelectronics, electro-optics, medicine and more. Two ways can be used to reach the nanometre scale. Nanostructured materials are synthesized by either “bottom-up” or “top-down” processes [Hu et al. 1999]. The bottom-up approach starts with atoms, ions or molecules as “building blocks” and assembles nanoscale clusters or bulk materials from them. The “top-down” methods for processing of nanostructured materials involve starting with a bulk solid and obtaining a nanostructure by structural refinement. One such recently advanced approach is presented by so called Severe Plastic Deformation (SPD) which introduces defects, i.e. dislocations, into the materials which can then rearrange to attain a minimum energy configuration by forming a submicron cell/sub-grain structure. Of the variety of SPD methods, only ball milling and repeated cold rolling can produce nanostructured metals of average grain size below 100 nm.

In the last decade, various severe plastic deformation (SPD) processes have been proposed for ultra grain refinement, such as High Pressure Torsion (HPT) [Valiev et al. 1991], Equal Channel Angular Pressing (ECAP) [Valiev et al. 1993] etc. However, the grain sizes achieved so far through these routes for pure metals such as Cu, Ni, and Ti are actually outside the nanocrystalline regime, the grain sizes obtained still remain in the 150-350 nm range or more. This has been the motivation for this thesis to develop a simple but very versatile method (repeated cold-rolling) to synthesize nanostructured materials of grain size less than 100 nm in bulk quantities. In the present study, we found that massive nanocrystalline samples of Ti, Zr and Pd with average grain sizes well below 100 nm and Ni with grain sizes less than 10 nm can be synthesized at ambient temperature by repeated cold-rolling. The focus of this thesis is a systematic study of grain refinement processes at different stages of the deformation including the limiting minimum grain size achievable by repeated cold-rolling and the mechanical response of the nanostructured materials produced by repeated cold-rolling.

In principle, alloy formation by deformation-assisted mixing or alloy processing by continued shear deformation is well-known, e.g. from ball- milling of alloy powders or elemental powder blends. In this context, repeated cold rolling processing is attractive from a basic point of view, since the deformation is introduced in a controlled and rather well dosed way. Thus, deformation-enhanced mixing, interface roughening or amorphization can be studied in detail and at a high effective (strain-) resolution. Concerning the formation of bulk amorphous materials, the repeated cold rolling deformation can allow synthesizing massive bulk amorphous materials in alloy systems with only modest tendency for amorphization. Although mechanical alloying processes have been extensively investigated, the mechanism of solid state amorphization

reactions during the mechanical deformation process is not yet firmly established and especially the early stages of amorphization during mechanical alloying still call for more detailed investigations. This part of the research is primarily focused on investigating the progress of solid state reaction in different glass forming systems for a better understanding of the early stages of the crystal-to-amorphous transition during intense mechanical deformation.

Chapter 2

The state of the art

2.1 Synthesis of nanostructured materials by severe plastic deformation

2.1.1 Introduction

Nanostructured materials [Gleiter 2000], which can be defined as materials with crystallite sizes less than 100 nm in dimension, are of high interest concerning basic scientific issues that are related to the size-dependence of materials properties as well as with regard to technological applications due to their modified and often improved performance and unique property combinations, e.g. increased tensile strength and increased elongation to failure (ductility) at the same time [McFadden et al. 1999, Wang et al. 2002]. These size-dependent property modifications become more pronounced at smaller grain sizes. Thus, from a scientific point of view as well as concerning a further improvement of structural or functional properties, synthesizing material with an average grain diameter in the lower size range (i.e. $d < 20$ nm) is an important and timely issue. Moreover and especially with respect to applications, options for synthesizing massive bulk materials that consist of nanocrystalline grains need to be developed.

Several laboratory-scale processing techniques are currently available to produce nanocrystalline materials, i.e. materials with an average grain size less than 100 nm, and ultrafine-grained (average grain size in the 100–1000 nm range) materials. They can be generally classified into the following four groups: mechanical alloying and compaction [Koch 1997, Zhou et al. 2003], severe plastic deformation [Valiev et al. 1991, 1993], gas-phase condensation of particulates and consolidation [Gleiter 1989, Sanders et al. 1997], and electrodeposition [Erb 1995]. Whereas the first two methods typically tend to yield material with ultra-fine grain sizes, the latter two techniques are capable of producing material with mean grain sizes in the tens of nanometers (nm). A fifth technique which can, in principle, facilitate the production of a nanocrystalline (nc) alloy entails controlled crystallization of a material capable of forming an initially fully amorphous metallic glass, particularly if the metallic glass can be produced in bulk form. This approach is attractive for producing controlled two-phase microstructures [Wilde et al. 2003, He et al. 2003], but due to the nature of the process, the technique is limited to glass-forming compositions. With this approach, nanocrystallites can be formed either by controlled thermal annealing [Inoue et al. 1990, Peker et al. 1993] and/or by severe mechanical deformation at the bulk [He 1998] or local [Kim et al. 2002] level.

Gas-phase condensation or inert gas condensation [Gleiter 1989] has been used in a limited way to produce nanostructured materials such as Cu, Ni and Pd. Here, powder particles with grain size in the 5–50 nm regime are produced by condensing

from the vapor phase, and the particles are then consolidated in a die using high pressures and, in some cases, additional thermal energy. The process has several limitations including specimen volume and yield, purity issues particularly in the vicinity of the particle boundaries, incomplete densification/porosity (resulting in specimens with densities lower than 99% of the theoretical density), and difficulties associated with retaining the fine grain size during consolidation. The process, however, is capable of providing a microstructure that is usually texture-free and consisting of equiaxed grains. Recently it has been shown that the density of the specimens can be increased by cold rolling, while retaining the equiaxed, texture-free microstructure without a change in grain size [Markmann et al. 2003].

Electrodeposition (direct current and pulsed) has been used to produce sheets of nc metals (such as Ni, Co, Cu) and binary alloys (such as Ni-Fe, Ni-W) [El-Sharik et al. 1992, Lu et al. 2001]. The grain size can be controlled and sheets with thickness of 100 μm or more and grain size of 10–40 nm are routinely produced. Moreover, the grain size distribution in these materials often tends to be narrow with the maximum grain size not exceeding 80 nm for a material with a mean grain size of 20–30 nm [Dalla et al. 2002]. In recent years, more effort has been devoted to improving the synthesis of nc-metals by electrodeposition rather than by inert gas condensation/compaction, primarily because of the problems associated with attaining full density via the latter approach. Yet, the use of saccharin in the plating bath to produce nanocrystalline grains often results in carbon and sulphur as impurities in the material [Ebrahimi et al. 1999].

Unlike many of the above methods, mechanical attrition produces nanostructures not by cluster assembly but by the structural refinement of coarser-grained structures as the result of severe plastic deformation. The advantage of the process lies in its ability to produce reasonably sized billets of material. Similarly, the serious problems that are usually cited are (1) contamination from milling media and/or atmosphere, and (2) the need (for many applications) to consolidate the powder product without coarsening the nanocrystalline microstructure. In fact, the contamination problem is often given as a reason to dismiss the method- at least for some materials.

Some of the shortcomings associated with material purity can be offset by using the approach of severe plastic deformation (SPD) of bulk material (as, for example, via torsion, multiple extrusion or multiple forging) where material purity is limited only by that of the starting material. In the last decade, various SPD processes for achieving grain refinement have been developed, such as high-pressure torsion straining (HPT) or equal channel angular pressing (ECAP). These processes are characterized by a large strain that is applied on the material at a rather high strain rate of the order of 1s^{-1} or higher and the simultaneous application of a high hydrostatic pressure of the order of several GPa. Related processes such as the Conshearing Process [Saito et al. 2000] or Continuous Confined Strip Shearing (C2S2) [Lee et al. 2002] and ECAP-Conform [Raab et al. 2004] have been proposed for the production of metal strips in a continuous manner that would – at least in principle – allow an effective up-scaling. A comprehensive review by Valiev et al. [Valiev et al. 2000] discusses the various metallurgical aspects of materials produced by severe plastic deformation.

2.1.2 High Pressure Torsion (HPT)

Devices, where High Pressure Torsion (HPT) was conducted under high pressure, were first used in [Zhorin et al. 1984]. In the first work these devices were used for investigation of phase transformations during heavy deformation [Zhorin et al. 1984] as well as the evolution of the structure and changes in the temperature of recrystallization after large plastic deformations [Smirnova et al. 1986]. Successful formation of homogeneous nanostructures with high-angle grain boundaries via severe torsion straining [Valiev et al. 1991, 1993] was a very important step allowing one to consider this procedure as a new method for processing of nanostructured materials. A disk type sample with a thickness of 0.3 - 0.5 mm and the radius of 5 -15 mm is held between anvils and strained in torsion under the applied pressure of several GPa. A upper holder rotates and surface friction forces deform the sample by shear. Due to the specific geometric shape of the sample, the main volume of the material is strained in conditions of quasihydrostatic compression under the applied pressure. As a result, in spite of large strain values, the deformed sample is not destroyed. The minimum average grain size achieved by HPT for pure metals is around 150 to 350 nm. The true strain after one revolution of the sample having a thickness of 0.3 mm and the radius of 5 mm is 4.1 (See appendix A.1).

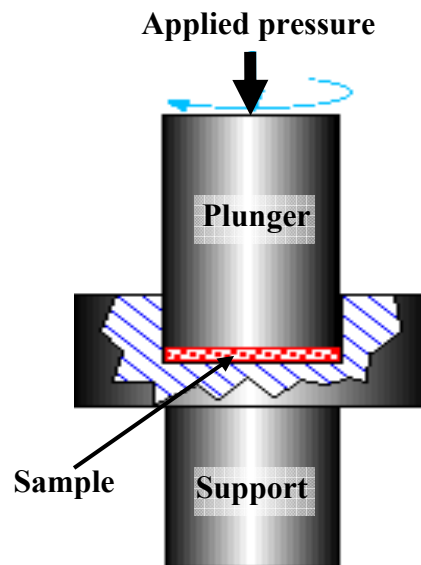


Figure 2.1: Schematic illustration of HPT processing.

2.1.3 Equal Channel Angular Pressing (ECAP)

Equal-channel angular pressing (ECAP) is a processing method in which a metal is subjected to an intense plastic straining through simple shear without any corresponding change in the cross-sectional dimensions of the sample. There are numerous well-established methods for subjecting metallic samples to an imposed strain, including through the standard industrial metal-working processes of rolling or extrusion, but all of these methods necessitate a change in the physical dimensions of the sample. In contrast, ECAP differs from these conventional procedures because the cross-sectional dimensions of the sample remain unchanged during straining.

Historically, ECAP was first developed in the Soviet Union almost twenty years ago [Segal et al. 1981] but the process has received significant interest in western countries only within the last six or seven years for processing of structures with submicron and nanometric grain sizes [Valiev et al. 2000]. The principle of ECAP is depicted schematically in Fig. 2.2. The ECAP die contains two channels, equal in cross-section, intersecting at an angle near the centre of the die. The angle can be chosen between 0 and 90 degrees to provide a varied amount of strain. The test sample is machined to fit within these channels and it is multiple pressed through the die using a plunger. Thus simple shear is imposed during the deformation at the intersection of the two channels. The true strain after one pass is around 0.8 (See appendix A.2).

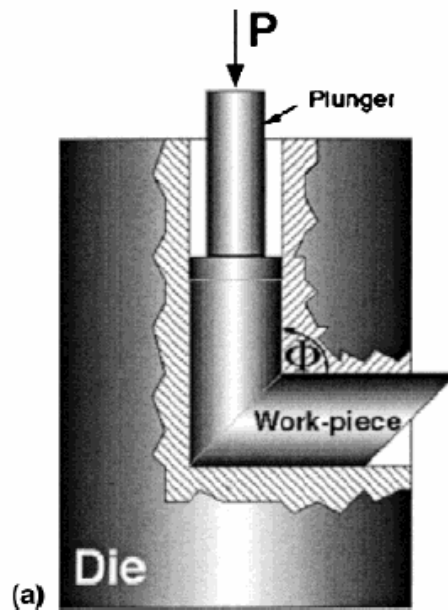


Figure 2.2: Schematic illustration of an ECAP process.

2.1.4 Continuous Confined Strip Shearing (C2S2)

The HPT or ECAP techniques are neither continuous nor can handle a long and thin workpiece, thereby acting as a major drawback for wider commercial applications of this process. If the ECAP process could be used for producing metallic strips in a continuous manner, it would be more useful to extend the concept of ECAP as a new forming technique for producing various metallic sheets with tailored properties in a large quantity. More recently, some modified SPD processes have been proposed based on the ECAP principle, such as Continuous Confined Strip Shearing (C2S2) [Lee et al. 2002] and ECAP-Conform [Raab et al. 2004] for the production of metal strips in a continuous manner. A schematic of the C2S2 machine is shown in Fig. 2.3. A specially designed feeding roll and a guide roll were used as a feeding apparatus. Feeding the workpiece using the feeding roll, instead of feeding the material using the ram of the hydraulic press, not only makes continuous operation possible but also allows the formation of various metal strips into the desired final dimensions. However, the grain sizes of C2S2 processed materials remain in the ultrafine-grained (100–1000 nm) regime.

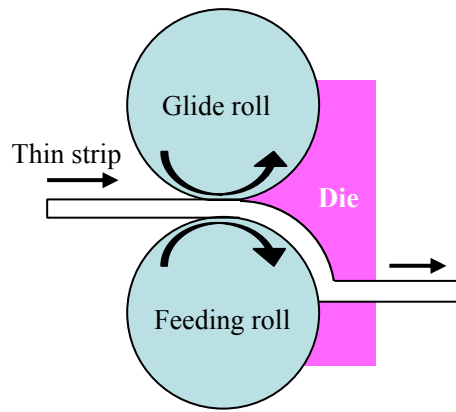


Figure 2.3: A schematic showing the C2S2 process based on the ECAP principle.

2.2 Plastic deformation mechanisms of micro- and nano- crystalline materials

2.2.1 Deformation by Slip

The usual method of plastic deformation in metals is by the sliding of blocks of the crystal over one another along definite crystallographic planes, called slip planes. Generally the slip plane is the plane of greatest atomic density and the slip direction is the closest-packed direction within the slip plane. Since the planes of greatest atomic density are also the most widely spaced planes in the crystal structure, the resistance to slip is generally less for these planes than for any other set of planes.

In the hexagonal close-packed metals (Fig. 2.4b), the only plane with high atomic density is the basal plane (0001). The axes $\langle 11\bar{2}0 \rangle$ are the close-packed directions. For zinc, cadmium, and cobalt slip occurs on the (0001) plane in the $\langle 11\bar{2}0 \rangle$ directions. However, zirconium and titanium, which have low c/a ratios, slip occurs primarily on the prism and pyramidal planes in the $\langle 11\bar{2}0 \rangle$ directions. Since there is only one basal plane per unit cell and three $\langle 11\bar{2}0 \rangle$ directions, the hcp structure possesses three slip systems. The limited number of slip systems is the reason for the extreme orientation dependence and low ductility in hcp crystals.

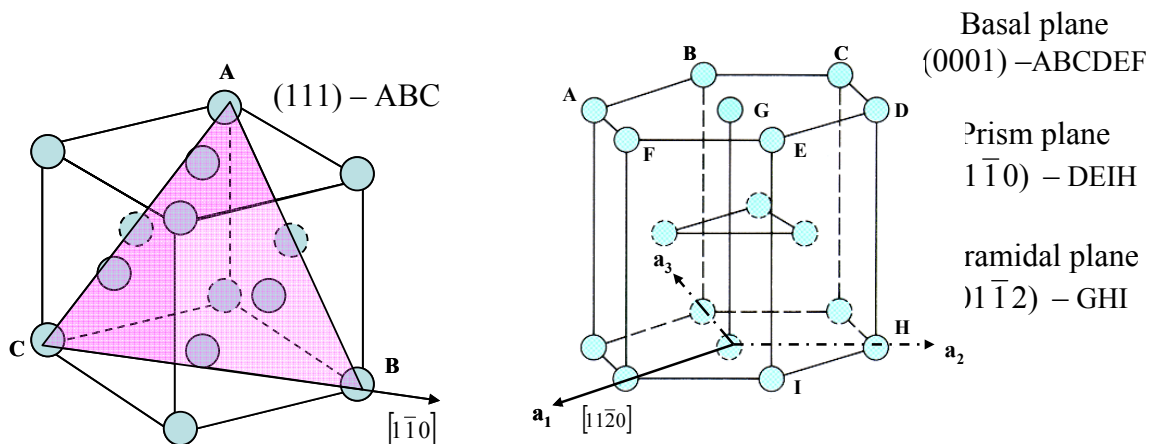


Figure 2.4: (a) Face-centered cubic structure; (b) Hexagonal close-packed structure.

In the face-centered cubic structure (Fig. 2.4a), the $\{111\}$ octahedral planes and the $\langle 110 \rangle$ directions are the close-packed systems. There are eight $\{111\}$ planes in the fcc unit cell. However, the planes at opposite faces of the octahedron are parallel to each other, so that there are only four sets of octahedral planes. Each $\{111\}$ plane contains three $\langle 110 \rangle$ directions. Therefore, the fcc lattice has 12 possible slip systems.

Slip in bcc metals is found to occur on the $\{110\}$, $\{112\}$, and $\{123\}$ planes, while the slip direction is always the $\langle 111 \rangle$ direction. There are 48 possible slip systems, but since the planes are not so close-packed as in the fcc structure, higher shearing stresses are usually required to cause slip.

2.2.2 Deformation by twinning

The second important mechanism by which metals deform is the process known as twinning. Twins may be produced by mechanical deformation or as the result of annealing following plastic deformation. However, twinning is not a dominant deformation mechanism in metals which possess many possible slip systems. Twinning generally occurs when the slip systems are restricted or when the critical resolved shear stress is increased so that the twinning stress is lower than the stress for slip. The lattice strains needed to produce a twin configuration in a crystal are small, so that the amount of gross deformation that can be produced by twinning is small. The important role of twinning in plastic deformation comes not from the strain produced by the twinning process but from the fact that orientation changes resulting from twinning may place new slip systems in a favorable orientation with respect to the stress axis so that additional slip can take place. Twins have been observed in conventional fcc metals and alloys with low stacking fault energy. Twins have also been observed in fcc metals and alloys with relatively high stacking fault energy when extreme deformation conditions are imposed (cryogenic temperatures, shock-loading).

2.2.3 Dislocation plasticity of microcrystalline materials

The common low-temperature plastic-deformation mechanism in coarse-grained materials involves the continuous nucleation of dislocations from Frank–Read sources and their glide through the crystal on well-defined slip systems. Dislocations can move through the crystal grains and can interact with each other. As the orientation changes at a grain boundary, the slip plane in a grain does not continue in the same direction beyond the boundary. So, dislocations gliding on a slip plane are unable to cross the boundary but get piled up against it. This happens more often in a fine grained materials. The yield strength σ_y of a polycrystalline materials is a function of its grain size as given by the Hall-Petch equation:

$$\sigma_y = \sigma_i + kd^{-1/2} \quad (2.1)$$

where σ_i is the yield strength at 'infinite' grain size, k is the Hall-Petch constant, and d is the mean grain diameter. Conventional dislocation mechanisms cease to function when the grain sizes are below a critical value. This is because the size of a Frank–Read source cannot exceed the grain size. Since the stress needed for their operation is inversely proportional to the size of the source, this deformation mechanism can operate only down to a grain size of typically about 1 μm . For smaller grain sizes, mobile dislocations must be nucleated from other sources, such as the grain boundaries or grain junctions.

2.2.4 Deformation of nanocrystalline materials

It is generally accepted that conventional dislocation sources such as the Frank-Read source cease to operate in nanocrystalline metals, and that grain boundaries become potential dislocation sources and sinks. For the larger grain sizes (of 50–1000 nm) deformation is dominated by dislocation processes and in the lower grain-size range (<20 nm) a GB-based deformation process takes over, leading to a reduction of

the yield and flow stress with decreasing grain size [Chokshi et al. 1989, Gertsman et al 1994] ; this phenomenon is known as the “inverse Hall–Petch effect”.

The most common dislocations responsible for the slip deformation of fcc metals are extended dislocations, their cores being split into two Shockley partials connected by a stacking fault. The length of the stacking fault, i.e., the dislocation splitting distance, r (the width of the stacking fault region between the partial dislocations), depends on the stacking-fault energy, Γ , and the resolved shear stress, σ , on the glide plane as [Hirth et al 1992]:

$$r = \frac{K_1 b^2}{(\Gamma - K_2 \sigma)} \quad (2.2)$$

where $b = a_0/\sqrt{6}$ is the length of the Burgers vector of the partials; K_1 and K_2 are numerical factors depending on the elastic constants of the material and the types of partials forming the extended dislocation. Under the high stress required to nucleate dislocations from the GBs, the magnitude of r can be significant and, for a nanocrystalline grain size become comparable to, or even larger than, the grain diameter d . Thus an extended (the combination of the two partials) dislocation cannot be nucleated unless the grain size, $d > r(\sigma)$. Simulations of fully 3D nanocrystalline-Al microstructures [Phillpot et al 1995] revealed the nucleation of complete $1/2[110]$ dislocations from the GBs and triple junctions, provided the grain size d is large enough ($d \geq 18$ nm). As d decreases below 18 nm, complete dislocations can no longer be nucleated, and only individual partials, travelling across the grains while leaving behind stacking faults transecting the grains, are observed. The requirement that $d > r(\sigma)$ represents a necessary condition for the dislocation-glide mechanism to be fully operational. When d becomes comparable to r only single partials can be nucleated, producing stacking faults in their glide through the grains. The interplay between $r(\sigma)$ and d thus results in a grain size below which the slip process becomes less and less effective in producing plastic strain and the GB based deformation starts to dominate. This suggests that a critical grain size, $d_c \sim r$, exists below which the material starts to soften due to the domination of a GB based deformation mechanism. From the MD simulations of Swygenhoven et al. (2002) and Shiotz et al. (1998), it appears that no dislocation activity exists below a critical grain size of 10 nm. Plastic deformation takes place entirely by means of grain boundary sliding. Grain boundaries are considered elastically softer than the grain interiors of nanocrystalline metals [Schiotz et al.1999]. Recently, Swygenhoven et al. (2004) have reported different possible deformation mechanisms of nanocrystalline materials by molecular dynamics simulations (see Fig. 2.5). In addition, Yamakov et al. (2004) have proposed (by molecular dynamics simulations) a deformation map for nanocrystalline metals using the splitting distance between two partial dislocations and the stacking fault energy, γ_{sf} , of the materials. According to this map, a strongest grain size exists for a given applied stress—namely, the grain size that corresponds to a cross-over between the normal and inverse Hall–Petch regimes. For high- γ_{sf} materials, this cross-over is at the transition from perfect slip to grain-boundary-mediated deformation, whereas in low- γ_{sf} materials, the deformation mechanism goes from slip via extended partial dislocations (a partial dislocation that transects the entire grain leaving behind a stacking fault defect) to grain-boundary-mediated processes, and the strongest size corresponds to a grain size that

equals the splitting distance between the partials at the resolved shear stress. It is also claimed that the strongest grain size increases with decreasing stacking fault energy.

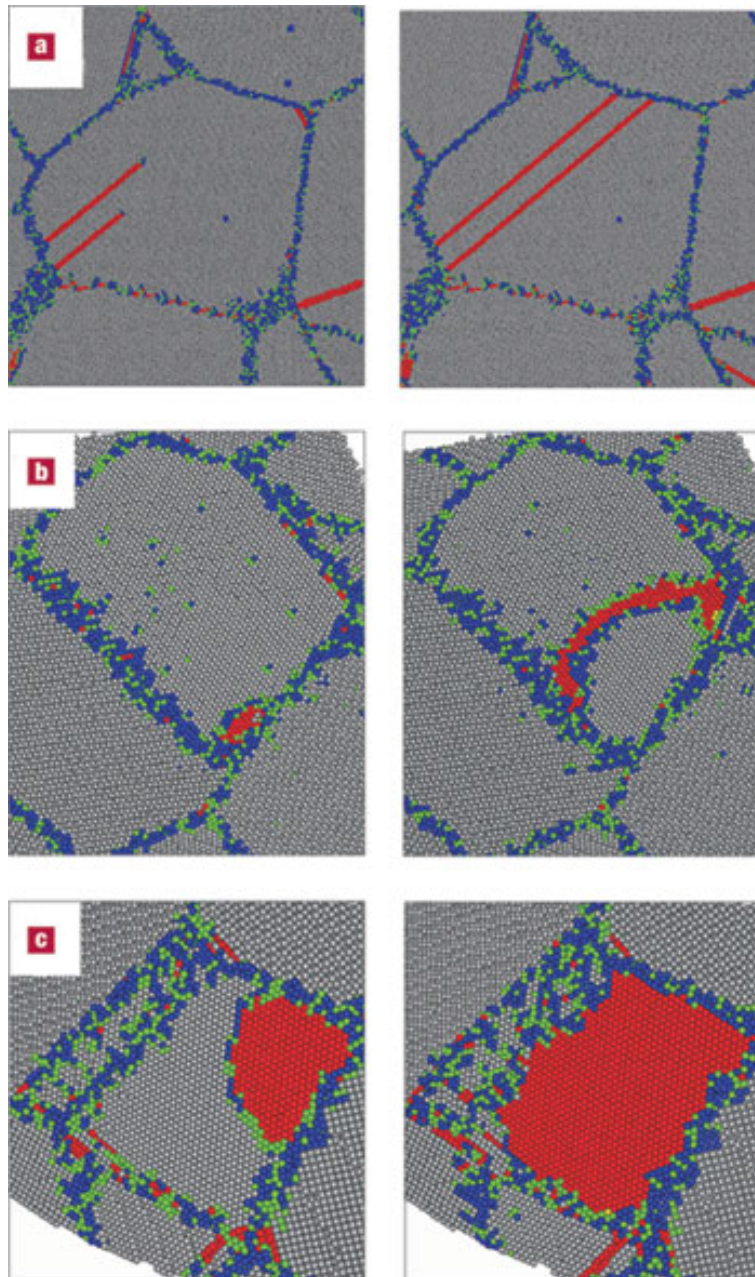


Fig. 2.5: Typical deformation mechanisms of nanocrystalline materials [Swygenhoven et al. 2004]. (a) Extended partials that transect the entire grain in nanocrystalline Ni (b) A full dislocation that nucleates locally at a grain boundary in nanocrystalline Al. (c) A partial dislocation that has nucleated at a triple junction in nanocrystalline Cu.

2.2.5 Grain-boundary based deformation mechanisms: crossover from 'normal' to 'inverse' Hall-Petch behaviour

The variation of flow stress as a function of grain size from the microcrystalline to the nanocrystalline regime are schematically shown in Fig. 3.3. Conventional polycrystalline metals and alloys show an increase in yield strength (σ_y) with decreasing grain size (d) according to the well-known Hall–Petch equation:

$$\sigma_y = \sigma_0 + k d^{-1/2} \quad (2.3)$$

where σ_0 is friction stress resisting the motion of gliding dislocation, and k is the Hall–Petch slope. In analogy, the hardness (H_v) can be related to the grain size by

$$H_v = H_0 + k_H d^{-1/2} \quad (2.4)$$

For better understanding of the plastic deformation mechanism, we have divided crystalline materials in four groups (see Fig. 2.6):

- (i) Microcrystalline regime (grain size above 1 μm)
- (ii) Ultrafine-grained regime (grain size in the 100 -1000 nm range)
- (iii) Upper nanometer grain-size regime (grain size between 10 -100 nm)
- (iv) Lower nanometer grain-size regime (grain size below 10 nm)

(i) A microcrystalline regime, ranging from the single crystal to a grain size of about 1 μm ; in this regime the classical Hall–Petch description applies; The Hall–Petch effect in conventional coarse-grained materials is attributed to the grain boundaries acting as efficient obstacles to dislocations nucleated mostly from Frank–Read sources.

(ii) For the ultrafine-grained materials, grain boundaries act as dislocation sources for the nucleation of complete dislocations that subsequently glide across the grains where they become re-incorporated into the grain boundary structure. Other than for the inability of Frank–Read sources to operate within such small grains, the material therefore still seems to deform by the conventional dislocation-slip mechanism. In this region the Hall-Petch slope remain same as microcrystalline materials.

(iii) Upper nanometer grain-size regime, grain size between 100 nm to 10 nm; in this regime the Hall–Petch slope is smaller than its value in coarse-grained materials, in some cases even near-zero. In this region extended dislocation are nucleated from grain boundaries when the grain size remains larger than the dislocation splitting distance. When the grain size becomes comparable to the dislocation splitting distance, only single partials can be nucleated, producing stacking faults in their glide through the grains.

(iv) Lower nanometer grain-size regime (grain size below 10 nm) below which the Hall–Petch slope is negative, hence with a decrease in strength on decreasing grain size. This behaviour is often referred to as the “inverse” Hall–Petch effect. Both simulation studies of the mechanical behaviour in the crossover regime [Yamakov et al 2003, Schiotz et al 2003] revealed that the transition from a dislocation-based to a GB-mediated deformation mechanisms with decreasing grain size leads to a crossover in the mechanical behaviour, from Hall–Petch hardening to softening. However, the exact nature of GB-mediated deformation mechanisms (when $d < d_c$) is still subjected to debate. Several mechanisms such as mesoscopic glide [Hahn et al. 1997], grain

boundary diffusion creep [Yamakov et al. 2002a] and grain rotation [Ovidko 2002] has been proposed to account for the plastic deformation without dislocation motion below the critical grain size. Grain boundary sliding over finite distances requires changes in the grain shape. Therefore, an accommodation process must be active in parallel. Recent, Weissmuller et al. (2005) suggested a new accommodation mechanism based on recent experimental investigations (Markmann et al. 2003, Rosner et al. 2004).

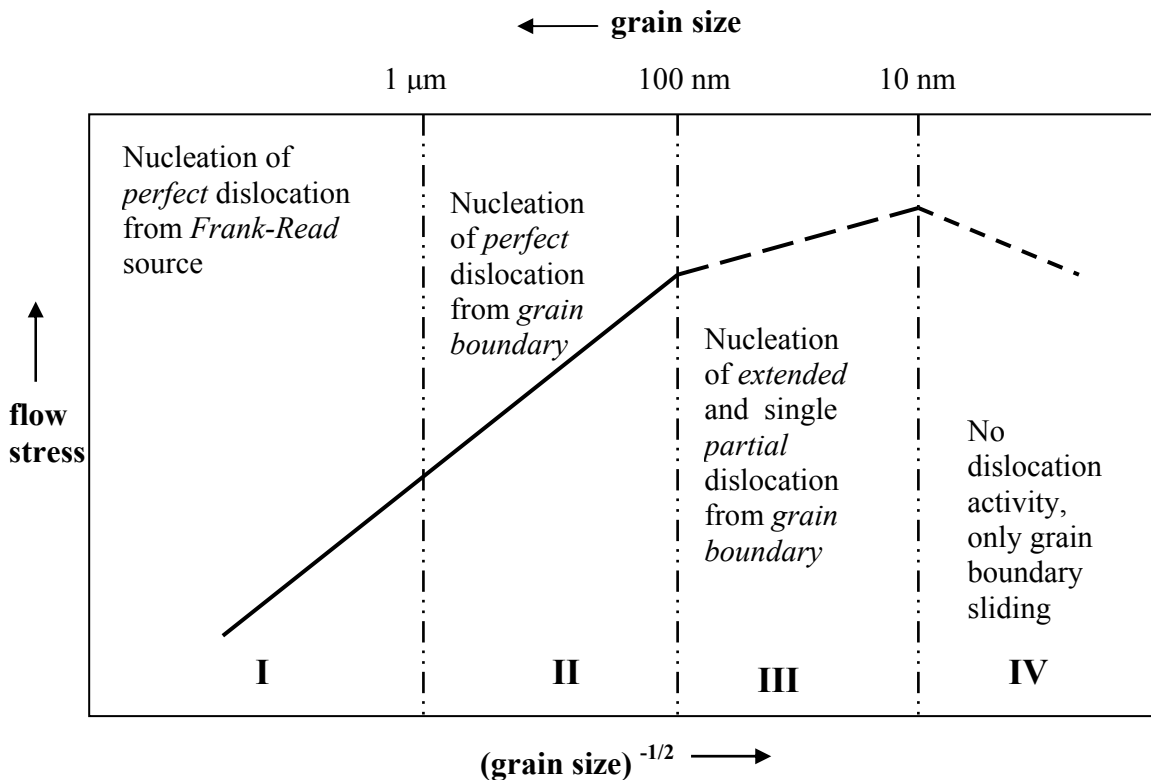


Figure 2.6: Schematic representation of the variation of yield stress as a function of grain size in microcrystalline, ultrafine-grained and nanocrystalline metals and alloys.

Ambient temperature mechanical softening with decreasing grain size in nanostructured materials - the so called “inverse Hall-Petch effect” is still under debate. However, we described that no dislocation activity exists below a critical grain size which is around the width of the stacking fault region between the partial dislocations. Therefore, deformation must take place by GB-mediated deformation mechanisms below a critical grain size. Moreover, the critical grain size must be determined by experimental study. However, up to now no reliable data are available on this context due to the problem of finding full density nanocrystalline materials of grain size less than 50 nm without any artefacts.

2.3 Mechanical alloying and solid-state amorphization

2.3.1 Introduction

Glasses have been manufactured from silica and related oxides for more than 4000 years. A glass is characterized by its lack of long-range atomic order and exhibits a glass transition manifested by a change in the thermodynamic properties, such as specific heat and thermal expansion coefficient during heating or cooling. In 1960, Klement *et al.* obtained the first amorphous alloy (or metallic glass) by liquid melt quenching in the Au-Si system. A glass is obtained when a liquid is cooled into a state of rigidity without crystallizing. Metallic glasses are now formed in suitable systems by processing techniques such as rapid solidification from the liquid state, vapour deposition, plasma processing, and laser processing [Suryanarayana 1999].

Because of their noncrystalline structure with no grain boundaries, amorphous alloys have an unusual combination of properties such as high strength, good bend ductility, high fracture toughness, good corrosion resistance, and desirable soft magnetic properties. Because of this, metallic glasses have found several industrial applications, the most important of which is for core laminations in distribution transformers [Liebermann 1993].

Because of the high quenching rate requirements ($10^4 - 10^6$ K/s), only thin ribbons or foils with a thickness less than 100 μm could initially be fabricated with rare exceptions such as the Pd- base Pd-Ni-P alloys [Kui et al.1984, Wilde et al. 1994]. Recently, a series of bulk metallic glasses of La- [Inoue et al. 1990a], Zr- [Peker et al. 1993], and Mg- [Inoue et al. 1993] based alloys have been found with critical cooling rates less than 100 K/s. However, the preparation of bulk metallic glasses by melt quenching is still limited by the appropriate composition and usually contain more than three elements in the vicinity of the deep eutectic point of the phase diagram. There are also methods of amorphizing a solid without passing through the liquid state at any stage. Known as solid-state amorphization reactions, these include irradiation, hydrogen-assisted amorphization, interdiffusion of elemental metals, pressure-induced vitrification, and mechanical alloying.

Since the first report of Schwartz et al. (1983), the solid-state amorphization reactions (SSAR) have been observed in many binary and multicomponent systems in both deposited multilayers [Schröder 1985, Meng et al. 1987] and by mechanical alloying processes [Hellstern et al. 1986, Schwarz et al. 1986]. The two main mechanical alloying processes that can induce a crystalline-to-amorphous transition are milling of powders [Schwarz et al. 1986] or repeated cold rolling [Atzmon et al. 1985, Wilde et al.1999]. A considerable amount of work has been performed on amorphization induced by mechanical alloying. However, the mechanisms of mechanically induced solid-state amorphization reactions are not yet firmly established especially concerning the early stages of the transformation. Compared to ball milling, repeated cold rolling has been much less systematically studied; however, this technique is especially useful to investigate the early stages of amorphization during mechanical alloying.

Based on the experimental data, the glass-forming ability of binary metal systems was defined to distinguish qualitatively between systems from which it is either

possible or not possible to obtain metallic glass by liquid melt quenching, and correspondingly the systems have been classified into two groups: glass-forming and non-glass-forming systems. Because of their powerful capability, solid-state amorphization reactions have so far produced a great number of non-equilibrium alloys with either an amorphous structure, not only in glass-forming systems but also in some non-glass-forming systems defined previously based on the experimental results from liquid melt quenching. For example, some new amorphous alloys have been obtained by a solid-state amorphization reaction in immiscible systems for example Y-Mo [Chen et al. 1996] and Ag-Cu [Sheng et al. 2002]. It follows naturally that some basic concepts and understanding concerning metallic glasses should be somewhat modified or further developed, e.g. the previously defined glass-forming and nonglass-forming systems, the glass-forming ability or glass-forming composition range of binary metal systems, etc. In addition, the exact mechanism of the early stages of interdiffusion or forced atomic mixing at the interface, specially in nanoscale heterophase materials is not well understood.

2.3.2 Mechanically activated solid-state amorphization

Schwarz et al. (1983) observed for the first time a phenomenon called solid-state amorphization reaction (SSAR) in Au-La multilayered films produced by medium temperature annealing and claimed that a large negative heat of formation (ΔH_f) and a large asymmetry of the component interdiffusivities of the elements were necessary for a SSAR to take place. The large negative ΔH_f makes an amorphous phase have a lower free energy than that of a mechanical mixture of two crystalline metals and thus serves as the thermodynamic driving force. Meanwhile, the large asymmetric diffusion, i.e. atoms of one metal diffuse much faster into the other constituent phase than vice versa, which in turn kinetically suppresses either nucleation or growth of the possible intermetallic compounds-frequently of complicated structure. Since then, SSAR has been observed in some other binary metal systems having characteristics similar to those of the Au-La system. A little later, Clemens suggested two similar parameters to predict the possibility of SSAR, i.e. a large negative ΔH_f and an atomic volume ratio considerably different from one [Clemens 1986]. The atomic volume ratio was thought to result in asymmetric interdiffusion of atoms.

Metallic glasses have been obtained by rapid solidification techniques in a number of binary and ternary alloy systems. It has been well established that, amongst other conditions, the likelihood of obtaining a glassy phase is very high near deep eutectics. But, in mechanically alloyed powders an amorphous phase is obtained around the equiatomic composition [Schwarz et al. 1993]. This observation can be rationalized with reference to Fig. 2.7. A hypothetical binary phase diagram featuring some solid solubility on either end and also exhibiting the presence of an intermetallic phase is shown in Fig. 2.7(a). α and β are the terminal solid solutions, γ is the intermetallic and L represents the liquid phase. The Gibbs free energies of the different phases at a temperature T_r (reaction temperature) are shown as a function of composition in Fig. 2.7(b), assuming that the free energy of the undercooled liquid fairly accurately represents the free energy of the amorphous phase. At this temperature, α , β , γ , and mixtures of these phases are thermodynamically stable, whereas L is metastable.

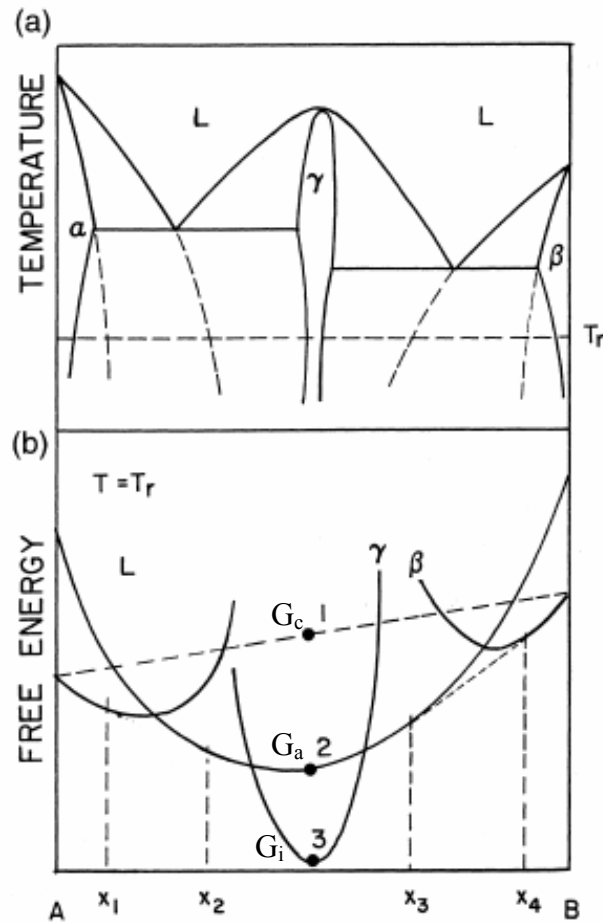


Figure 2.7: (a) Hypothetical binary phase diagram featuring some solid solubility on either end and also showing the presence of an intermetallic phase. (b) Gibbs free energy versus composition at a temperature corresponding to T_r in the above diagram.

The equiatomic blended elemental powder mixture has a free energy, G_c corresponding to point 1 in Fig. 2.7(b), half way along the straight line joining the free energies of pure metals A and B. If the two components are allowed to interdiffuse freely, then the lowest free energy state corresponding to the formation of the γ phase, G_i (point 3) will be obtained. Even though thermodynamically this is the lowest free energy state, this can be kinetically prevented from occurring when the free energy G_a , corresponding to the formation of an amorphous phase (point 2), is reached.

Preventing the reaction $c \rightarrow i$ (crystalline solid solution to intermetallic compound) from occurring and favouring $c \rightarrow a$ (crystalline solid solution to amorphous phase) to occur is possible by a proper choice of metals A and B, the reaction temperature T_r , and the reaction time t_r . Schwarz and Johnson (1983) proposed that two conditions need to be satisfied for an amorphous phase to form from a thin film couple (or a blended elemental powder mixture). First, the two metals must have a large negative heat of mixing in the liquid (amorphous) state, and this provides the thermodynamic driving force for the reaction to occur. Hellstern et al. (1987) confirmed the importance of the large negative heat of mixing by studying the glass-forming ability of several titanium-containing transition metal alloys. Systems such as Cu-Ti and Co-Ti with a large negative heat of mixing could be completely amorphized, while Fe-

Ti, Mn-Ti, and Cr-Ti could be only partially amorphized due to their smaller heat of mixing. The isomorphous V-Ti system did not amorphize at all because a solid solution always formed on milling the powder mixture.

The reaction time scales also are important because not only should one allow the formation of the amorphous phase, but also maintain it without transforming to the equilibrium phases. These concepts can be explained with reference to Fig. 2.8. Like in Fig. 2.7, if we assume that the free energy of the blended elemental mixture is G_c , that of the amorphous phase as G_a , and that of the intermetallic as G_i , then these are schematically shown in Fig. 2.8. To prevent the stable intermetallic from forming, the time scale for the formation of the amorphous phase from the blended elemental mixture, i.e., $t_{c \rightarrow a}$ should be much shorter than $t_{c \rightarrow i}$. Further, since the amorphous phase is metastable, $t_{a \rightarrow i}$ should be much longer than $t_{c \rightarrow a}$ so that the stability of the amorphous phase can be increased. Thus, the kinetic conditions for the formation of an amorphous phase by solid state reactions can be summarized as:

$$t_{c \rightarrow a} \ll t_{c \rightarrow i} \quad \text{and} \quad t_{a \rightarrow i} \gg t_{c \rightarrow a}$$

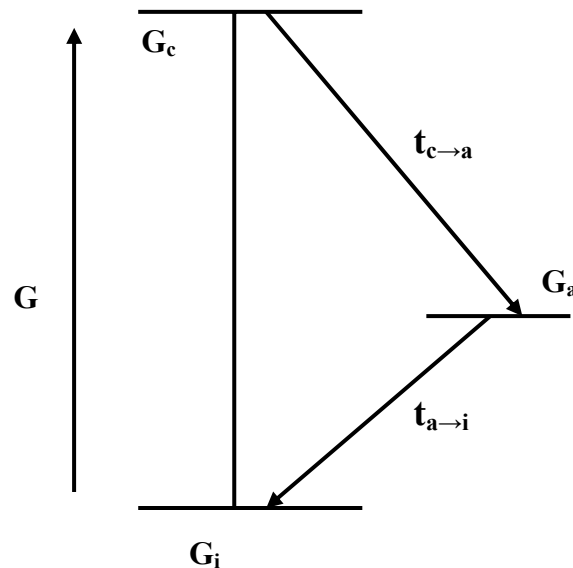


Figure 2.8: Schematic free energy diagram indicating the criteria to be met for solid state amorphization.

In the last decade, SSAR have also been observed in some binary metal systems having different characteristics from those of the Au-La system, e.g. in the Ni-Mo system with a small negative ΔH_f [Zhang et al. 1994], in the immiscible Cu-Ta equilibrium system even with a positive ΔH_f [Liu et al. 1996], and in the Au-Ta system in which the two metals have almost identical atomic size [Pan et al. 1995]. Table 2.1 lists the observations of SSAR in different binary metal systems. Evidently, the development of a general criterion capable of predicting the possibility of SSAR in binary metal systems with either positive or negative ΔH_f is needed. Moreover, the subject of kinetics is still an open question requiring much further investigation.

Table 2.1: Lists of binary metal-metal systems observed to exhibit solid-state amorphization reactions.

System	ΔH_f (kJ mol ⁻¹)	Atomic size difference (%)
Transition metal–rare-earth systems		
Au–La	–108	23.2
Cu–Er	—	27.3
Ni–Ce	–40	31.7
Ni–Er	–48	29.1
Simple-metal–transition-metal systems		
Al–Mn	–43	4.6
Al–Mo	–24	4.8
Al–Pt	–82	3.1
Mg–Ni	–8	22.1
Sn–Co	–17	10.8
Transition-metal–transition-metal systems		
Au–Ta	–49	0.8
Au–Y	–110	20.0
Au–Zr	–112	9.3
Co–Zr	–60	21.2
Cu–Nb	+4	10.6
Cu–Ta	+3	9.4
Cu–W	+33	6.8
Cu–Y	–32	29.1
Fe–Zr	–37	21.9
Hf–Ni	–63	20.3
Mo–Ni	–11	8.6
Mo–Y	+35	24.4
Nb–Ni	–45	12.8
Nb–Y	+44	20.7
Ni–Ta	–44	12.9
Ni–Ti	–52	14.0
Ni–Zr	–72	21.6
Ta–Y	+40	21.8
W–Y	+35	24.0

The diffusion coefficient of Cu and Ni in Zr at ambient temperature is in the order of 10^{-22} – 10^{-24} m²/s. This means that at room temperature no effective movement would be possible. However, SSAR has been observed in Cu–Zr and Ni–Zr systems by ball milling of elemental powder mixture. Therefore, there must be a considerable amount of atomic mixing occurring before the crystal to amorphous phase transformation occurs. However, the mechanisms for the atomic mixing process at room temperature is still in debate. Additionally, supersaturated solid solution or even amorphous phase formation was observed in systems with a positive heat of mixing, for example, Ag–Cu or Y–Mo. Moreover, the thermodynamics can not explain the atomic mixing of immiscible elements by mechanical alloying. In section 5.4, we propose a new mechanism which can explain atomic mixing process at room temperature even in immiscible metallic systems.

2.3.3 Enhanced solid-state amorphization by sharp concentration gradients

Solid state diffusion and diffusion controlled reactions are important phenomena in many areas of technology, especially in the case of multilayered structures used in microelectronics devices. Amorphization by solid-state reaction has been observed in many binary multilayer systems. It is well known that in thin film configurations, certain crystalline or amorphous phases may grow at the expense of other thermodynamically more stable phases. An unsolved problem concerning the thermodynamic and kinetic aspects of solid-state amorphization is why in its early stage amorphous alloys can form and grow without evidence of intermetallic-compound formation. The usual thermodynamic analysis has shown that in solid-state amorphization the driving force for amorphous-alloy formation is smaller, at least, than that for the formation of some intermetallic compounds and that has suggested that the answer for this problem must lie in the kinetic constraints which restrict the nucleation of intermetallic compounds. However, the usual thermodynamic analysis has not considered the effects of concentration gradients occurring during the early stage of solid-state amorphization. Desre' et al.(1990, 1991, 1996) suggested on the basis of thermodynamic arguments that sharp concentration gradients present during diffusion mixing facilitate amorphization in solid state reactions by reducing or suppressing the driving force for crystallization. As the concentration gradient diminishes during diffusive layer growth, the driving force for the crystallization of compounds is gradually restored and the energy barrier to their nucleation reduced to the classical value.

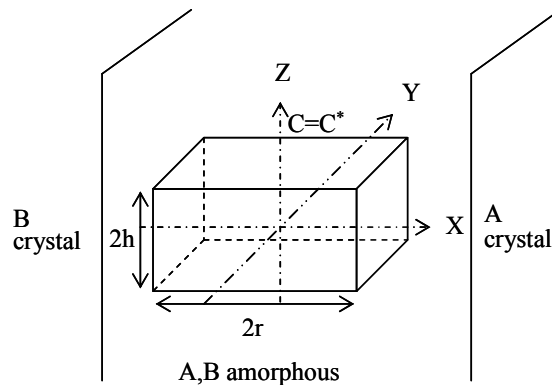


Figure 2.9: Parallelepiped- or cube ($h = r$) shaped intermetallic phase nucleus in amorphous layer. r is parallel to concentration gradient ∇C along x .

Using the classical homogeneous nucleation theory, the free-energy change upon formation of a cubic nucleus of dimension $2r$ of an AB compound (Fig. 2.9) from an amorphous phase of the same concentration would be

$$\Delta G_N = 24\sigma r^2 + 8\rho\Delta G_{pc}r^3 \quad (2.7)$$

where the first term is the nucleus surface area times the interfacial energy σ and the second term is the usual molar free energy of polymorphous crystallization times the nucleus volume $8r^3$ and the atom density ρ (mol/cm^3). Desre' et al. (1990) have recently shown that for a compound embryo of dimensions $2r$ and composition C^* , forming from an amorphous phase of concentration ranging from $C(-r)$ to $C(+r)$, the

expression for the Gibbs free energy of nucleation taking into account the effect of the concentration gradient ∇C in the amorphous phase is approximately given as [Desre' et al. 1990]

$$\Delta G_N = 24\sigma r^2 + 8\rho\Delta G_{pc}(C^*)r^3 + \frac{4}{3}\rho\alpha(\nabla C)^2 r^5 \quad (2.8)$$

where
$$\alpha = \frac{\partial^2 G_a}{\partial C^2} > 0,$$

σ is the interfacial energy of the intermediate phase, ρ is the number of moles of atoms per unit volume, ΔG_{pc} is the free energy change for polymorphous transformation at composition C^* . The first two terms in Eq. (2.8) represent the usual contribution of surface and volume effects to nucleus formation. The main consequence of the concentration gradient appears in the $(\nabla C)^2 r^5$ term of Eq. (2.8). Clearly, this term will be most important during the earliest period of interdiffusion. As the coefficient of the r^5 term is positive which suppresses the driving force for nucleation by compensating for the second term with $\nabla G_{pc} < 0$ for sufficiently sharp gradients ∇C . In fact, as shown in Fig. 2.10 which refers to nucleation of $Ni_{10}Zr_7$ in Ni-Zr amorphous layers at the largest ∇C values nucleation is prohibited until a critical gradient ∇C_c given by

$$\nabla C = \frac{\rho}{9\sigma} \frac{(2\Delta G_{pc})^{3/2}}{\alpha^{1/2}} \quad (2.9)$$

is reached, but even at ∇C_c the nucleation barrier is larger than that for a uniform solid solution.

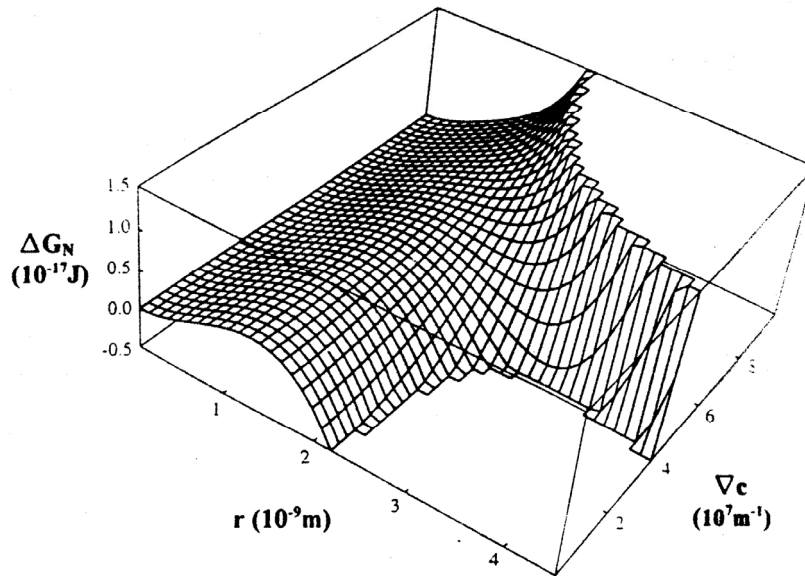


Figure 2.10: Work of nucleus formation ΔG_N as a function of nucleus size r and imposed concentration gradient ∇C .

Let us use equation 2.8 to calculate the effective driving force for nucleation of the $\text{Ni}_{10}\text{Zr}_7$ intermetallic compound phase from an amorphous $\text{Ni}_{64}\text{Zr}_{36}$ layer under a concentration gradient ∇C . For a critical gradient $\nabla C_c = 4.85 \times 10^5 \text{ cm}^{-1}$, no negative value of ΔG_N is obtained and the minimum is attained at $\Delta G_N = 0$. This implies that for $\nabla C > \nabla C_c$, no driving force is available for nucleation of $\text{Ni}_{10}\text{Zr}_7$. Furthermore, the minimum in $\Delta G_N(r)$ vs r no longer occurs in the ∇C range greater than $5 \times 10^5/\text{cm}$. Since the total concentration variation across the amorphous layer is of the order of $\nabla C = 0.6 - 0.8$ (for Ni-Zr, Cu-Zr), the critical concentration gradient correspond to a critical thickness $\epsilon_c \cong 0.8/\nabla C_c$ of the amorphous phase formed by a solid state reaction across which crystallization is thermodynamically disallowed. For $\nabla C_c \cong 5 \times 10^5/\text{cm}$, a critical thickness $\epsilon_c \cong 160 \text{ \AA}$ is obtained.

With a similar approach Zheng (1992) demonstrated an analysis of the effect of a sharp concentration gradient on the nucleation of intermetallic compounds within a metastable solid solution formed by interdiffusion of pure elements. It has been predicted that at small concentration gradients, the driving force for intermetallic-compound formation will be larger than that for amorphous-alloy formation; on the other hand, at sufficiently sharp concentration gradients, the driving force for amorphous-alloy formation will be larger than that for intermetallic compound formation.

According to the above discussion, solid-state amorphization, in which very sharp concentration gradients occur at the beginning and then gradually flatten out, can be divided into two stages.

- (1) In the first stage, the concentration gradients are very sharp so that driving forces are available for only amorphous-alloy formation, which is larger than that for intermetallic compound formation. As a result, amorphous-alloy formation will be observed and intermetallic-compound formation will not be observed during this stage.
- (2) In the second stage, the concentration gradients are small so that driving forces are available for both amorphous-alloy and intermetallic-compound formation, and the driving force for intermetallic-compound formation is larger than that for amorphous-alloy formation. As a result, intermetallic-compound formation will be observed and continuing amorphous-alloy formation will not be observed during this stage.

Chapter 3

Experimental Procedure

3.1 Repeated Cold-Rolling (Folding and Rolling)

There is continued interest in finding cost effective and simpler ways to fabricate nanostructured materials, even though research groups have been investigating possibilities for the past three decades. The grain sizes achieved through all severe plastic deformation (SPD) routes for pure metals are actually outside the nanocrystalline regime [see section 2.1]. Thus, an alternate SPD technique needs to be developed which can produce massive bulk nanostructured materials. Moreover, recently Zehetbauer et al. (2003) reported that the high applied pressure reduces the diffusion coefficient for vacancy diffusion, restricting thereby the annihilation of dislocations, thus leading to a higher density of equilibrium vacancies and dislocations which is the main key to reduce the steady-state grain size and thus the finally achievable grain size via severe plastic deformation. However, in principle it should be feasible to obtain a truly nanoscaled grain structure by applying large strains only, if processing is conducted at a low homologous temperature such that rapid dislocation annihilation is prevented. In order to verify this assumption, an extremely large strain was applied to different fcc (Ni and Pd) and hcp (Ti and Zr) metals by repeated rolling and folding at ambient temperature. This synthesis option presents a low-pressure, low strain-rate processing route that allows – in principle – the application of unlimited strain since the true strain depends only on the number of rolling and subsequent folding repetitions.

The repeated cold rolling and folding (F&R) process is schematically illustrated in Fig. 3.1. Pure elemental foils with initial thickness of 12-50 μm were stacked and then folded 4 to 5 times to yield a 20x20 mm^2 multilayer sandwich. The sample weight was about 2 to 3 g. The folded samples were rolled in a motorized 2-high rolling mill at a strain rate of 0.5 s^{-1} to a thickness of approximately 200 μm to obtain the starting material. Thereafter, the sample was folded and then rolled for 10 subsequent times with a continuously decreasing spacing between the rolls until the thickness was decreased to

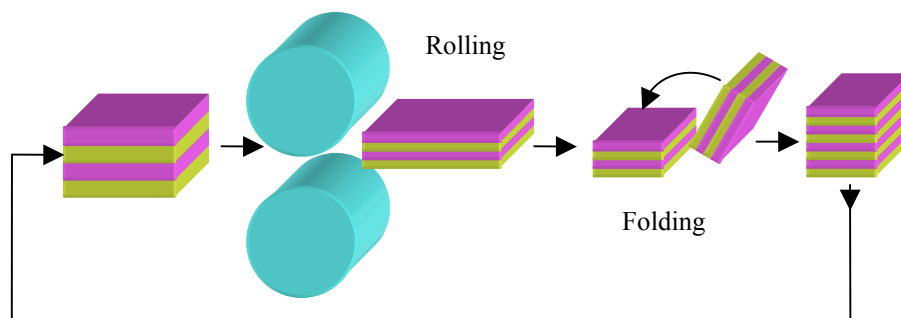


Figure 3.1: A schematic illustration of the cold-rolling and folding process (F&R). The thickness of the multilayer of elemental foils is reduced by 50% with each rolling and folding pass.

200 μm . This procedure constitutes one folding and rolling (F&R) pass. Thereafter, the sample was cut (or broken) in half, stacked and cold-rolled again, following the same procedure. The deformation procedure (1 F&R-pass) was repeated for up to 100 times. The deformation time and the respective strain rate were calculated from the geometry of the rolls (diameter of the rolls 150 mm, length of the rolls 100 mm), the circumferential roll velocity (1m/min) and the thickness of the samples (200-400 μm). In fact, the actual strain rate is smaller than the calculated upper bound, because of the sliding at the internal interfaces and due to certain areas of the sample that do not overlap after the folding. Consequently, a small area fraction is not deformed during rolling, as described by [Bordeaux et al. 1990]. Moreover, the bending of the rolls that occurs inevitably is not included in the simplified calculation. The theoretical true strain corresponding to 100 F&R cycles amounts to ~ 80 (see appendix A.3), as obtained from the calculated average layer thickness reduction. However, the actual true strain is smaller than this limiting theoretical value, as described above. By applying the F&R technique we successfully produced nanocrystalline metals and alloys in large quantity (See chapter 4). A similar procedure has previously been used to synthesize multilayer samples [Atzmon 1984], UFG materials [Saito et al. 1998] or metallic glasses [Wilde et al. 1999]. In the case of UFG-materials, the rolling and folding procedure with an additional intermediate “brushing” operation has been denoted as “Accumulative Roll-Bonding (ARB)” [Saito et al. 1998]. In fact, cold-rolling is a well-known process that is frequently applied in industrial processing of sheet metal. Yet, the deformation process used here differs from classical cold-rolling as well as from ARB in the amount of strain (that is far larger than in both processes), in the absence of lubricating agents and in the absence of intermediate brushing. Thus, due to friction at the roll surfaces, a shear strain component adds to the rolling strain that is active in conventional cold-rolling processing [Huang et al. 2003].

3.2 Materials Selection

Table 3.1 shows the different pure metals which have been cold-rolled at room temperature to systematically study the grain refinement process at different stages of deformation including the limiting minimum grain size achievable by repeated cold-rolling. For better understanding the strain induced grain refinement process, we selected two fcc (Ni and Pd) and two hcp (Ti and Zr) pure metals that have similar mechanical behaviour and thermal stability.

Table 3.1: Different pure metals (purity $\geq 99.95\%$) used in repeated cold-rolling.

Elements	Atomic radius (Å)	Melting point (K)	Mechanical Properties*					
			$\sigma_{0.2}$ (Mpa)	E (Gpa)	G (Gpa)	UTS (Mpa)	δ %	HB, MPa
Ni (fcc)	1.24	1726	80	200	75	400	40	800
Pd (fcc)	1.37	1825	60	120	50	195	40	480
Ti (hcp)	1.46	1946	100	110	40	250	70	600
Zr (hcp)	1.60	2120	100	90	33	250	25	570

* $\sigma_{0.2}$ – yield stress, E – modulus of elasticity, G – shear modulus, UTS – ultimate tensile strength, δ , % – elongation to failure, HB – Brinell hardness [Grigoriev et al. 1997]

Table 3.2. lists the different systems that have been rolled starting from pure elemental multilayer sandwiches to study the progress of a solid state amorphization reaction in different glass forming systems for a better understanding of the early stages of the crystal-to-amorphous transition during intense mechanical deformation. All the cold-rolled samples were investigated by X-ray diffraction (XRD), followed by the characterization of their morphology in cross section by scanning electron microscopy (SEM) and plan view and cross-sectional transmission electron microscopy (TEM) and heat flow by differential scanning calorimetry (DSC).

Table 3.2: Different metal-metal composites that have been rolled starting from pure elemental multilayer sandwich to study the progress of solid state amorphization reaction.

Binary	Ternary	Quaternary
Ni ₅₀ Ti ₅₀ , Cu ₇₅ Ti ₂₅	Ti ₃₅ Zr ₁₀ Cu ₅₅	Ti ₃₅ Zr ₁₀ Cu ₄₇ Ni ₈
Cu ₄₀ Zr ₆₀ , Cu ₆₀ Zr ₄₀		Zr ₆₅ Al _{7.5} Cu _{17.5} Ni ₁₀
Ni ₃₆ Zr ₆₄		

3.3 X-ray Diffraction (XRD)

X-rays scattered from different layers of atoms can interfere with each other. If the Bragg condition is satisfied, constructive interference will occur and a peak in the diffraction intensity versus θ will appear. The microstructure evolution at different stages of the deformation process was followed by XRD that averages over the sample volume. The X-ray diffraction (Phillips X-Pert) intensity was measured in the Bragg Brentano geometry with Cu-K α ($\lambda = 1.5418 \text{ \AA}$) radiation at an operating voltage of 50 kV and a current of 40 mA with the continuously variable slit to maintain a constant irradiated area as θ becomes larger.

3.4 Scanning Electron Microscopy (SEM)

Scanning electron microscopy was used to estimate the average layer thickness and for compositional analysis using energy-dispersive x-ray analysis (EDX) of the cold-rolled samples at different deformation level. This was carried out in a Leo 1530 microscope at a typical accelerating voltage of 10 kV for taking micrographs and 20 kV for EDX analysis. The cross-sectional fracture surface was used for that purpose, since most of the individual layers broke at different positions, which results in a higher resolution of the individual layers in the SEM images as compared to polished cross-sections. The fracture surfaces were obtained by breaking the cold-rolled sheet perpendicular to their large surface.

3.5 Transmission Electron Microscopy (TEM)

For plan view transmission electron microscopy/selected area electron diffraction investigations (TEM/SAED, Philips Tecnai F20 ST operating at 200 KV), 3 mm in diameter samples were mechanically punched out. Thereafter, the Ni was thinned by twin-jet electropolishing (1/3 nitric acid and 2/3 methanol). Due to the detrimental impact of the electrolyte, Pd, Ti, Zr and all multilayer samples were thinned by ion milling with a low accelerating voltage (3.5 kV) to minimize the beam effects on the microstructure.

For cross-sectional TEM, 2 mm × 5 mm × 300 μm sample are glued into a 300 μm slit of the 2 mm diameter solid Cu cylinder. Then that Cu cylinder was inserted into a second hollow Cu cylinder (inner dia. 2mm and outer dia. 3mm) to give the necessary mechanical stability to the whole assembly. Thereafter, ~0.2 mm thick slices cut from 3 mm diameter sandwich and ground to a thickness of 60-80 μm using 800, 1200 and 2400 grit SiC papers and were further polished using a 3 μm diamond paste. Finally the sample was thinned by ion milling for electron transparency.

3.6 Differential Scanning Calorimetry (DSC)

Thermal analysis was carried out using a Perkin-Elmer Pyris 1, working between -170°C to 730°C. DSC is a technique which profiles heat loss or gain from a substance heated at a constant rate. Temperature and enthalpy calibrations were carried out by a standard procedure using pure indium and zinc as reference materials. The machine was calibrated for a heating rate of 20 °C /min, since most of the measurements were performed at this heating rate. Aluminium pans were used in the present study since they did not react with the studied samples at temperatures below 550 °C. For both isothermal and continuous heating runs, a sample size of 10-15 mg was used.

3.7 Setting up of a Rapid Thermal Annealing Furnace (RTA)

The furnace (Fig. 3.2) was designed and built for rapid thermal annealing treatment, for example, to change the concentration gradient at the interface of the multilayer samples. The heating source of the furnace is a special quartz lamp (short-wave twin-tube infrared emitter, 450 watts, 115 volts) that is controlled by a very fast controller (Eurotherm 2408) to reach the desired temperature within few seconds. The sample can be cooled very rapidly by purging Helium gas directly on the sample. The maximum heating and cooling rates of the furnace is around 50 °C s⁻¹. Additionally a special sample holder was built to hold the sample in the high flow rate of the cooling gas.

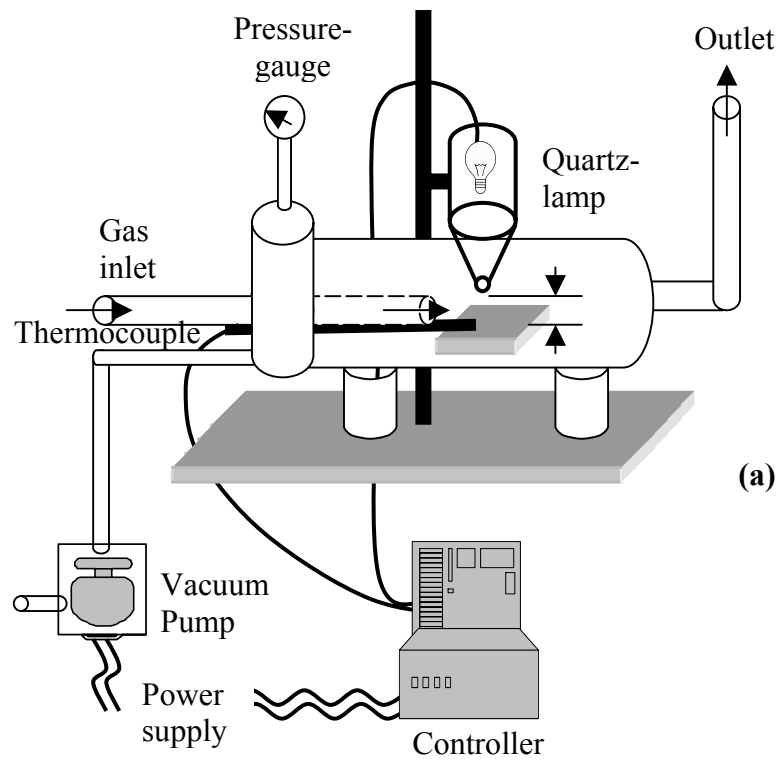


Figure 3.2: (a) Schematic figure and (b) Image of the rapid thermal annealing furnace designed for rapid heating and rapid cooling, (c) Sample holder.

Chapter 4

Nanostructured materials from repeated cold-rolling

In chapter 2 we briefly discussed that “severe plastic deformation” methods such as torsion straining under high hydrostatic pressure (HPT) in the range of several GPa, or equal channel angular pressing (ECAP) techniques have successfully been used to produce large quantity ultrafine-grained (grain size between 100 nm to 1000 nm) metals. Recently, Valiev et al. (2003) as well as Zehetbauer et al. (2003) reported independently that the high applied pressure reduces the diffusion coefficient for vacancy diffusion, restricting thereby the annihilation of dislocations, thus leading to a higher density of equilibrium vacancies and dislocations which is the main key to reduce the steady-state grain size and thus the finally achievable grain size via severe plastic deformation. However, we report that grain refinement up to the nanometer scale should be possible by applying large strains only, if processing is conducted at a low homologous temperature such that rapid dislocation annihilation is prevented. In order to verify this assumption, an extremely large strain was applied to different fcc (Ni and Pd) and hcp (Ti and Zr) metals by repeated rolling and folding at ambient temperature. In this chapter, we report the details of grain refinement process at different stages of plastic deformation and the thermal stability and mechanical response of one of the severely cold-rolled metals (Ni).

4.1 Synthesis of nanocrystalline metals

4.1.1 Elemental Ni (fcc)

The evolution of defect-structure and texture at different stages of the deformation can be followed by X-ray diffraction methods that average over the sample volume. Fig. 4.1a shows the XRD scan of an as-rolled multilayer sample (Ni) after different F&R cycles. Initially the intensity of the Bragg peaks of the elements gradually decreased and the peaks broadened with an increasing number of rolling passes (increasing strain) due to the refinement of the crystallite size and the build-up of internal lattice strain introduced into the samples during plastic deformation. After 40 F&R passes (true strain, $\epsilon \approx -32$, see appendix A.3 for strain calculation), the relative intensities of the (111) Bragg peak strongly increased and the (220) and (311) peaks almost vanished, indicating the formation of a strong rolling texture during cold-rolling. A metal which has undergone a severe amount of deformation, as in rolling or drawing, will develop a preferred orientation, or texture, in which certain crystallographic planes tend to orient themselves in a preferred manner with respect to the direction of maximum strain. The evolution of the texture during continued rolling deformation is indicated in Fig. 4.1b. The ratio of the (111)/(220) Bragg reflection intensity increased strongly up to 40 F&R passes. Further rolling up to 100 F&R passes ($\epsilon \approx -80$) gradually

reduced the intensity ratio down to a value close to 1. This reveals that a strong rolling texture developed in the early stages of rolling, which is indicative of a dominance of dislocation processes during that stage of the deformation process [Hughes et al. 2000]. The XRD scan after 100 F&R passes shows that all Bragg peaks have similar intensities, which represents that further deformation gradually reduces the texture developed during initial stages of rolling. The reduction of the rolling texture after 60 F&R passes indicates the presence of alternative deformation mechanisms that can become active at small nanocrystalline grain size, such as grain boundary sliding or grain rotation [Hahn et al. 1997] during further rolling beyond 60 F&R passes.

The common low-temperature plastic-deformation mechanism in coarse-grained materials involves the dislocations glide through the crystal on well-defined slip systems. However, recent molecular dynamics simulations [Shiotz et al. 1998, Swygenhoven et al. 2002] suggest that no dislocation activity exists below a critical grain size of 10 nm . Plastic deformation takes place entirely by means of grain boundary sliding and grain rotation. From TEM investigation, we observed that after 80 F&R passes the average grain size is 7-8 nm (Fig. 4.5). Therefore, it is anticipated that the local deformation mechanism changes from dislocation plasticity (rolling up to 60 F&R passes) to grain boundary sliding and grain rotation (after 80 F&R passes), which leads to a gradual decrease of the texture with continued cold rolling. However, texture analysis by pole figure (distribution of planes in stereographic projection) plots indicates that the sample after severe deformation (100 F&R) is not completely texture free. Fig. 4.2a show the pole figures of Ni after 100 F&R, indicating that the residual texture is at least qualitatively similar to those of other cold-rolled fcc materials.

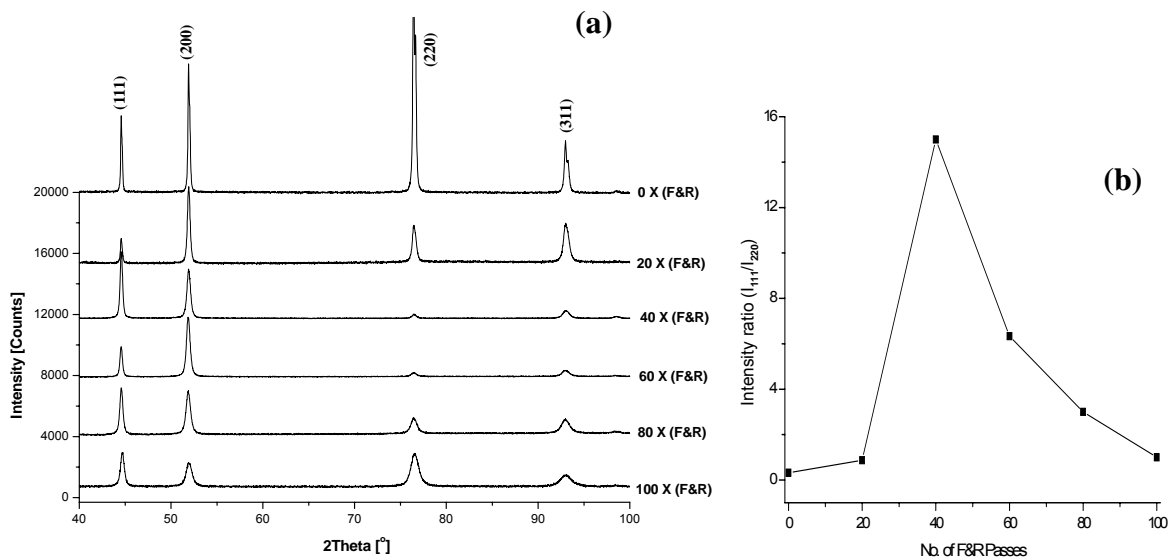


Figure 4.1: (a) XRD scan of as-rolled multilayer samples (Ni) after different F&R cycles as indicated in the figure. (b) Ratio of the intensities I of the (111) and the (220) Bragg reflection versus the number of F&R passes.

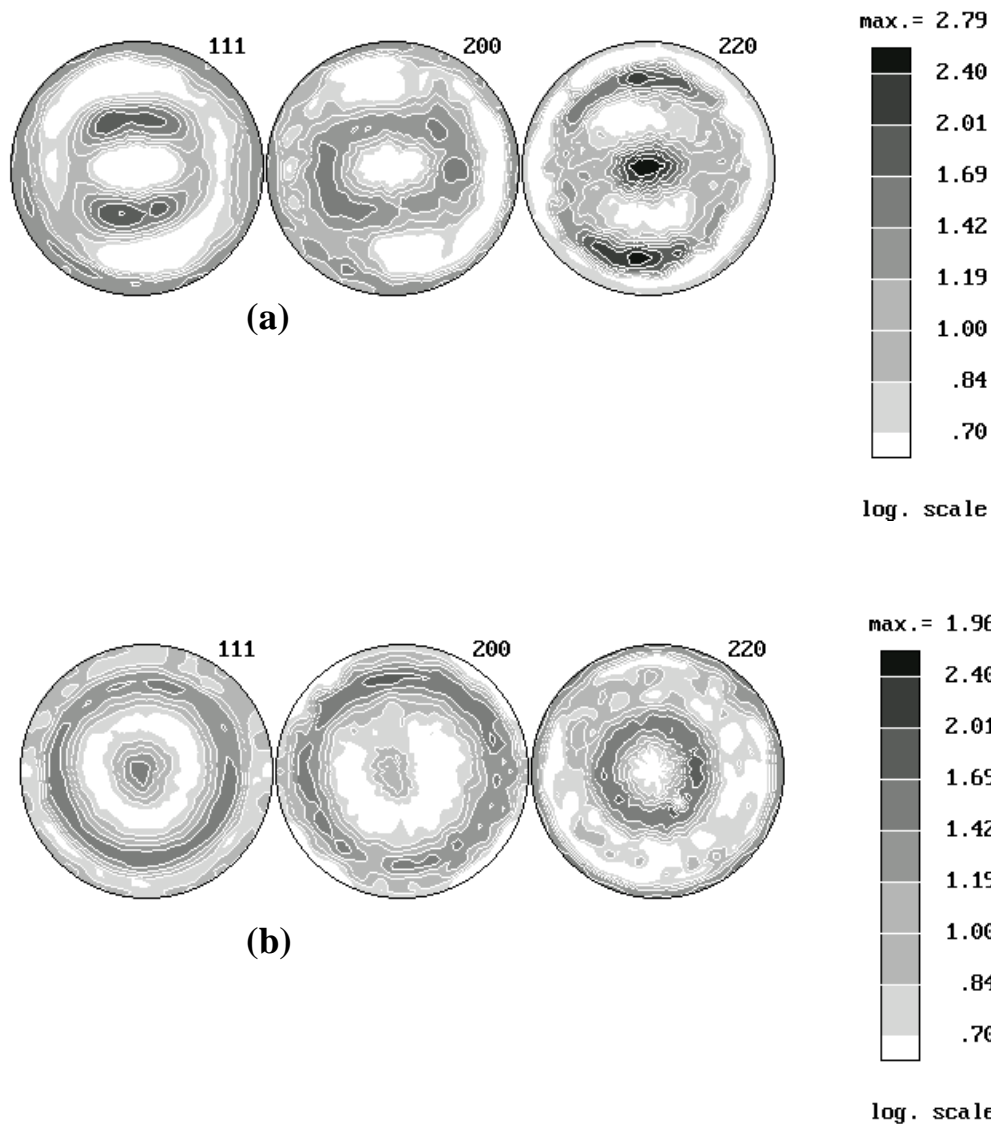


Figure 4.2: Pole figures in (111), (200), and (220) directions for (a) Ni after 100 F&R and (b) 100 F&R Ni after additional HPT (diameter of the die, $d = 10$ mm, pressure, $p = 6$ GPa, 5 rotations).

The severe cold rolled Ni (100 F&R) is further deformed by an additional High Pressure Torsion (HPT) (diameter of the die, $d = 10$ mm, pressure, $p = 6$ GPa, 5 rotations) to study the effect of additional HPT on the final microstructure. The HPT were performed in collaboration with Prof. R. Z. Valiev, Institute of Physics of Advanced Materials, Ufa State Aviation Technical University, Russia. Figure 4.2b shows the pole figures of 100 F&R Ni after additional HPT. It was noticed that the remaining rolling texture after extended folding and rolling has almost vanished after HPT. However, the change of texture after HPT does not prove grain boundary sliding or grain rotation during the HPT operation, because the orientation of grains changes due to a macroscopic partial rotation of the sample. This can be explained by figure 4.3.

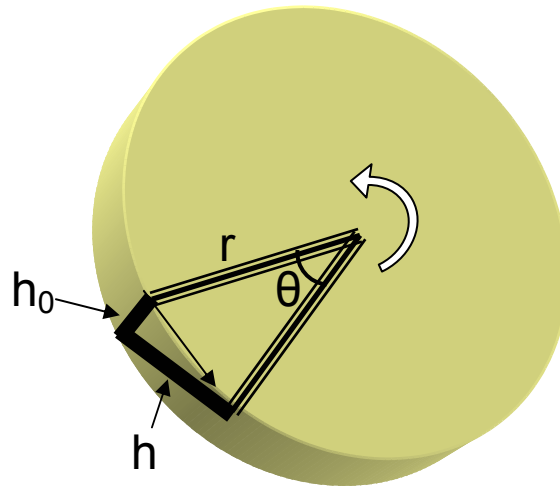


Figure 4.3: Schematic illustration of HPT processing.

Due to the small torsion, θ° (Fig. 4.3), straining the initial vertical slit (h_0) of the sample becomes inclined (h) and elongated. After a full (360°) rotation the vertical slit becomes almost horizontal. Therefore, there are two probabilities for the reduction of texture during HPT. Firstly, due to the grain boundary mediated deformation (grain boundary sliding and grain rotation) when plastic deformation takes place below a critical grain size. Secondly, due to the physical changes of the relative position and orientation of the sample geometry. However, it should be noted that the additional deformation under high pressure does not refine the microstructure any more. In fact, limited grain growth was observed after additional HPT most probably due to dynamic recrystallization during the HPT operation.

The continuous increase of strain during repeated cold rolling and folding of the multilayer sample resulted also in a decrease of the average layer thickness, l , with continuously increasing total interface area. The average thickness of the layers after n passes is given as: $l = l_0/2^n$ if the reduction is 50% per pass and if plane-strain conditions are assumed. In previous investigations, a multiple-necking of the elemental sheets has been reported to carry a significant part of the plastic deformation [Bordeaux et al. 1990]. However, rather large differences of the shear modulus values of the constituents are required for necking to occur, which is not the case for the presently studied single-element systems. Consequently, a rather homogeneous decrease of the layer thickness was observed in this work. SEM-investigations indicate that the bonding at the interfaces is not extensive during the initial stages of the deformation process (Fig. 4.4). Since EDX-measurements in cross-section revealed that the material, including the layer interfaces, are free from measurable quantities of contaminants, this behavior is most likely related to the low diffusivities at room temperature of Ni with melting points above 1700 K and deformed at low strain rates (compared to ARB) of the order of 1 s^{-1} . In addition, the average layer thickness is estimated from the SEM results. The cross-sectional fracture surface was used for that purpose, since most of the individual layers broke at different positions, which results in a higher resolution of the individual layers in the SEM images as compared to polished cross-sections. Fig. 4.4 shows the cross-sectional SEM micrographs of the fracture surfaces of cold rolled Ni at different deformation levels. It is apparent that cold rolling leads to a significant refinement of the layer thickness. The average layer thickness is about $1 \mu\text{m}$ after 20 F&R cycles. The

lamellar structure was highly refined with further rolling. Additional processing for up to 100 F&R cycles results in a refinement of the individual layers down to an average thickness of less than 50 nm. The von Mises equivalent strain,

$$\varepsilon = \frac{2}{\sqrt{3}} \ln\left(\frac{l}{l_0}\right),$$

corresponding to 100 F&R cycles amounts to ~ 80 , as obtained from the average layer thickness reduction.

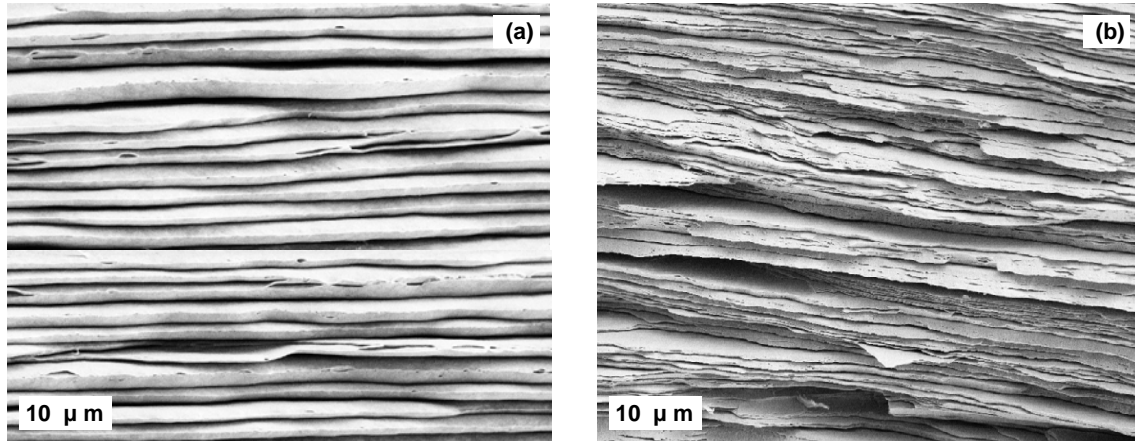


Figure 4.4: SEM images showing overviews of the deformed Ni-multilayer samples after different F&R cycles: (a) 10 cycles, (b) 20 cycles.

A quantitative and direct analysis of the grain size evolution during all stages of the deformation processing is impaired by the high defect densities and by the micro strain fields that affect X-ray diffraction (XRD) experiments as well as transmission electron microscopy (TEM). However, the combined results by XRD, scanning electron microscopy (SEM) on fracture surfaces and TEM at selected deformation stages indicate that the very early stages of the F&R deformation process are dominated by the thickness reduction of the individual layers together with the formation of a pronounced rolling texture. This behavior favors the formation of a “pancake”- like microstructure with similarly oriented grains that are elongated in both directions in the plane of the layer. In fact, the observation of grains with a diameter exceeding 200 nm in plane-view TEM investigations of pure Ni after 60 F&R-passes indicates that the in-plane diameter of the grain is considerably larger than the layer thickness that is of the order of a few tens nanometres at this deformation stage. With continued deformation, the defect accumulation within the elongated grain structure favours grain subdivision to reduce the strain energy, which becomes extensive after intense deformation due to multiple dislocation generation and rearrangement to form a cell - or subgrain structure. At decreasing grain size that is necessarily coupled to a development of the average grain shape towards equiaxed grains, the deformation mechanisms that govern plastic deformation at low strain rates and nanoscale grain sizes become active, thereby decreasing the texturing as explained above. Additionally, the grain size distribution becomes narrower when the average grain size decreases down to the range of a few tens of nanometres.

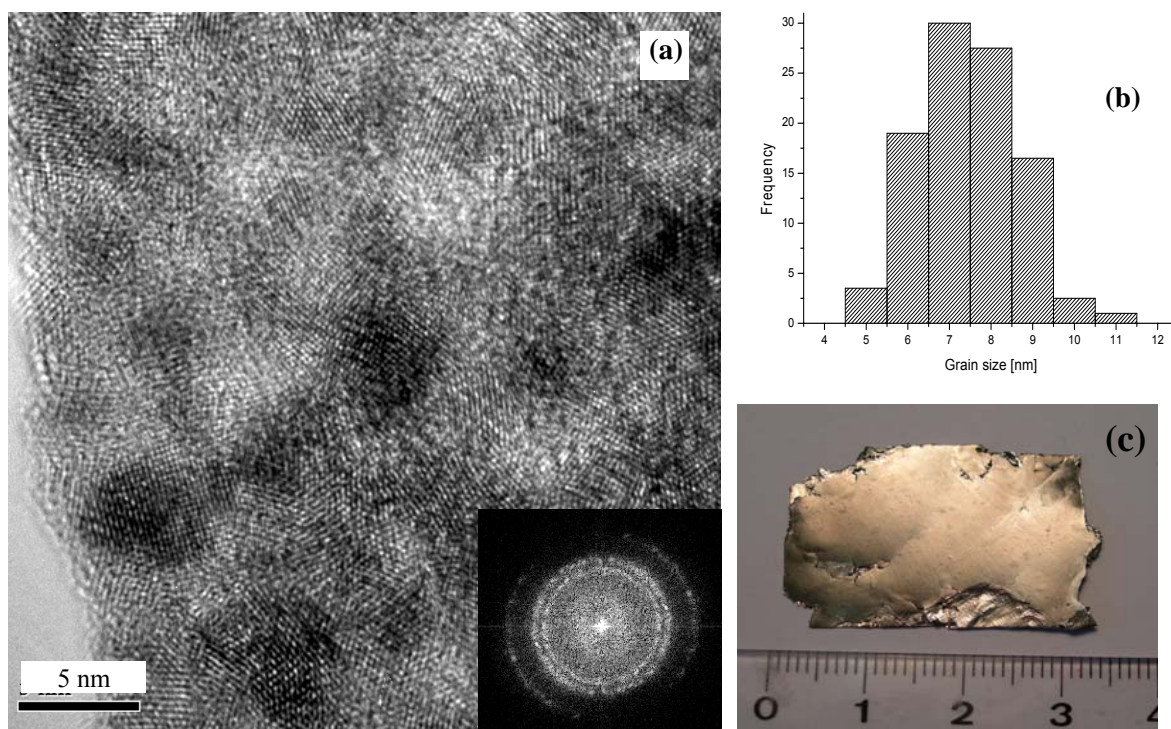


Figure 4.5: (a) HR-TEM micrograph of Ni that has been rolled for 80 passes. The inset at the bottom right corner shows the fourier transform pattern, (b) grain size distribution of Ni after 80 F&R passes, (c) bulk Ni sample after 80 F&R passes.

Fig. 4.5 shows a typical high resolution TEM image of pure Ni that has been folded and rolled for 80 passes. Clear lattice fringes are observed, indicating a dense nanocrystalline structure with an average diameter of the Ni-grains of about 7–8 nm. Quantitative analyses of the TEM high-resolution and dark-field images of about 100 grains, measuring always the largest diameter and the diameter in the direction perpendicular to the long axis, showed that the grain size distribution is fairly narrow (Fig. 4.5b). The fourier transform pattern of the image (inset in Fig. 4.5) shows a ring-like intensity distribution that indicates the presence of nanocrystals. To further analyze the microstructure of Ni after 80 F&R cycles, annealing experiments with subsequent microstructure analyses have been conducted. In this case, a Ni sample was heated to 350°C at a rate of 20°C/min under a purified Argon atmosphere and cooled at about 150°C/min directly after reaching 350°C. The HR-TEM micrograph shown in Fig. 4.6a indicates that the microstructure shows very limited coarsening due to the annealing treatment. In fact, the average grain size increased only marginally, from 7–8 nm previous of the annealing to about 10–12 nm after the thermal treatment (Fig. 4.6c). Yet, the thermal treatment was sufficient to allow for at least partial relaxation of the microstructure such that grain boundaries become distinguishable in the HR-TEM micrograph. The corresponding dark-field image (Fig. 4.6b) indicates clearly that the microstructure consists of a dense array of nanocrystalline grains of about 10–12 nm in diameter. Thus, a truly bulk (area of the sample is 5–6 cm² and thickness of the sample is around 0.5 mm, Fig. 4.5c) nanocrystalline structure has been obtained by repeated folding and cold-rolling of initially polycrystalline elemental sheets. EDX-

measurements by TEM revealed that the materials are free from metallic contamination. However, hot extraction measurement indicated that 0.24 wt. % Oxygen and 0.07 wt. % Nitrogen are present in the sample that has been rolled for 80 F&R passes.

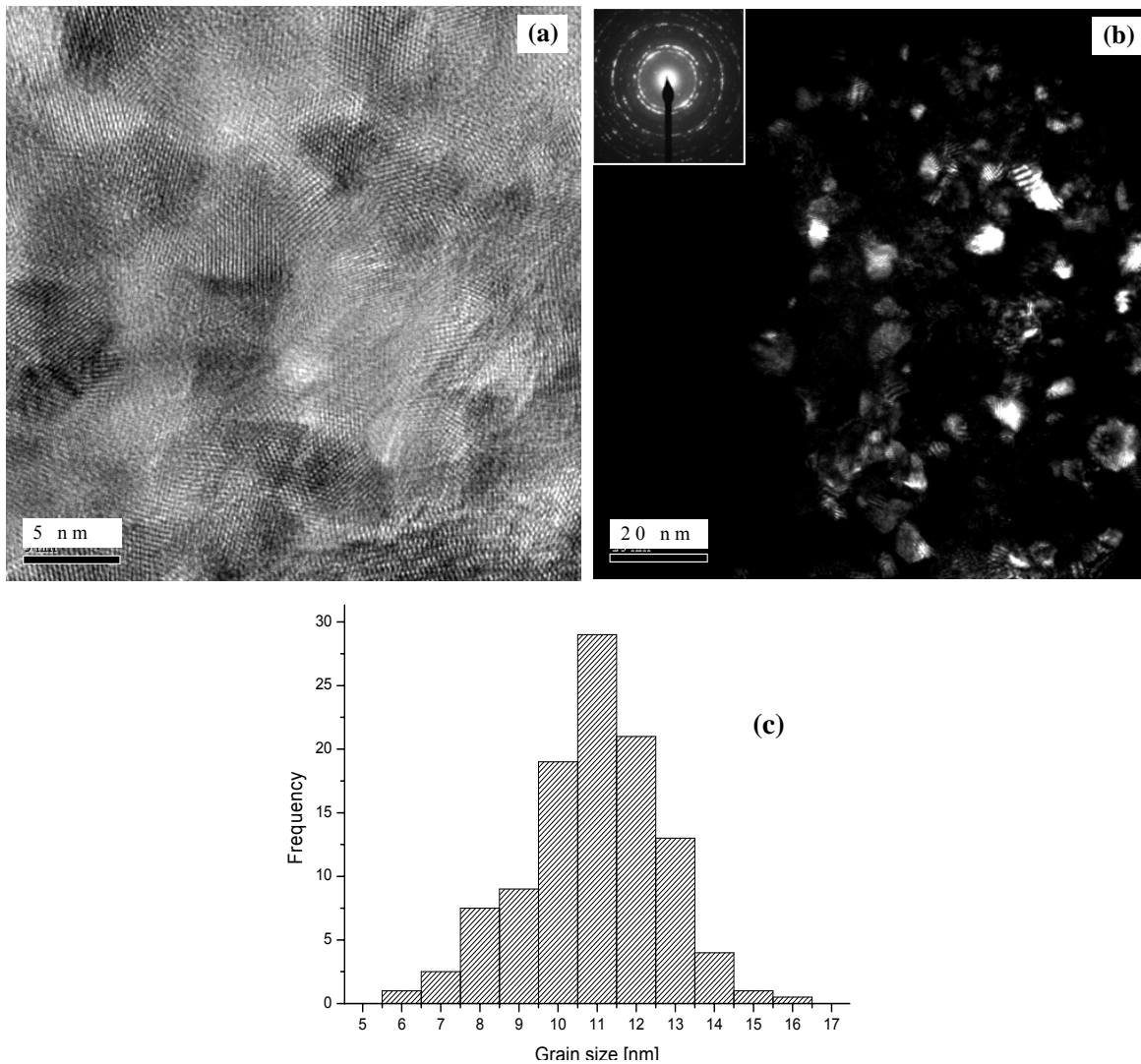


Figure 4.6: (a) HR-TEM micrograph of Ni that has been rolled for 80 passes and that has additionally been heated at 20 °C/min to 350°C followed by rapid cooling to room temperature. (b) Dark field TEM image corresponding to the HR-TEM shown in (a), indicating individual grains of about 10-12 nm in diameter. (c) Grain size distribution of the same sample.

In addition to the extensive grain refinement down to 10 nm, the HR-TEM analysis (Fig. 4.7) revealed that some larger - but still nanocrystalline grains (of about 30 nm in diameter) contained twins, although the material has a rather high stacking fault energy of about $\gamma_{sf} = 125 \text{ mJ/m}^2$ [Carter et al. 1977]. The corresponding dark field TEM image of the twinned grain is shown in Fig. 4.7 as an insert. Yet, careful examination showed only few twinned grains in nanocrystalline Ni after severe plastic deformation, which might partly be due to the multiple strain contrast in adjacent regions and due to the different orientations of the nanocrystalline grains that obstruct the observability of twins. Yamakov et al. (2002) have been proposed (by molecular

dynamics simulations) that deformation twin can form in high stacking fault energy, γ_{sf} , metal such as Al ($\gamma_{sf} = 120\text{--}142 \text{ mJ/m}^2$). Recently, Rosner et al. (2004) have observed twin in inert gas condensed nanocrystalline Pd ($\gamma_{sf} = 130\text{--}180 \text{ mJ/m}^2$) after a moderate deformation ($\epsilon = 0.32$) at a strain rate of 0.3 s^{-1} . In section 2.2.4, we described that when the dislocation splitting distance between two partials becomes comparable to the grain size, complete dislocations can no longer be nucleated from the grain boundary (GB). However, only a single $1/6[112]$ partial is nucleated from a GB or a triple junction; this partial dislocation subsequently glides through the grain interior, but it is still connected to the GB by the stacking fault left behind by the glide. Similarly when multiple single partial dislocations are nucleated from the same grain boundary and subsequently glide in consecutive parallel slip planes, a set of consecutive stacking faults is generated, which is basically a twin. Therefore, twins can form in metals with high stacking fault energy below a critical grain size.

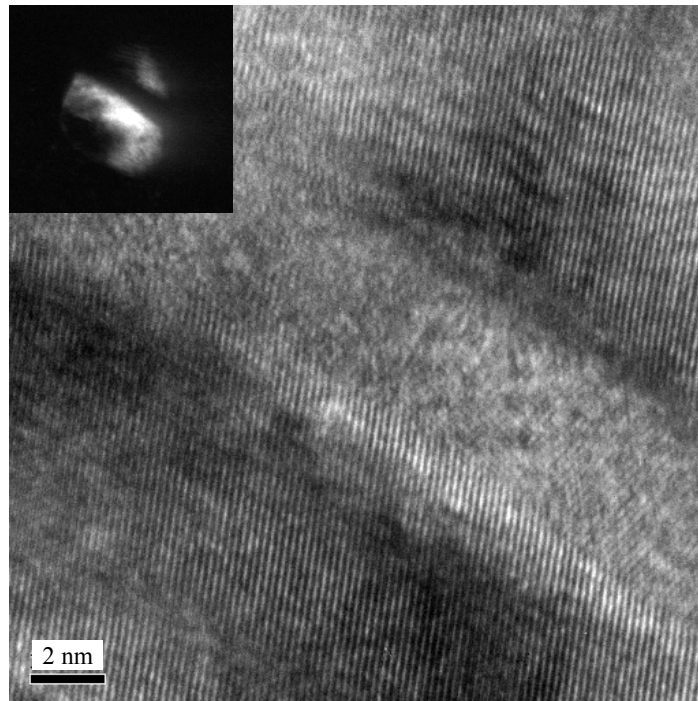


Figure 4.7: HR-TEM micrograph showing a deformation twin in a 30 nm Ni grain. Inset at the upper left corner shows the dark-field image of the twinned grain.

4.1.1.1 Sequential Combination of SPD Methods

One issue with cold rolling is that bonding at the interfaces is often not perfect, if – as in the present case – metals with melting points above 1700 K are deformed at room temperature and at low or moderate strain rates (compared to accumulative roll-bonding) of the order of 1 s^{-1} . Moreover, cold rolling inherently produces foils or sheets, i.e. materials that are less extended in one spatial direction. Thus, it is of interest to explore new processing pathways that potentially allow for synthesizing massive nanostructured materials. Fig. 4.8 shows a schematic representation of sequential combinations of different SPD processes for synthesizing massive nanostructured

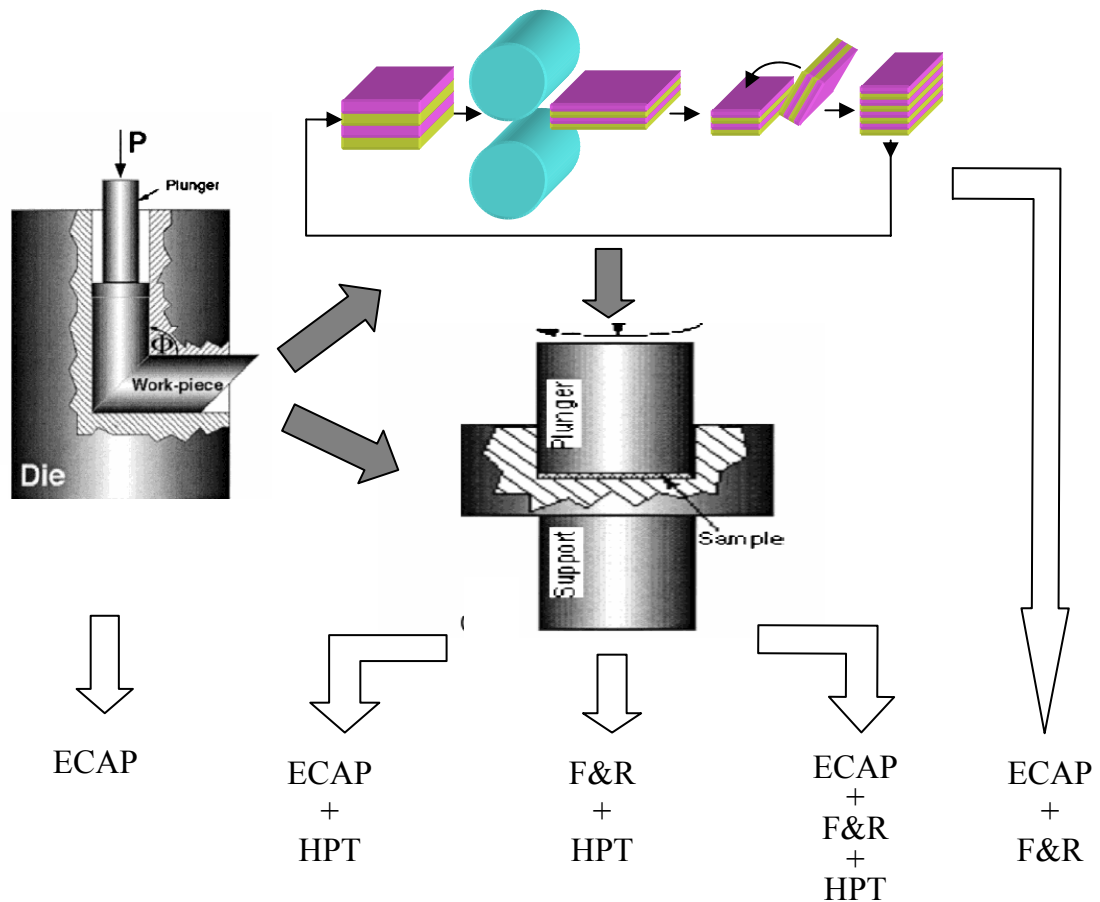


Fig. 4.8: Schematic representation of sequential combinations of different SPD processes for synthesizing massive nanostructured materials.

Table 4.1: Average grain size, true strain and hardness of Ni processed by different SPD routes.

	ECAP	HPT	F&R	F&R+HPT
True strain	~1 (for each pass)	~ 20 *	0.8 (after each folding)	-
Grain size (nm)	300 **	170 *	10 ***	40
Vickers Hardness (GPa)	2.45	3.5	5.77	6.57

* for 5 revolution of the sample having a thickness of 0.3 mm and the radius of 5 mm

** after 8 passes

*** after 80 F&R passes

materials. It should be noted that each SPD process has some limitations. For example, ECAP can produce large billets (up to 60 mm diameter and 200 mm long), however, the minimum grain size is around 300 nm for Ni. By contrast, the minimum grain size of HPT processed Ni is around 170 nm, but it has well-known limitation—overall sample dimensions are small (only up to 10 to 20 mm in diameter and up to 1 mm in thickness for a typical disc-shaped sample). On the other hand repeated cold rolling can produce large quantities (of the order of kilograms by industrial rolling mills) of nanocrystalline Ni of grain sizes below 10 nm, but the limitation is that the bonding at the interfaces is often not perfect. Therefore, combining SPD processing for example F&R+ECAP or F&R+HPT can produce large quantity of nanostructured materials of grain sizes below 50 nm. As one result it was observed that cold rolled material that was additionally processed by HPT at room temperature displayed full density and ductile behavior during deformation since no cracks occurred during the torsion deformation.

Fig. 4.9 shows a dark-field TEM overview (a) and a high-resolution image (b) of the microstructure of Ni after cold rolling (100 F&R) and subsequent high pressure torsion straining (diameter of the die, $d = 10$ mm, pressure, $p = 6$ GPa, 5 rotations ($\epsilon \approx 20$)) followed by annealing the sample at 300°C for a short time (heated from room temperature to 300°C by 20°C/min and subsequently cooled to 30°C by 150°C/min) to allow for some relaxation of the lattice defects to render the grain boundaries more observable. As shown in Fig. 4.9, the heat treatment did not result in flat grain boundaries, but instead the presence of grain boundaries with many kinks and facets is observed, as indicated by the white line in Fig. 4.9b. However, texture analysis by XRD methods indicate that the remaining rolling texture after extended folding and rolling

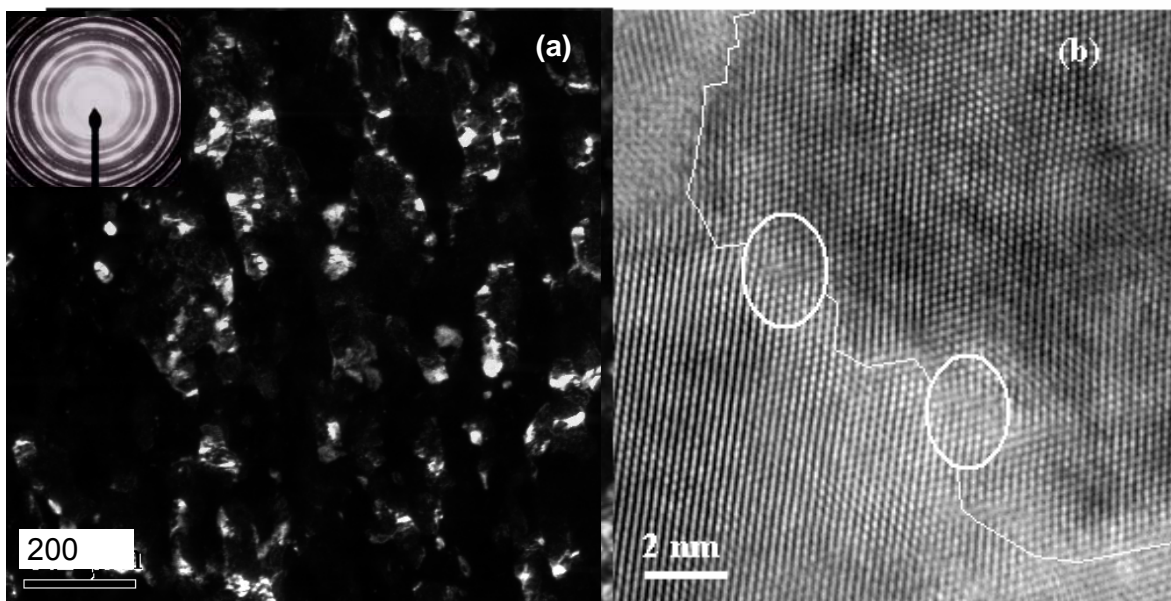


Figure 4.9: (a) Dark-field TEM image of Ni after cold rolling ($\epsilon = -80$) and HPT, followed by short annealing at 300°C. (b) HRTEM micrograph of the same sample. The circle marks a dislocation situated at the grain boundary of two nanocrystalline grains. The white line indicated the grain boundary of the grain in the upper right corner of the image.

decreased rapidly during HPT and hardness (Table 4.1) measurements show a significant increase of the hardness after additional HPT. Additional tests are required to examine whether the increase of the average grain size or the loss of texturing (and the associated increase of the fraction of large-angle grain boundaries) are responsible for the hardness increase. From table 4.1, it can be seen that the Vickers hardness of Ni (80 F&R) after an additional HPT operation is 6.57 GPa, which is six times higher than microcrystalline Ni and almost twice the value of HPT Ni (see Fig. 4.10). The Vickers hardness test were performed in collaboration with Prof. R. Z. Valiev, Institute of Physics of Advanced Materials, Ufa State Aviation Technical University, Russia. It should be noted that the hardness value of electrodeposited Ni of grain size 10 nm is about 6 GPa. To further clarify the very high hardness of cold-rolled Ni an additional nanoindentation experiment has been performed in collaboration with Dr. Norbert Huber, IMF-II, Forschungszentrum Karlsruhe. It has been found that the hardness, measured by nanoindentation of Ni (80 F&R + HPT) is 7 GPa, which is little (8 %) higher than Vickers hardness test. However, the Youngs modulus, determined from nanoindentation study, of the same Ni sample is 190 GPa, which is almost the same as that of coarse grained Ni (200 GPa). Therefore, Ni displays almost similar elastic behavior in micro- or nano- crystalline grain sizes regimes.

On the other hand, it was also found that an initial ECAP treatment did not change the grain size obtained by cold rolling for up to 100 passes. Because ECAP reduces the grain size up to 300-350 nm. However after only 20 F&R passes the grain size is reduced to 200-400 nm from a starting initial grain size of 50 μm . Therefore, an ECAP treatment before cold rolling does not affect the final microstructure, but reduces the necessary rolling and folding repetition by 20 F&R passes for the synthesis of materials below 100 nm. On the other hand, if severely cold rolled samples can be further processed by ECAP and if 100% density can be achieved, then the combination of F&R+ECAP will become a promising route for synthesizing massive nanostructured materials.

4.1.1.2 The Hall-Petch plot of hardness of Ni

Recent experimental work for the strength or hardness behaviour of nanocrystalline materials revealed a deviation from the classical Hall-Petch equation. While some workers have suggested that the Hall-Petch behaviour is still valid up to very small grain sizes (with the difference that the Hall-Petch slope is in all cases lower than the one for the coarse grain specimens), others have observed even negative Hall-Petch slopes. The hardness values of severely cold-rolled Ni are plotted as a function of grain size in Fig 4.10. For comparison, this plot also contains hardness data from different literature. The highest hardness of ~ 7 Gpa is observed at a grain size of about 40 nm in our cold-rolled + HPT Ni. However, the smallest grain sizes of about 10 nm, our data show a significant decrease in hardness, consistent with the inverse Hall-Petch effect expected at these grain sizes. However, it is difficult to find out the cross-over from Hall-Petch to inverse Hall-Petch region because there are not enough experimental data between the grain sizes from 100 nm to 5 nm. Moreover, the hardness values of nanocrystalline Ni is not completely reliable due to artefacts (sulphur impurities at the grain boundaries) of electrodeposited samples. Therefore, hardness

measurements of artefact-free Ni of grain sizes from 100 nm to 5 nm are necessary to find out the exact Hall-Petch slope and the strongest grain size of Ni.

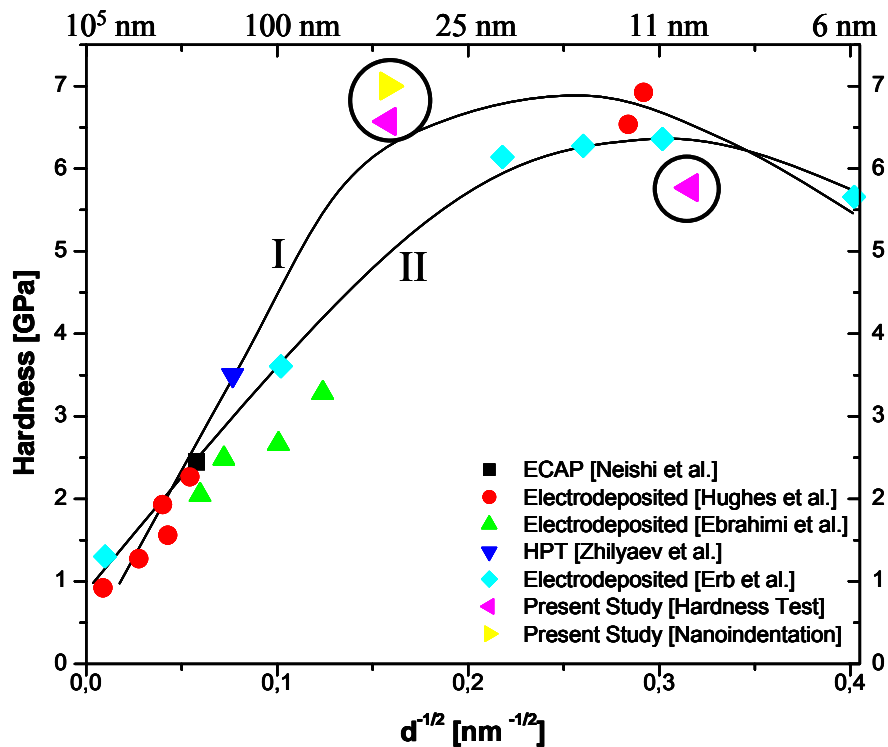


Figure 4.10: Hall-Petch plot of hardness of Ni against the inverse square root of grain size. The present result are compared with literature data of different grain sizes.

4.1.1.3 Thermal Stability

Fig. 4.11a shows a dark-field TEM overview of Ni after cold rolling (80 F&R) and subsequent high pressure torsion straining. It is important to note that the additional deformation under high pressure resulted in an appreciable increase of the average grain size from $\bar{D} = 8$ nm to $\bar{D} = 40$ nm, probably due to dynamic recrystallization or strain induced grain growth. A series of heat treatments have been performed to determine the thermal stability of the severely deformed Ni. No grain growth was observed up to 350 °C. An additional annealing at 365 °C for 5 minutes caused very little coarsening. It can be seen from figure 4.11b that the average grain size increased only marginally, from 40 nm to about 50 nm after the thermal treatment. As cold-rolled Ni ($\bar{D} = 10$ nm) grains start to grow at 350 °C and the average grain size become 50 nm after 5 minutes annealing at 365 °C. It has been recently found [Wang et al. 2002] that controlled heat treatment of cold-rolled Cu leads to a bimodal grain growth (few grains grow abnormally up to the μm range, whereas the majority of the grains remain in the nanocrystalline range) after a short annealing at 200 °C for 3 minutes. However in the present study we did not observe any abnormal grain growth of Ni after annealing at same homologous temperature than that of Cu in the experiments by [Wang et al. 2002].

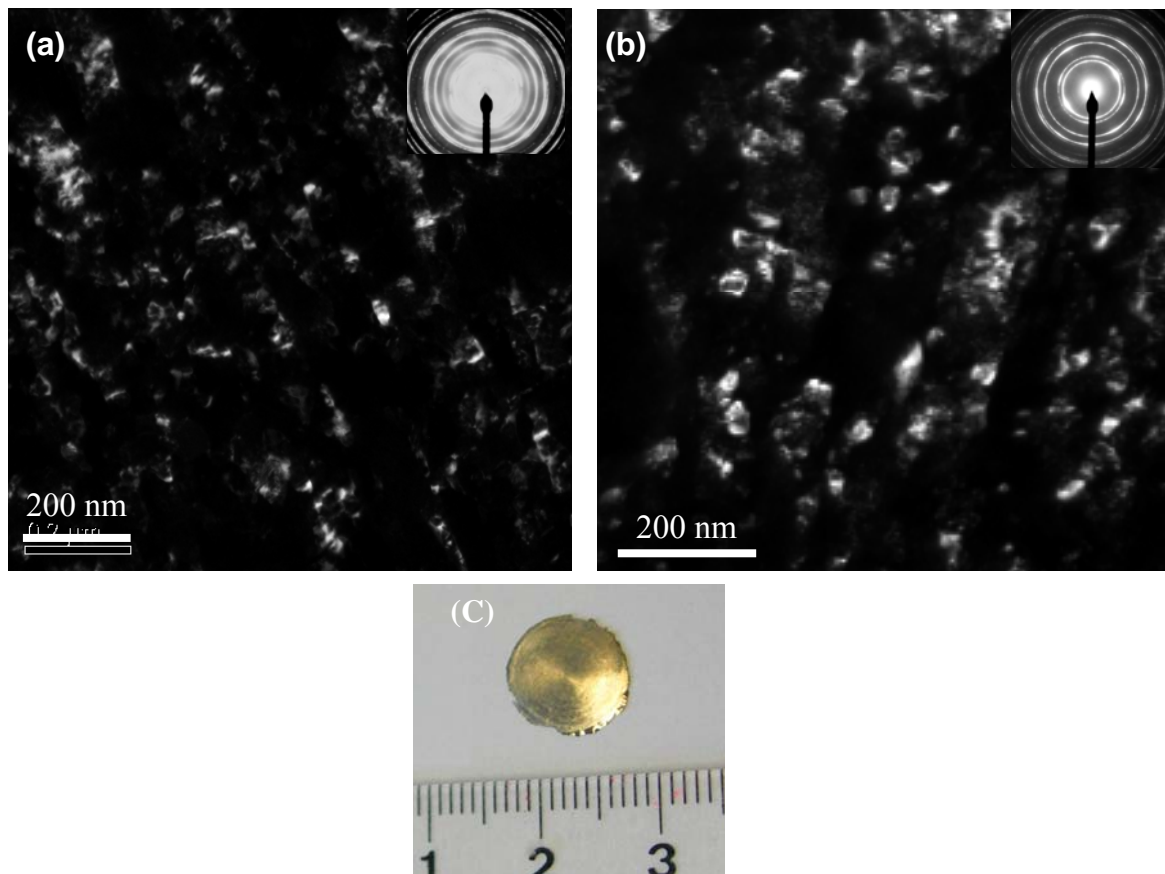


Figure 4.11: (a) Dark-field TEM micrograph of Ni that has been rolled for 80 passes and subsequent HPT straining. (b) Dark-field TEM image of Ni (80 F&R + HPT) after annealing at 365°C for 5 min. (c) Cold rolled Ni (80 F&R) after additional HPT.

4.1.2 Elemental Pd (fcc)

For a better understanding of the microstructural refinement process by repeated cold-rolling, another fcc metal (Pd) has been deformed analogously. It was found that the microstructural developments are quite similar to that of Ni at different deformation stages. Fig. 4.12 shows the XRD scan of an as-rolled multilayer sample (Pd) after different F&R cycles. Initially the intensity of the Bragg peaks of the elements gradually decreased and the peaks broadened with an increasing number of rolling passes due to the refinement of the crystallite size and the build-up of internal lattice strain, which are the characteristics of all plastic deformation processes. Additionally, the intensity of the (111) and (200) Bragg peaks strongly increased at the initial stage of cold-rolling indicating the formation of a strong rolling texture during cold-rolling. However, the relative intensities of (111) and (200) gradually decreased after 100 F&R, indicating the decreasing of the rolling texture. The texture development during repeated cold rolling of Pd is similar (intensity ratio of (111)/(220)) to that of Ni. However, the XRD analysis shows that a much stronger rolling texture developed in Ni compared to Pd although both the elements have the same crystal structure (fcc). It should be noted that a θ — 2θ XRD scan is useful only to know whether texture is developed in the sample during deformation. However, the exact texture component and the intensity of the texture can be best understood by pole figures and ODF (orientation distribution function) analysis.

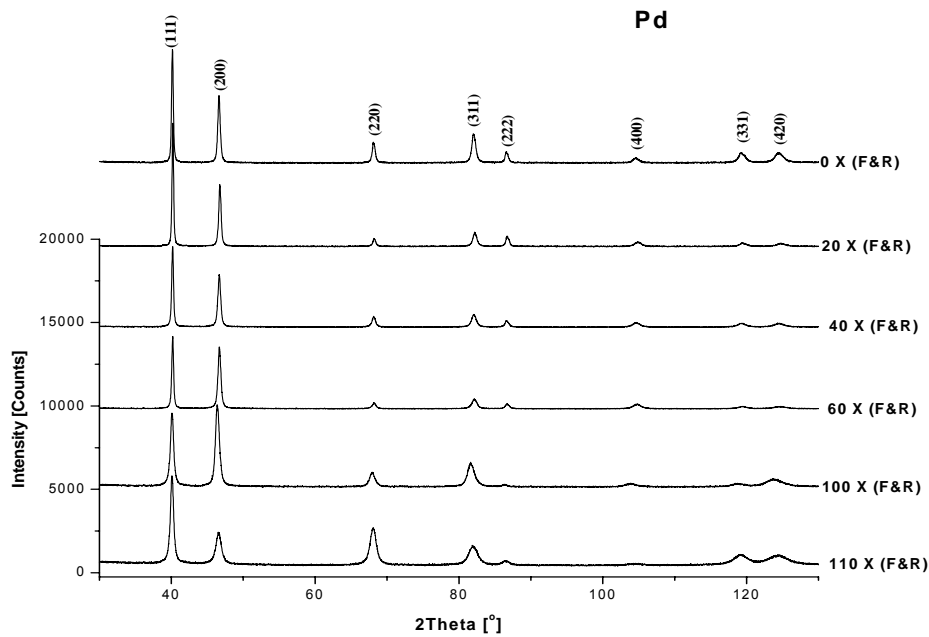


Figure 4.12: (a) XRD scans of as-rolled multilayer samples (Pd) after different F&R cycles as indicated in the figure.

Grain refinement is less extensive for the case of Pd compared to Ni. The final average grain size which was achieved after 100 F&R is around 50 nm which is 5-6 times larger than Ni after the same amount of deformation. However many kinks and facets are observed in the grain boundaries of severely deformed Pd. Fig. 4.13 shows the HRTEM image of a Pd sample after 105 folding and rolling treatments, corresponding to an equivalent strain of about $\epsilon = -85$. More clearly, the rough interface morphology is observed on as-deformed Pd-samples after cold rolling. The contrast between the two adjacent grains is higher in this case, since the upper grain is oriented in a $\langle 100 \rangle$ zone axis, allowing to observe a full lattice image of Pd after severe

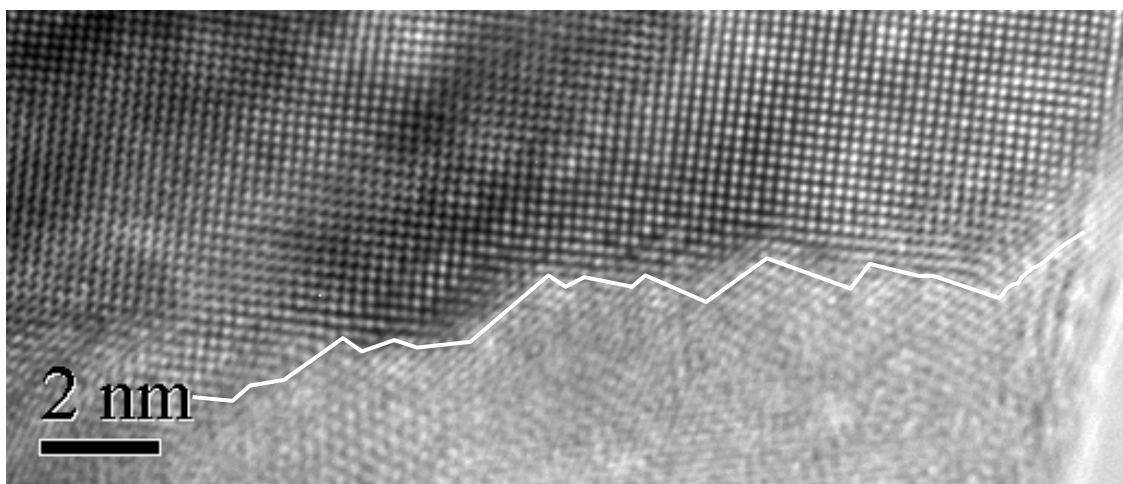


Figure 4.13: HRTEM image of Pd after severe deformation (105 F&R). The white line indicates the position of the grain boundary between the upper grain (in $\langle 100 \rangle$ orientation) and the lower grain.

deformation while the lower grain is oriented in an off-Bragg condition with the incident electron beam. In addition to the rough interfaces that resemble the “non-equilibrium” grain boundaries as described by Valiev (2004), a very high density of lattice defects has been detected, including a high dislocation density at the grain boundaries and within the crystallites. Another additional microstructural finding is that many stacking faults are observed in severely deformed Pd after 105 F&R passes (Fig. 4.14). Recently, Rosner et al. (2004) observed deformation twin in nanocrystalline Pd. It is surprising to observe a large number of stacking faults or twin in metals like Pd which has a very high stacking fault energy ($130\text{-}180\text{ mJm}^{-2}$) [Rosner et al. 2004]. It should be noted that the 105-F&R Pd contain no metallic impurities (EDX-measurements by TEM). However, hot extraction measurement revealed that the around 0.1 wt. % Oxygen is present in the severely cold-rolled (105-F&R) Pd sample.

The deformation mechanisms of nanocrystalline materials differ from those of coarse-grained materials. In section 2.2.4, we described that complete dislocations can no longer be nucleated from grain boundaries (GB) when the dislocation splitting distance between two partials become comparable to the grain size. However, if the applied stress is sufficiently high (dislocation nucleation stress is inversely proportional to grain size) only a single partial can be nucleated from a GB or a triple junction; this partial dislocation subsequently glides through the grain interior, but it is still connected to the GB by the stacking fault left behind by the glide. Therefore, below a critical grain size, which is nearly the equilibrium distance between two partials, a stacking fault can be observed in high stacking fault energy metals such as Ni and Pd due to single partial dislocation motion through the grain.

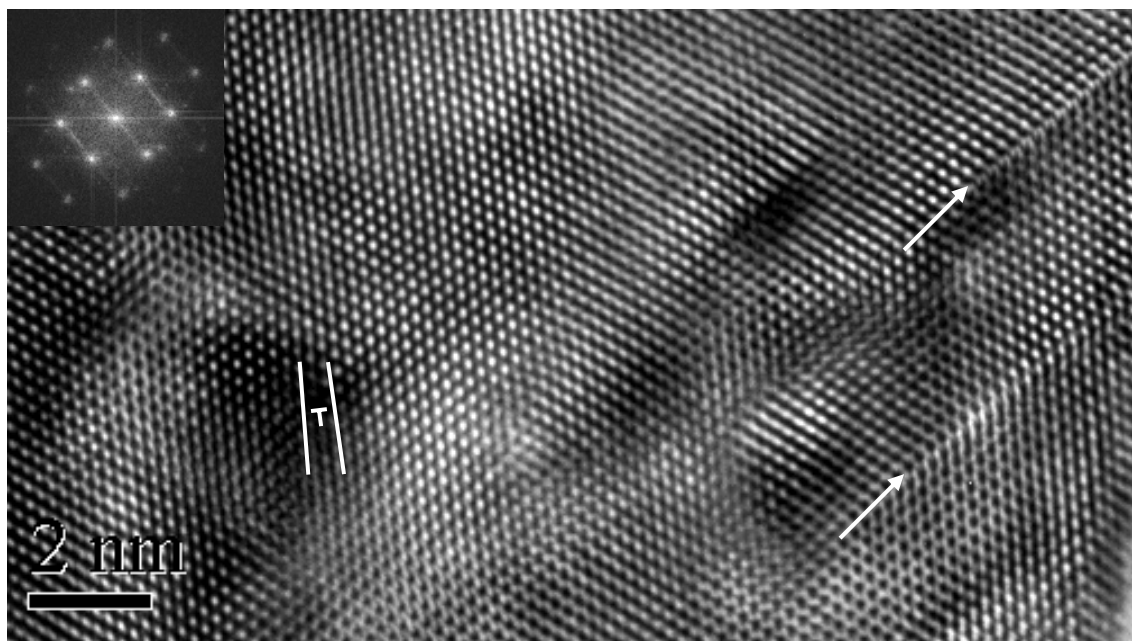


Figure 4.14: HRTEM image of Pd after severe deformation (105 F&R) showing a grain in $\langle 110 \rangle$ orientation. Many stacking faults (\rightarrow) and dislocations (\perp) are present in the microstructure. The insert in upper left corner shows the corresponding fourier transform showing the reflections of a $\langle 110 \rangle$ zone axis.

4.1.3 Elemental Ti (hcp) & Zr (hcp)

Metals with an hcp-structure such as Ti and Zr have been treated analogously and they present basically a similar deformation behaviour coupled to an analogous microstructure development that is governed by layer-thickness decrease, grain-size decrease and – at the latest stage – by a pronounced decrease of the texturing. Figures 4.15 and 4.16 show the XRD scan of an as-rolled multilayer sample of Ti and Zr respectively after different F&R cycles. As expected for plastic deformation processes, the Bragg peaks gradually decrease and the peaks broaden with an increasing number of rolling passes due to the refinement of the crystallite size and the build-up of micro-strain. At the same time it has been observed that after 10 F&R passes, the relative intensities of the (002) Bragg peak strongly increased and the other Bragg peaks almost vanished after 30 F&R passes for Ti and after 40 F&R passes for Zr, indicating the formation of a strong rolling texture.

For hcp metals the basal plane tends to be parallel with the rolling plane. As expected from cold rolling, we found that extensive cold rolling leads to the formation of a (002) basal texture in both Ti and Zr due to the strong increase of the (002) Bragg peak. This result indicates a dominance of dislocation processes during the early stages of the deformation process. Additionally, further rolling up to 100 F&R passes shows that the other Bragg peaks gradually increased after 80 F&R passes, indicating random grain orientation at that stage of deformation. This later stage of the overall deformation process proceeds at a decreased grain size. Thus, the local deformation mechanism may change and grain boundary sliding and grain rotation can become active, which would lead to a gradual decrease of the texture with continued plastic deformation. However, XRD scans after 100 F&R show that the sample is not totally texture free. For a detail understanding of the amount of the residual texture components and their intensity, pole figure and ODF (orientation distribution function) analysis would be needed.

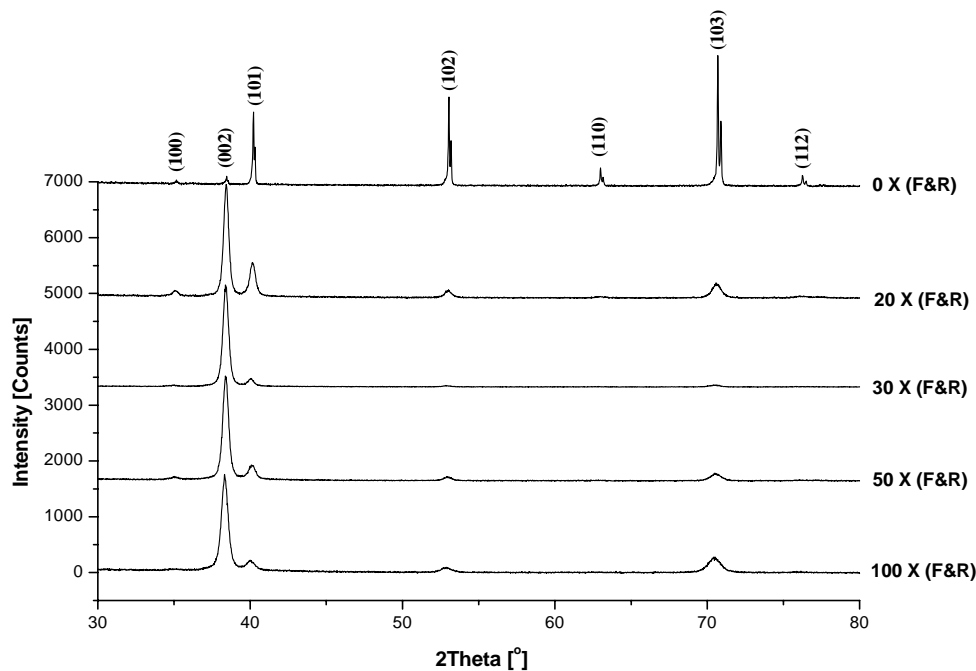


Figure 4.15: XRD scan of as-rolled multilayer samples (Ti) after different F&R cycles as indicated in the figure.

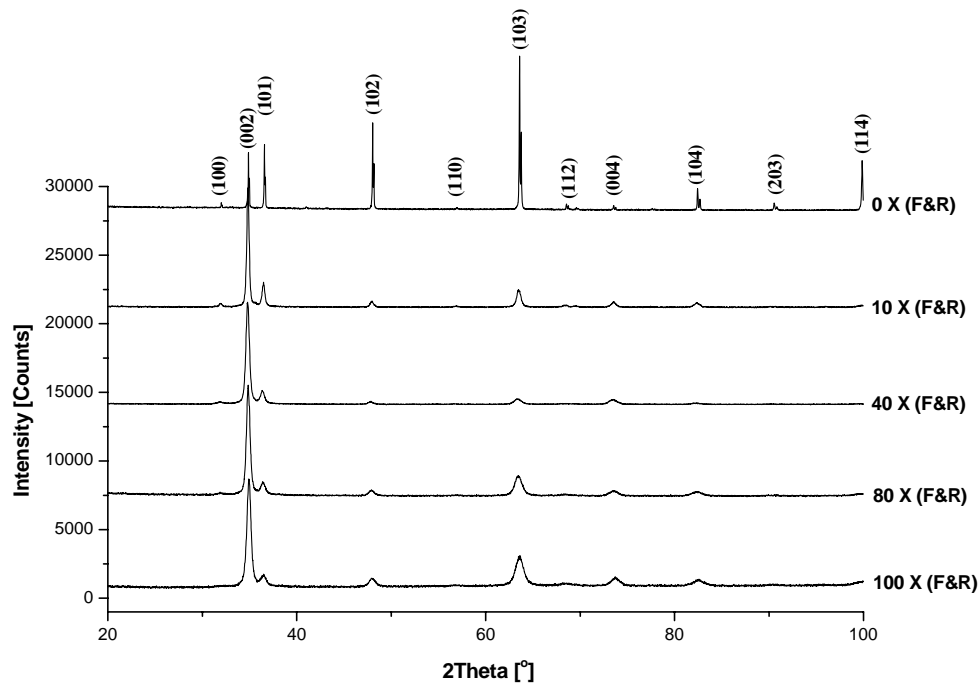


Figure 4.16: XRD scan of as-rolled multilayer samples (Zr) after different F&R cycles as indicated in the figure.

The microstructure after large deformation was additionally investigated by TEM. Dark field micrographs of Zr and Ti after 80 F&R passes are shown in Fig. 4.17. SAED patterns (insets in Fig. 4.17), obtained from regions with a diameter of 1.3 μm show a ring-like pattern indicating ultra-fine grains. It can be seen from Fig. 4.17 that the microstructure of severely deformed (80 passes) Zr and Ti consists of a dense array of nanocrystalline grains with an average grain size of approximately 80 nm. Quantitative analyses of the TEM dark-field images of about 100 grains, measuring always the largest diameter and the diameter in the direction perpendicular to the long axis, showed that the grain size distribution is fairly narrow compared to the distributions obtained by alternative SPD-techniques. For the Zr and Ti samples, the grain size was found to be $80 \text{ nm} \pm 40 \text{ nm}$ after 80 F&R passes. Thus, the grain size at this deformation stage is considerably larger for the hcp-metals compared to Ni (with fcc structure). Since grain subdivision occurs by movement and accumulation of dislocations, grain refinement by plastic deformation should proceed more efficiently in systems, e.g. fcc metals, with a larger number of active slip systems (or slip systems that can become active). The different possible slip systems in fcc, hcp and bcc structure have been described in section 2.2.1. In the fcc metals, slip occurs on $\{111\}$ planes and in the $\langle 110 \rangle$ directions. There are only four sets of $\{111\}$ planes. Each $\{111\}$ plane contains three $\langle 110 \rangle$ directions. Therefore, the fcc lattice has 12 possible slip systems. On the other hand, in hcp metals slip occurs only in (0001) basal plane and in the $\langle 11\bar{2}0 \rangle$ directions. Since there is only one basal plane per unit cell and three $\langle 11\bar{2}0 \rangle$ directions, the hcp structure possesses three slip systems. Therefore, during plastic deformation of fcc structures, slip can take place in 12 possible directions and eventually forms a complex 3-dimensional dislocation network, which then forms a dislocation cell or subgrain structure after additional deformation. Whereas in hcp metal

glide occurs only on one plane (basal plane) and in three possible directions. Therefore, the generation of a dislocation network is less extensive in hcp metals compared to fcc metals. Thus, the present results suggest that grain refinement under given boundary conditions such as temperature, applied pressure and strain and strain rate depends on the total number of slip systems that can become active during deformation. This explanation indicates that smaller average grain sizes are achievable at higher strain values, which has been confirmed experimentally: after 120 F&R passes, the average grain diameter for Ti was obtained as 50 nm (Fig. 4.18). Thus, even for systems with a smaller number of active slip systems, a truly nanocrystalline microstructure can be obtained if the amount of strain is increased.

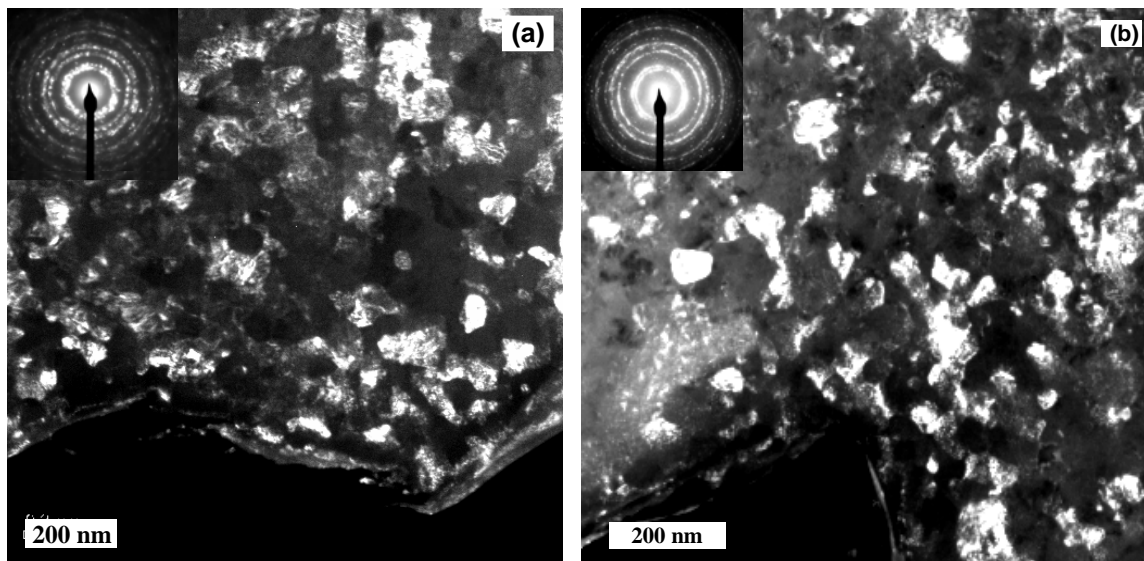


Figure 4.17: Dark field TEM images with corresponding SAED as an insert of (a) Zr and (b) Ti after 80 F&R passes.

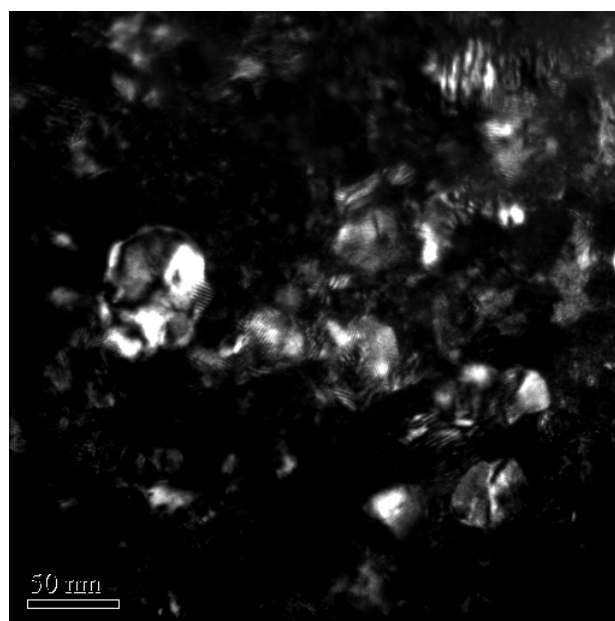


Figure 4.18: Dark field TEM image of Ti and after 120 F&R passes.

4.1.4 Cold-rolling of Zr at low (below $-100\text{ }^{\circ}\text{C}$) temperature

For a clear understanding of the grain refinement process by plastic deformation, a pure Zr sample has been rolled with liquid nitrogen cooling of the workpiece between consecutive rolling passes and during the rolling reformation. The sample was rolled at a strain rate of 0.5 s^{-1} by directing a flow of liquid nitrogen on the sample and roller surface during deformation and sample handling. The temperature ($-150\text{ }^{\circ}\text{C}$ and $-100\text{ }^{\circ}\text{C}$ before and after each pass, respectively) of rolling was estimated by Wang et al (2002) in a similar experiment. The aim of the low temperature rolling is to compare the grain refinement rate at low-temperature (LT) rolling as compared to room temperature rolling. Fig. 4.19 shows the dark field TEM image of Zr that has been rolled at LT for 8 F&R passes. It can be seen from Fig. 4.19a that the microstructure consists of a dense array of equiaxed nanocrystalline grains with an average grain size of approximately 100 nm. It should be mentioned that the grain refinement took place quite faster at LT compared to room temperature rolling. The average grain size after 8 F&R passes at LT rolling becomes 100 nm, whereas after the same amount (8 F&R) of deformation at room temperature we observed typical average grain sizes around 500 nm. Moreover, it is required to roll up to 70-80 F&R passes at room temperature to reduce the grain size down to 100 nm. Fig. 4.19b shows the details of an individual grain with bend-like structure due to an inhomogeneous distribution of the residual strain. The HR-TEM analysis (Fig. 4.20) shows the presence of a huge lattice defect density (dislocation) in the LT rolled Zr. The use of the low temperature suppresses dynamic recovery, allowing the density of the accumulated dislocations to reach a higher steady-state level than that achievable at room temperature. It should be noted that we can only observe the microstructure after plastic deformation was ended and after the sample has been thinned to become electron transparent. Thus, it can be safely assumed that the dislocation density was higher during or shortly after rolling because of some dislocation annihilation during TEM sample preparation (ion milling). Heavily cold-worked metals contain a dislocation density of about 10^{14} to 10^{16} m^{-2} [Dieter 1988].

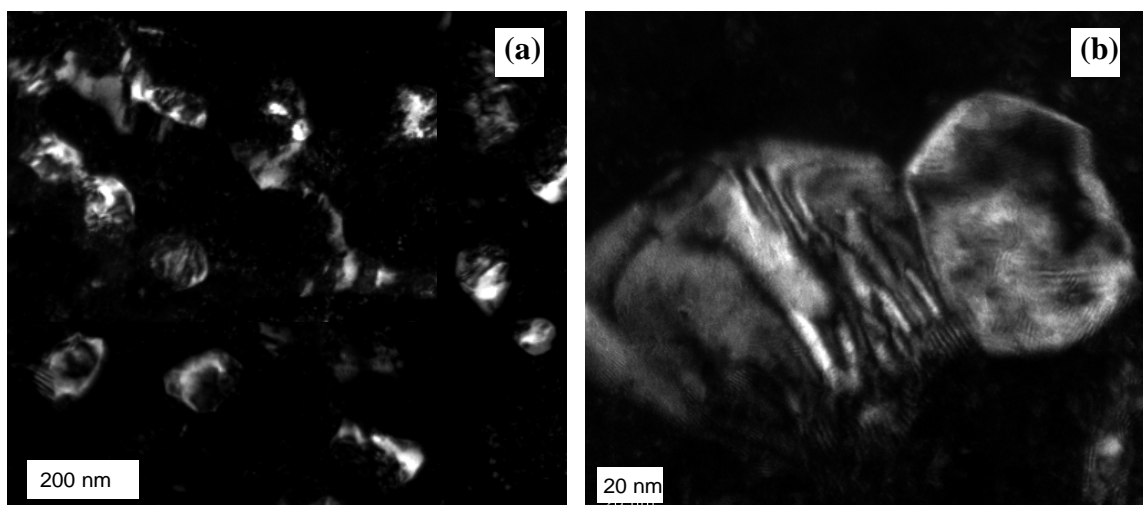


Figure 4.19: Dark field TEM images of Zr (a) the sample is continuously cooled by spraying liquid nitrogen on the workpiece and subsequently rolled for 8 F&R passes. (b) details of a individual grain.

However, in the present study, we estimated the dislocation density of LT rolled Zr to be around $5 \times 10^{16} \text{ m}^{-2}$ which is at the maximum limit of the dislocation density of cold rolled metals. Therefore, it is true that we can increase the equilibrium dislocation density in metals when rolled at low temperatures. A very large number of dislocations at low temperature can explain the faster grain refinement by forming cell or sub-grain structures which is less extensive due to faster dynamic recovery at room temperature.

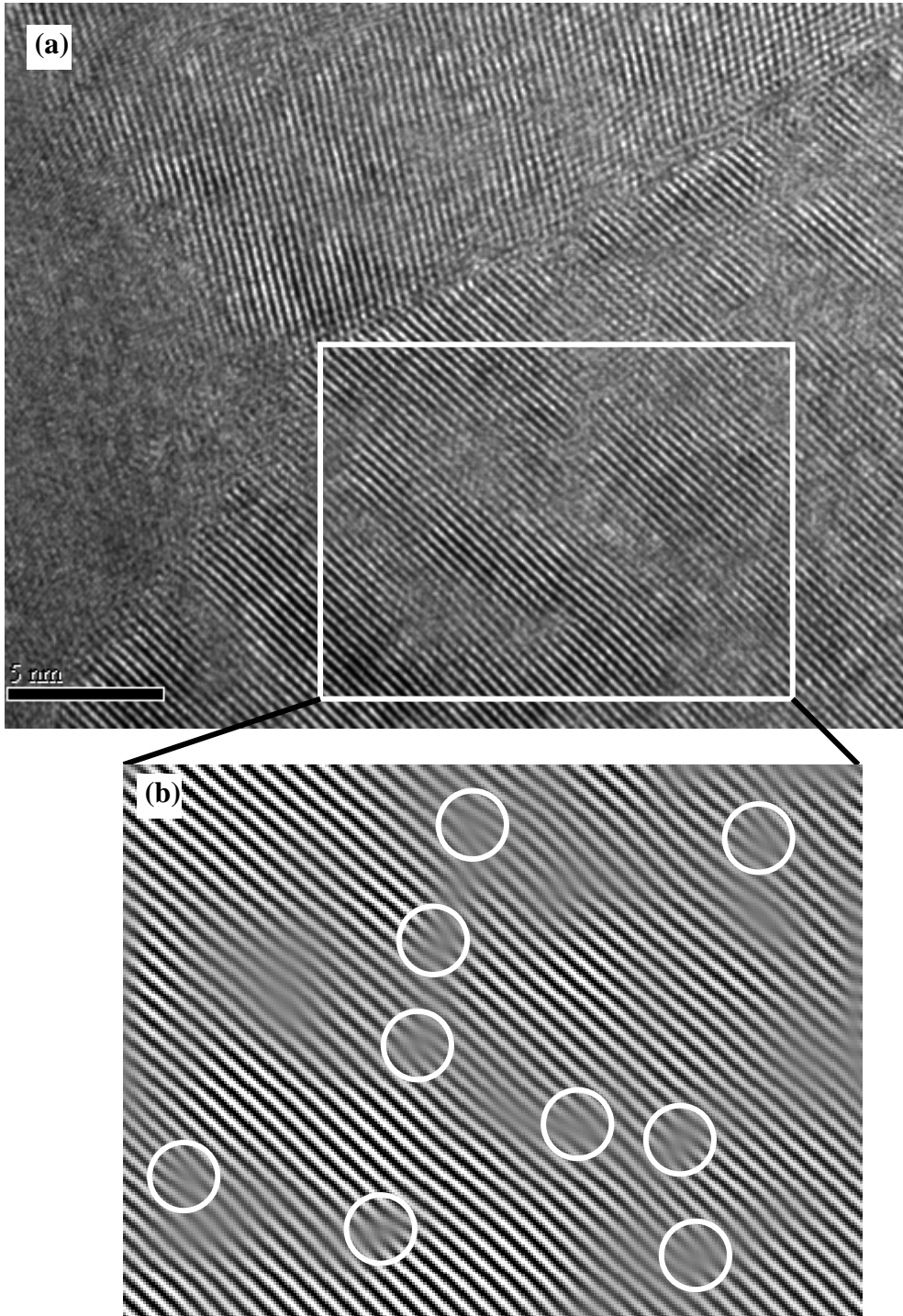


Figure 4.20: HRTEM images of Zr (a) after liquid nitrogen cooled rolling (8 F&R) shows the presence of huge lattice defect (dislocations). (b) Micrograph with a higher magnification of the selected area of figure a.

4.2 Discussion

The results on the evolution of the microstructure of pure metals indicates that the repeated F&R technique is an alternative SPD technique that is capable of producing extremely fine nanocrystalline material at ambient temperature. It is shown in Fig. 4.4 that repeated F&R leads to a significant refinement of the multilayer structure in all cold-rolled samples. The average layer thickness achieved after 100 F&R passes ($\epsilon \approx -80$) is below 50 nm in pure Ni, Ti and Zr. In previous work, the synthesis of bulk ultrafine-grained samples of pure metals by SPD techniques was mostly limited to grain sizes larger than 100 nm. However, in the present investigations, bulk nanocrystalline samples of Ti and Zr consisting of grains considerably smaller than 100 nm in diameter could be synthesized. In fact, the grain size achieved in pure Ni is about 7–8 nm with a very narrow grain size distribution (Fig. 4.5b). To the authors' knowledge, average grain sizes less than 10 nm in pure Ni have not been obtained by any other SPD technique. Moreover, the plane-view TEM micrographs as well as the SEM images of the fracture surfaces together with the XRD-results that indicate the disappearance of the rolling texture after severe deformation (and corresponding grain-size reduction) indicate that the resulting grains are equiaxed. As indicated by Fig. 4.5 and Fig. 4.17, large differences in the final grain size at similar total deformation are observed between the two hexagonal close packed (hcp) metals Zr and Ti and the face-centered cubic (fcc) metal Ni. It is explained that grain refinement by plastic deformation should proceed more efficiently in systems with a larger number of active slip systems. Since the fcc structure possesses more (12) slip systems compared to the hcp (3) structure, grain refinement takes place more extensively in fcc metals compared to hcp metals.

Recently, Valiev et al. (2003) as well as Zehetbauer et al. (2003) reported independently that the high imposed pressure during high pressure torsion reduces the diffusion coefficient for vacancy diffusion, which reduces the probability of dislocation annihilation. Therefore, a high equilibrium density of dislocations can be stored when deformation takes place under a high applied pressure. According to their model, a high applied pressure plays the major role to reduce the steady-state grain size and thus the finally achievable grain size via severe plastic deformation. However, the present results indicate that the main key to produce such fine nanocrystalline structures seems to be the application of a large plastic strain but not necessarily involving a high applied hydrostatic pressure, as e.g. in high-pressure torsion straining. Although the rolling deformation also consists of a hydrostatic pressure component in addition to shear that is estimated as about 500 MPa at maximum for Ni, Pd, Ti and Zr [Dieter 1988], this value is low compared to SPD techniques such as HPT or equal-channel angular extrusion. Certainly, the pressure is too low to result in a considerable decrease of the vacancy diffusion coefficient as assumed in Ref. [Zehetbauer et al. 2003] to explain the possibility of nanostructure formation by severe plastic deformation under high hydrostatic pressure conditions.

4.2.1 Mechanisms for formation of nanocrystalline microstructures by repeated cold-Rolling

The formation of a nanocrystalline microstructure during intense cold rolling can be explained in terms of dislocation generation and rearrangement to form a cell- or subgrain structure followed by grain boundary sliding and grain rotation during further deformation, which is the most probable deformation mechanism in extremely fine nanocrystalline materials. The grain refinement processes at different stages of deformation are schematically shown in figure 4.21. In the initial stages of rolling, deformation proceeds via dislocation motion. Consequently, the early stages of the F&R deformation process are dominated by the thickness reduction of the individual layers together with the formation of a pronounced rolling texture (Fig. 4.21b). During rolling, metal flows in two directions (rolling and transverse directions), therefore, parent grains become elongated at the early stages of deformation. With continued deformation, the defect (dislocation) accumulation within the elongated grain structure favours grain subdivision to reduce the strain energy, which becomes extensive after intense deformation due to multiple dislocation generation and rearrangement to form a cell – or subgrain structure (Fig. 4.21c). The plastic deformation of coarse-grained metals at relatively low temperature is usually mediated by the nucleation and motion of dislocations. However, for nanocrystalline metals, dislocation sources and pile-ups are not expected to exist within the individual grains because of the limited grain size and

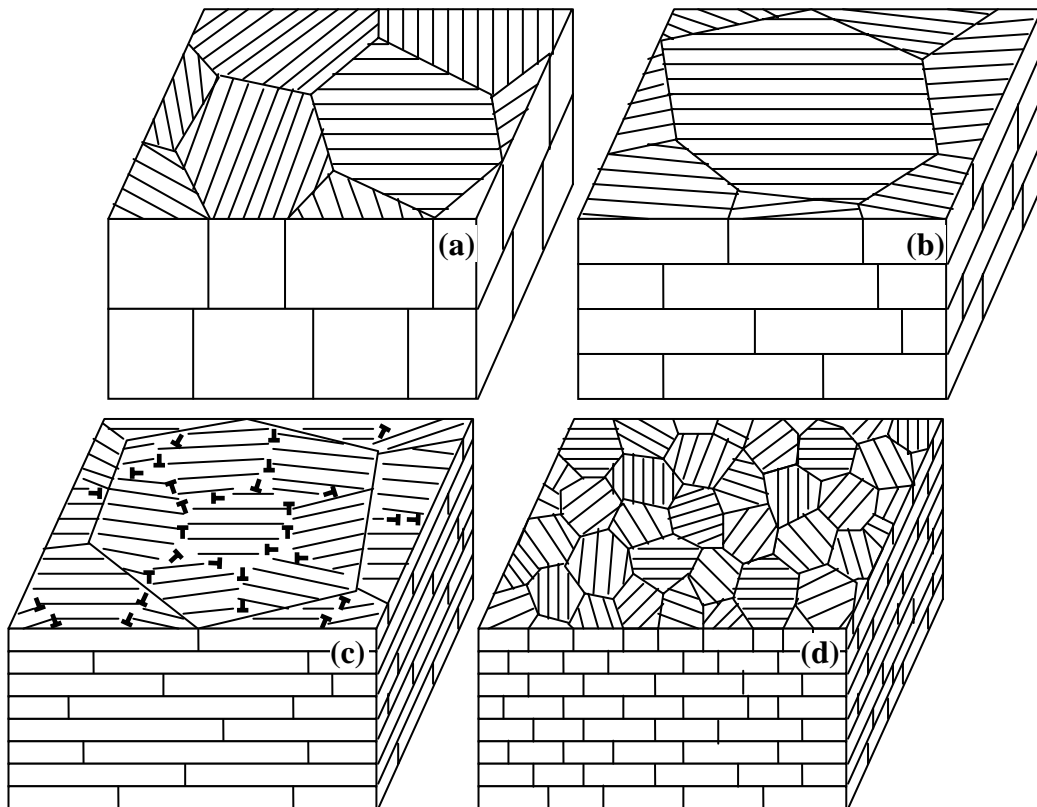


Figure 4.21: Schematic development of layer thickness, texture and grain size at different stages of repeated cold-rolling.

the much higher fraction of grain boundary (GB) atoms. It has been proposed [Swygenhoven 2002, Schiotz et al. 1998] that GB-mediated plasticity (e.g., GB sliding and/or grain rotation) substitutes for conventional dislocation nucleation and motion as the dominant deformation mechanism when grain sizes are reduced below a certain value. Therefore, at the final stages of rolling, when the grain size becomes < 20 nm, plastic deformation most probably proceeds via GB sliding and/or grain rotation, which is essentially responsible for the development of near-equiaxed grains and reduced rolling texture (Fig. 4.21d).

On the basis of the present results, we propose that the main key to produce fine nanocrystalline structures seems to be the requirement of a large plastic strain, which can produce more dislocation, therefore, more grain boundaries, but not necessarily involving a high applied hydrostatic pressure, as e.g. in high-pressure torsion straining. The more dislocation are produced and stored, the more grain boundaries can be built from them. Rolling of Zr at a low temperature supports this arguments. Due to the low working temperature, the dynamic recovery is reduced, which increases the equilibrium dislocation density, therefore, faster grain refinement is possible at low temperature rolling. Therefore, it should be noted that, the lower the working temperature, the faster the grain refinement rates. Therefore, rolling at room temperature took more time for the same amount of grain refinement compared to rolling at liquid temperature.

4.3 Synthesis of nanocrystalline alloys

4.3.1 Grain refinement of Ni₅₀Ti₅₀ elemental multilayers

So far the focus was on the grain refinement process of pure metals. This section will report the experimental investigation of grain refinement processes of multilayer composites. Elemental foils of Ni and Ti (purity $\geq 99.98\%$) with a thickness between 25 and 27 μm were stacked to form arrays of the composition Ni₅₀Ti₅₀ and then these stacks were continuously cold-rolled up to 80 F&R passes. The evolution of the bulk nanocrystalline Ni₅₀Ti₅₀ samples at different stages of the plastic deformation starting from a layered array of individual elemental sheets and investigated by X-ray diffraction are shown in Fig. 4.22. Initially the intensity of the Bragg peaks of the elemental constituents gradually decreased and the peaks broadened with increasing number of F&R-passes due to the simultaneous refinement of the grain size. Additionally, the XRD results that were obtained on the early stages of the deformation procedure, i.e. at strain levels lower than $\epsilon \approx -30$ (40 F&R passes) when the samples still reveal clear Bragg peaks. Moreover, the XRD-results clearly show the absence of any formation of a new phase in the multilayer samples during the rolling procedure. When the deformation was continued for more than 40 F&R passes, equivalent to a true strain ϵ of about -32, most of the crystalline signal contributions vanished and a broad diffuse scattering maximum appeared. Further processing for up to 80 F&R passes ($\epsilon = -64$) leads to the complete disappearance of Bragg peaks. The signal only shows a broad maximum at 42.6° that is usually interpreted as being typical of an amorphous phase.

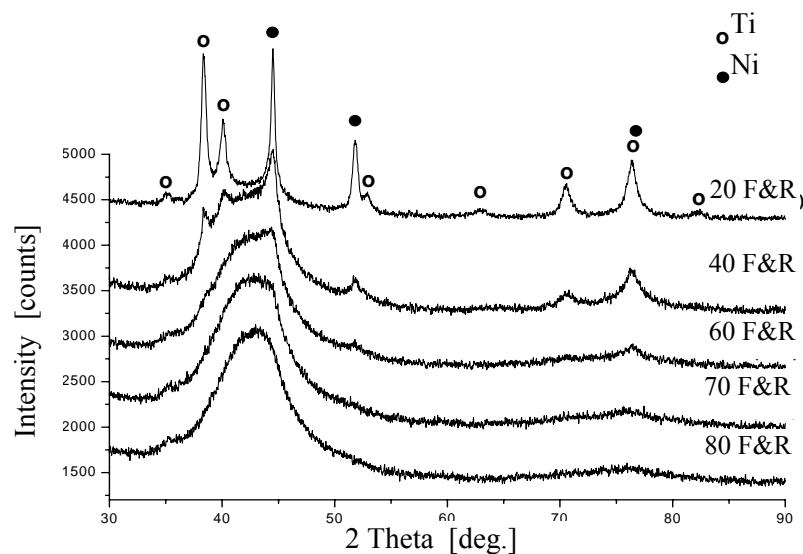


Figure 4.22: XRD scan of the as-rolled multilayer samples (Ni₅₀Ti₅₀) after different F&R cycles as indicated in the figure.

However, high-resolution TEM investigations revealed no amorphous phase, but the presence of a dense, nanocrystalline structure. Fig. 4.23 shows a typical high resolution TEM image of a Ni₅₀Ti₅₀ sample that has been rolled for 80 F&R passes. Remarkably, clear lattice fringes are observed that indicate a densely packed microstructure consisting of individual nanocrystals with an extremely low average diameter of about 4-5 nm. In addition to the small average grain size, cold-rolling of the

stacked elemental foils resulted in a comparably narrow size distribution: grains larger than 6 nm in diameter have not been observed in any sample which has been rolled for 80 F&R passes. However, the analysis of the lattice constant from the fringes that are observable in the individual grains as well as SAED analysis indicate that the grains are essentially consisting of the pure components, i.e. the lattice constants indicate either a Ni or a Ti-lattice.

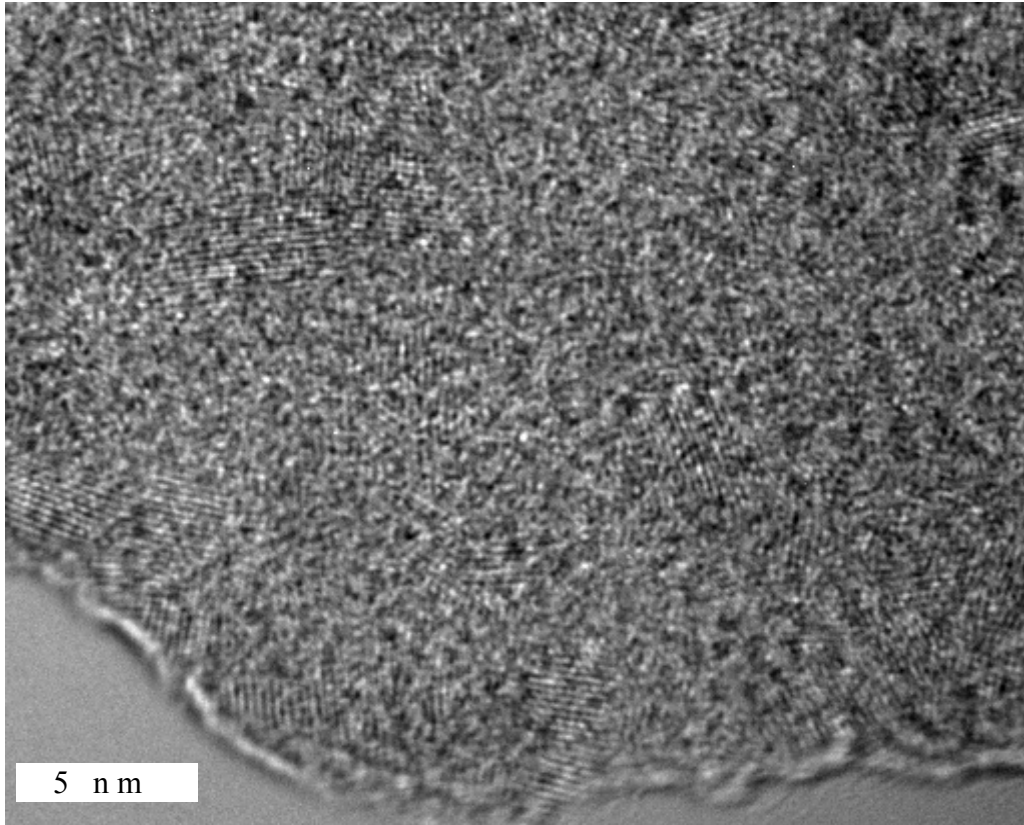


Figure 4.23: HR-TEM micrograph of a Ni₅₀Ti₅₀ multilayer sample that has been rolled for 80 passes.

4.3.2 Grain refinement of Ni₅₀Ti₅₀ shape memory alloys

Similar results have been observed after very little deformation in the sample with the same nominal composition (Ni₅₀Ti₅₀) but starting from a prealloyed sample. XRD patterns obtained from the samples with various thickness reductions are shown in Fig. 4.24. All observed peaks can be identified to represent either the intermetallic phase NiTi in the austenitic B2 (bcc, typical structure of CsCl) structure or NiTi₂ respectively. The appearance of a strong (110)_{B2} peak and the absence of the (200)_{B2} peak after the deformation corresponding to a true strain of -0.3 are due to the development of a strong rolling texture. Initially the intensity of the Bragg peaks of the intermetallic compounds gradually reduced and broadened with an increasing number of rolling passes which is common in plastic deformation processes. After a true strain of -1.2, most of the crystalline signal contribution vanished and a broad diffuse scattering maximum appeared.

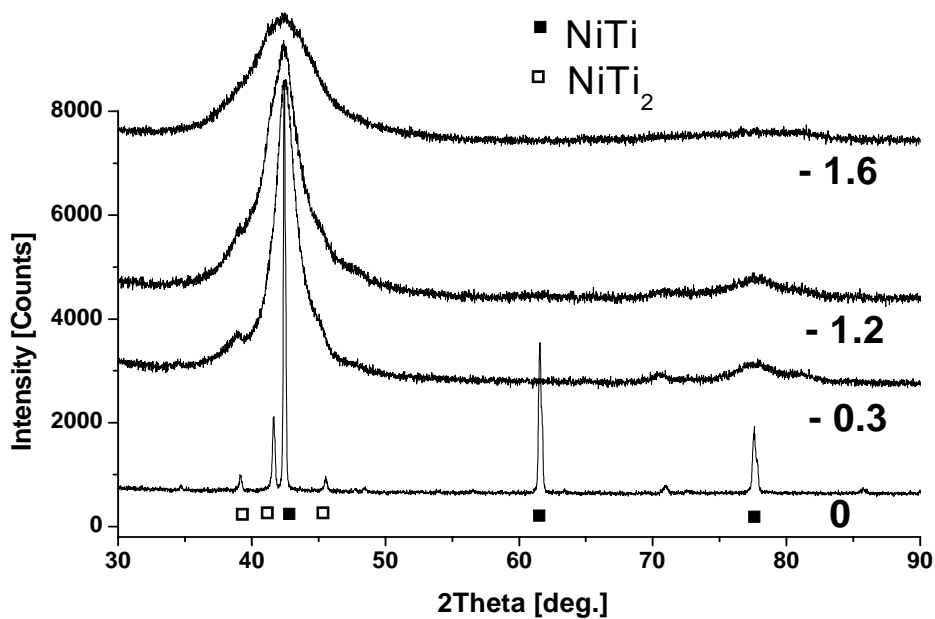


Figure 4.24: XRD signal after cold-rolling the prealloyed sample.

Upon further cold rolling to a true strain of -1.6, only the typical broad maximum is visible at 42.4° and no crystalline peak was observed, which indicates the presence of an amorphous phase. However, corresponding high resolution TEM investigations revealed the presence of a dense nanocrystalline structure also for the prealloyed sample and after a surprisingly low strain input. Fig. 4.25 shows typical high resolution TEM images (lattice fringes are clearly observable) of a Ni₅₀Ti₅₀ sample after a true strain of -1.6, indicating a dense nanocrystalline structure. After a true strain of -1.6, the typical microstructure consists of nanocrystalline grains with an average diameter of 5-6 nm.

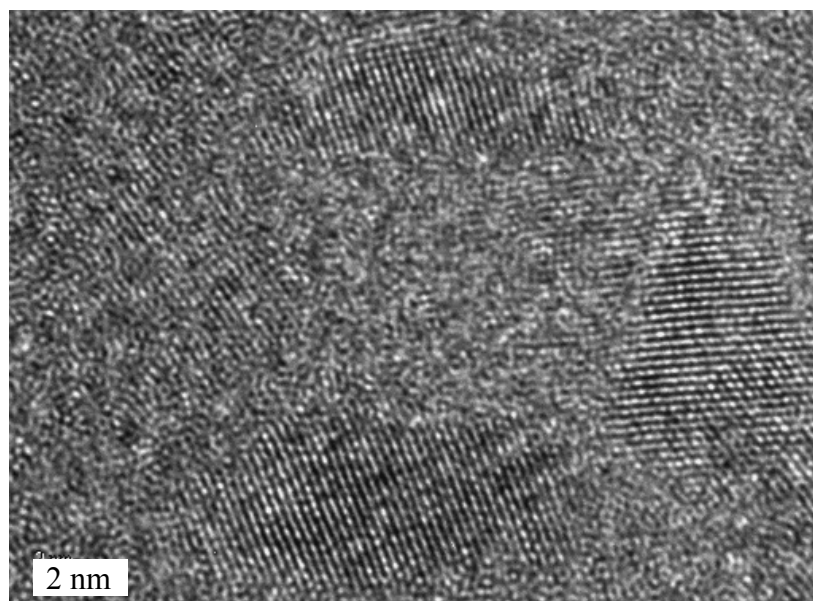


Figure 4.25: HR-TEM micrograph at the maximum strain level of the pre-alloyed sample.

4.3.3 Discussion

The present results demonstrate that bulk nanocrystalline Ni₅₀Ti₅₀ samples with average grain sizes considerably smaller than 10 nm can be synthesized at ambient temperature using two different processing pathways that start from a layered array of individual elemental sheets and alternatively, starting from the prealloyed intermetallic compounds. TEM measurements have indicated that the evolution of nanocrystalline structures yields quite similar final grain sizes starting from two different initial states. After heavy deformation equivalent to a true strain of about -64 when rolling started from pure elemental multilayers and a true strain of about only -1.6 when starting from prealloyed material, results a dense nanocrystalline structure with an average grain size of about 4-5 nm. In other words, very high deformation levels are required when rolling started from the pure elemental foils, whereas starting from a relatively brittle prealloyed sample, only little deformation is sufficient to produce a similar microstructure. This result is related to the defect generation rate and equilibrium defect density that is quite higher in brittle material, which essentially leads to finer microstructures rather quickly compared to relatively ductile materials.

4.4 Interface reaction between Al and Ni

Solid state diffusion and diffusion controlled reactions are important phenomena in many areas of technology, especially in the case of multilayered structures used in microelectronics devices. It is well known that in thin film configurations, certain crystalline or amorphous phases may grow rather than other thermodynamically more stable phases. This early result motivated us to analyze the phase-formation sequence, including the absence of certain equilibrium phases and the formation of metastable phases at the early stages of interface reactions. In this context, the Al–Ni system offers a model system to study the interface reaction, because the system is extensively studied [Sieber et al. 2001 and references therein] since it is relevant for both metallization and high temperature applications including coatings, such as laminates, and intermetallic matrix composites.

Elemental foils of Al (99.997%) and Ni (99.99%) with a thickness between 100 and 25 μm were stacked to form arrays of composition Al₈₀Ni₂₀ and folded 3 times to yield a 20x20 mm² multilayer sandwich. The folded samples were then rolled in a motorized 2-high rolling mill at a strain rate of 0.5 s⁻¹ up to 70 F&R passes as described in section 3.1. The microstructural evolution and interface reaction has been studied by XRD, TEM and three-dimensional atom probe (3D-AP) analysis at different stages of rolling and after additional annealing.

Fig. 4.26 shows the XRD scans of (a) an as-rolled Al₈₀ Ni₂₀ multilayer sample that has been rolled for 50 F&R passes and (b) after an additional annealing treatment at 250⁰C for 2 minutes. The XRD pattern of as rolled sample show only pure elemental peaks of Al and Ni. No reaction occurred between Al and Ni during severe cold-rolling. Some broadening of the reflections is observed for the highest number of F&R passes due to the grain refinement. On the other hand, all observed peaks of the short-time annealed sample can be identified to represent either the pure elements or the Al₃Ni intermetallic phase.

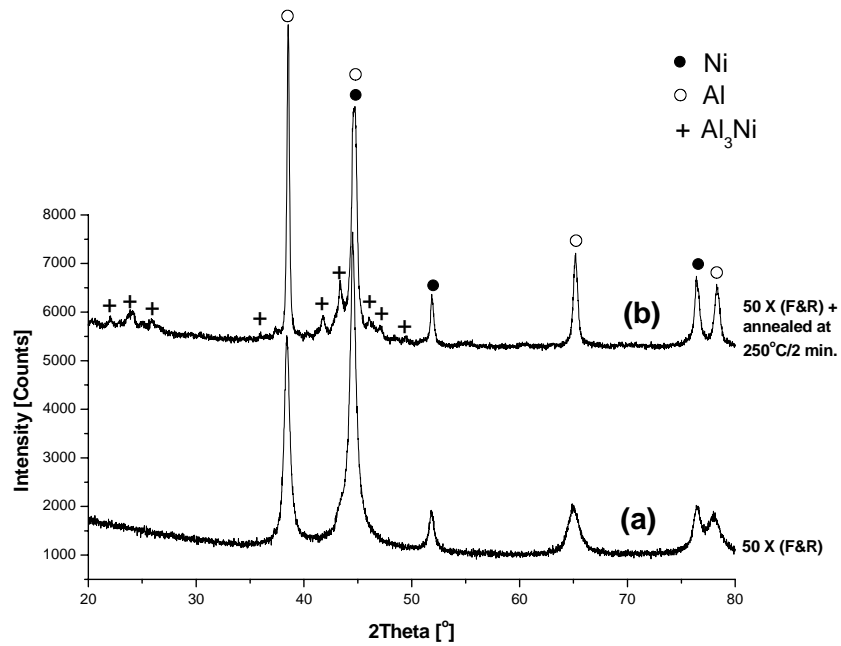


Figure 4.26: XRD patterns of an $\text{Al}_{80}\text{Ni}_{20}$ composite subjected to (a) 50 F&R passes and (b) the cold-rolled sample was annealed at 250°C for 2 min.

Fig 4.27 shows the cross-sectional energy filtered TEM micrographs of (a) an as-rolled (50 F&R) and (b) an annealed (2 min. at 250°C) sample. It can be seen from Fig. 4.27 that a multilayer structure is developed during repeated cold-rolling. The average layer thickness of Ni is about 10 nm after 50 F&R passes. The cross-sectional micrograph of the annealed sample (Fig. 4.27b) shows that limited interdiffusion took place at the Al/Ni interface (fade green area of Fig. 4.27b) due to the short annealing. However, some residual pure Al (green) and Ni (pink) layer can be identified after

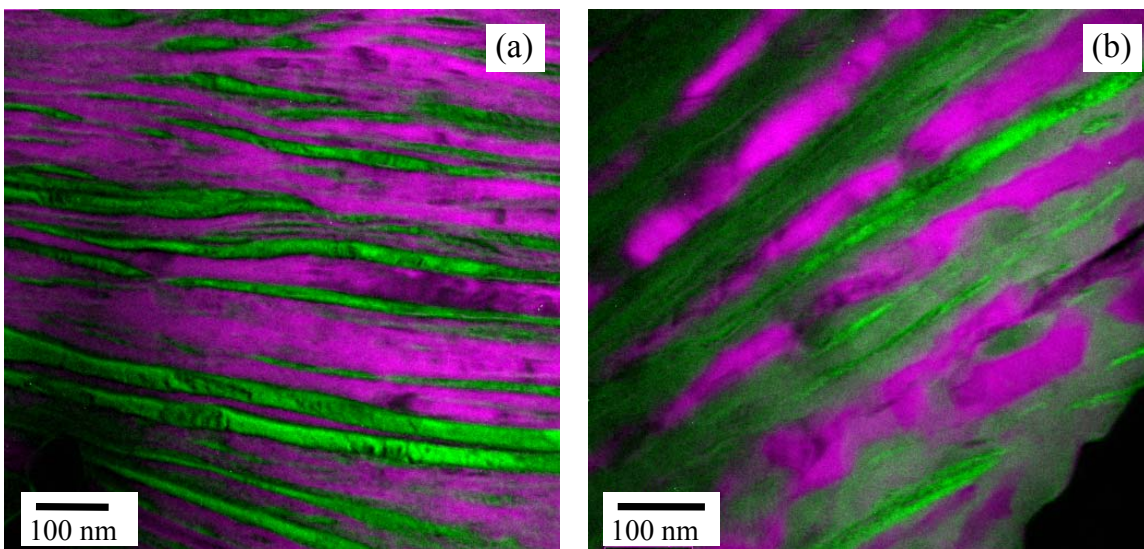


Figure 4.27: Energy-filtered TEM micrographs of (a) $\text{Al}_{80}\text{Ni}_{20}$ that has been rolled for 50 F&R passes and (b) after an additional annealing at 250°C for 2 minutes. The individual Al (pink) and Ni (Green) layer are visible.

controlled annealing. Comparing the TEM micrograph (Fig. 4.27b) with the corresponding XRD scan (Fig. 4.26), it is clear that an interface reaction took place during short-time annealing and the reacted layer (fade green area of Fig. 4.27b) consists of the Al_3Ni intermetallic phase.

Three-dimensional atom probe (3D-AP) investigation, were performed to further analyze the microstructural evolution at the interlayer interface [Sauage et al. 2005]. The 3D-AP analysis were performed in collaboration with X. Sauvage, Institute of Material Research, Universite' de Rouen, France. The most widely used atom probe is a time-of-flight atom probe. By applying high voltage pulses to a field ion microscope specimen, atoms are ionized from the surface of the tip. The field evaporated atoms which go through a small aperture called probe hole located in the centre of a field ion microscope screen are detected one-by-one using a microchannel plate detector. The position sensitive atom probe invented by Cerezo et al. [1988] about a decade ago adopted a position sensitive detector in a time-of-flight atom probe, by which they succeeded in obtaining two-dimensional elemental maps with a near-atomic resolution for all alloying elements. They also demonstrated that the elemental mapping obtained by the position sensitive atom probe can be extended to three-dimensional mapping by assigning z -coordinates in proportion to the number of detected atoms and reconstructing the data on a graphic workstation. This was the first real three-dimensional atom probe (3D-AP). The details of different atom probe techniques can be found in the review article by Hono (2002).

In the present study, 3D-AP specimens were prepared by a standard electropolishing procedure: the sample was sharpened in a solution of 2 vol. % perchloric acid in 2-butoxyethanol, cooled to 20°C , at 10 V d.c. Field ion microscopy images were obtain at 80 K using Ne as imaging gas (pressure of 5×10^{-3} Pa). 3D-AP analysis were carried out at 80 K in UHV (ultra high vacuum; residual pressure 10^{-8} Pa) with 16% pulse fraction and 1.7 kHz pulse repetition rate. The position sensitive detector used was a CAMECA's tomographic atom probe detector developed in the GPM (University of Rouen).

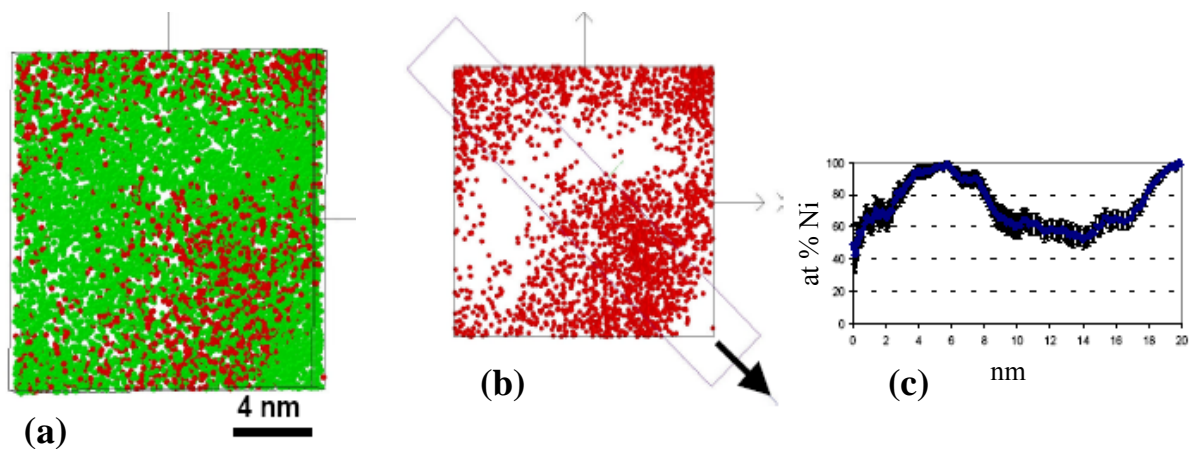


Figure 4.28: 3D-AP data set of as-rolled $\text{Al}_{80}\text{Ni}_{20}$ composite after 50 F&R passes: (a) elemental map of Al (red) and Ni (green), (b) only Al atoms are displayed to exhibit Al/Ni interface and (c) Ni concentration profile across the Al/Ni interface.

Fig. 4.28 shows the 3D-AP elemental mapping of Al (red) and Ni (green) in a selected volume of an as-rolled $\text{Al}_{80}\text{Ni}_{20}$ (50 F&R) sample. In figure 4.28b, only Al atoms are plotted to exhibit the Al/Ni interface. The rectangular area of Fig. 4.28b shows the region in which atoms are counted along the direction marked by the arrow to draw the concentration profile at the interface. Direct atom probe measurements show that considerable interdiffusion of atoms took place at the Al/Ni interface during repeated cold-rolling at room temperature. It can be seen from Fig. 4.28c that a supersaturated solid solution (about 40 % Ni atoms in the Al matrix) layer up to 6 nm in thickness present between Al and Ni layers. However, from TEM and XRD results, it should be noted that no intermetallic phase was noticed at the interface of the severely deformed as-rolled sample.

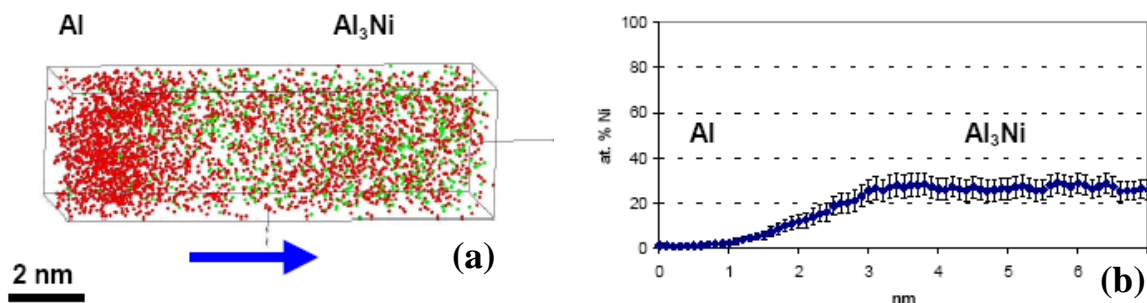


Figure 4.29: (a) 3D-AP elemental map of Al (red) and Ni (green) of $\text{Al}_{80}\text{Ni}_{20}$ composite that has been rolled for 50 F&R passes and annealed at 250°C for 2 minutes, (b) Ni concentration profile across Al/Ni interface.

On the other hand, the 3D-AP analysis (Fig. 4.29) shows that the Al_3Ni phase was formed at the Al/Ni interface of the annealed (2 min. at 250°C) sample. The composition analysis (Fig. 4.29b) shows that at least 4 nm thick layer of the Al_3Ni phase are present between unreacted Al and Ni layers. Fig. 4.30 shows another 3D-AP composition profile of the same annealed sample. It can be seen that at one Al/Ni interface (on the right side of the Al layer of Fig. 4.30a), no phase was formed even after annealing. In contrast, the Al_3Ni intermetallic phase was nucleated on the opposite side of the Al layer. The concentration gradient is $1.25 \times 10^6 \text{ cm}^{-1}$ at the interface where the Al_3Ni phase was nucleated. However, the concentration gradient is quite high, $5 \times 10^6 \text{ cm}^{-1}$, on the opposite side where no phase was detected. This results indicates that sharp concentration gradients present at the interface restrict the formation of any phase at that interface. This phenomena can be explained by a model developed by [Desre' et al. 1990, 1991], which considers that nucleation of any crystalline phase is not possible above a critical concentration gradient by reducing or even suppressing the driving force for nucleation. However, it is surprising that after annealing, the concentration gradient is very sharp at one interface and relatively flat at the opposite interface although the thermal diffusion should takes place similarly in both the interfaces. This can be explained by Fig. 4.31. As we have seen that after extensive rolling, some alloying took place at the interface. However, during further deformation, at certain regions of the

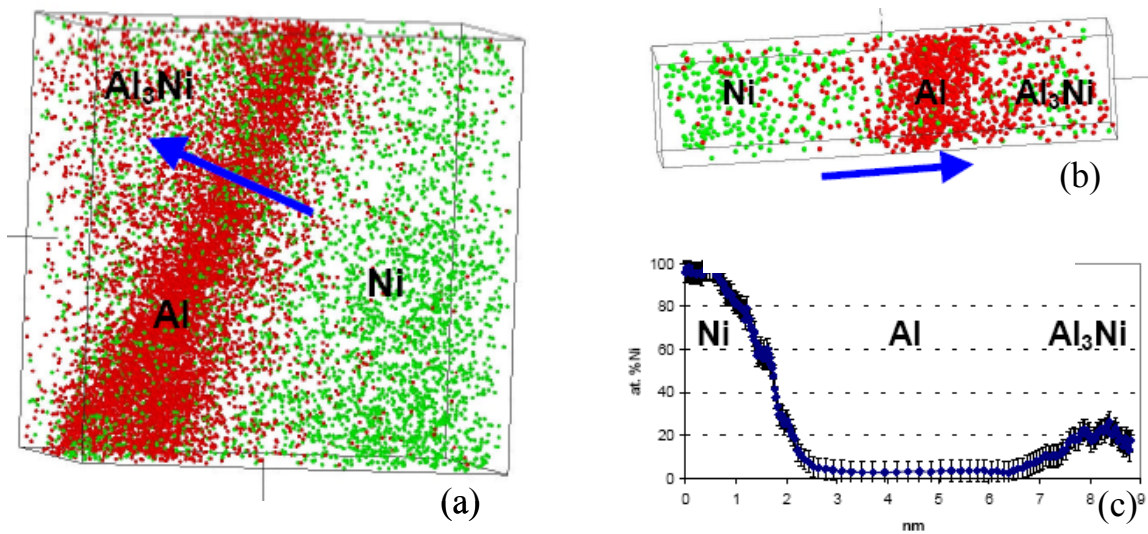


Figure 4.30: (a)–(b) 3D-AP elemental map of Al (red) and Ni (green) of 50-(F&R) $\text{Al}_{80}\text{Ni}_{20}$ composite annealed at 250°C for 2 minutes, (c) Ni concentration profile across Al/Ni interface.

sample pure metals can come closer by replacing the alloyed layer at the interface due to the inhomogeneous deformation as schematically shown in Fig. 4.31b. As a result, the concentration gradient is very sharp at the position where almost no solid solution layer is present at the Al/Ni interface, whereas the concentration gradient is relatively flat at the other interface due to the presence of an alloyed layer at the interface. Consequently, after controlled annealing, due to the diffusion at both the interfaces the extremely sharp gradient becomes somewhat flatter but not sufficiently low to form any crystalline phase at that interface. On the other hand, the concentration gradient at the initially alloyed interface becomes low enough to form certain phase at the interface. The effect of the concentration gradient on nucleation kinetics is described in detail in the next chapter of the thesis.

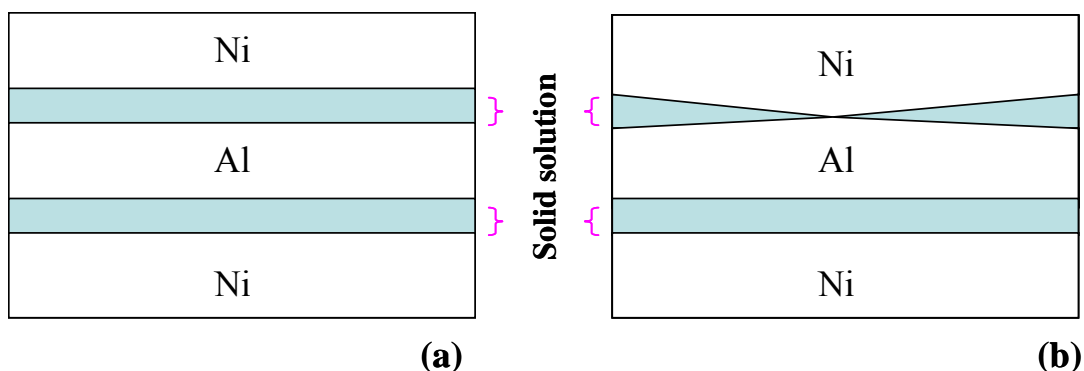


Figure 4.31: Schematic representation of multilayer structure developed during repeated cold-rolling. (a) a thin uniform layer of supersaturated solid solution present between Al and Ni, (b) non uniform alloyed layer between pure metals.

Chapter 5

Amorphous materials from repeated cold-rolling

Since the early discovery of Schwartz and Johnson (1983), amorphization by solid-state reactions have been observed in many binary and multicomponent systems in both deposited multilayers and by mechanical alloying processes. The two main mechanical alloying processes that can induce a crystalline-to-amorphous transition are milling of powders or repeated cold rolling processes. Although mechanical alloying processes have been extensively investigated, the mechanism of solid-state amorphization reaction during the mechanical deformation process is not yet firmly established. Moreover, compared to ball milling, the repeated cold rolling process has been much less systematically studied and especially the early stages of amorphization during mechanical alloying still call for more detailed investigations.

For a better understanding of the progress of solid state reaction, we used repeated cold rolling because the geometry of the elemental layers is better defined compared to ball milled samples and since the deformation can be performed at a low strain rate to avoid the uncertainty of increasing the temperature during processing which is commonly observed during ball milling. Therefore, we performed detailed structural investigations of the solid-state amorphization reaction during repeated cold rolling in different binary $\text{Cu}_{60}\text{Zr}_{40}$, $\text{Ni}_{36}\text{Zr}_{64}$, ternary $\text{Ti}_{35}\text{Zr}_{10}\text{Cu}_{55}$ and quaternary $\text{Zr}_{65}\text{Al}_{7.5}\text{Cu}_{17.5}\text{Ni}_{10}$ and $\text{Ti}_{35}\text{Zr}_{10}\text{Cu}_{47}\text{Ni}_8$ elemental multilayers. However, the early stages of the amorphization reaction has been studied systematically in the $\text{Cu}_{60}\text{Zr}_{40}$ system by plan view as well as cross-sectional transmission electron microscopy. In the prior work, amorphous samples produced by cold rolling were reported mainly based on plan view TEM, which due to the projected view is problematic in terms of studying the process at the internal heterophase interfaces.

5.1 Binary Cu-Zr elemental multilayer

In this section we describe the progress of the solid-state amorphization reaction in the $\text{Cu}_{60}\text{Zr}_{40}$ alloy at different stages of deformation. Elemental foils of Cu and Zr (purity $\geq 99.98\%$) with a thickness between 16 and 25 μm were stacked to form arrays of compositions $\text{Cu}_{60}\text{Zr}_{40}$ and then were continuously cold-rolled up to 100 F&R passes. The evolution of the amorphous phase investigated by x-ray diffraction (XRD) is shown in Fig. 5.1. In the early stages of rolling, the intensity of the elemental Bragg peaks gradually reduced and broadened with an increasing number of rolling passes due to continuous grain refinement by plastic deformation. After 40 F&R passes, a broad diffuse maximum, characteristic of an amorphous phase and centred at about $2\theta = 39.8^\circ$ appeared along with some weak crystalline diffraction peaks due to unreacted Cu and Zr. Doubling the F&R passes leads to a fully amorphous sample without any indication for residual crystalline material. Further rolling up to 100 passes makes no significant changes in the diffraction pattern, indicating that the amorphization process was completed after 80 passes. There is no indication for the formation of an intermetallic compound at any stage of cold rolling.

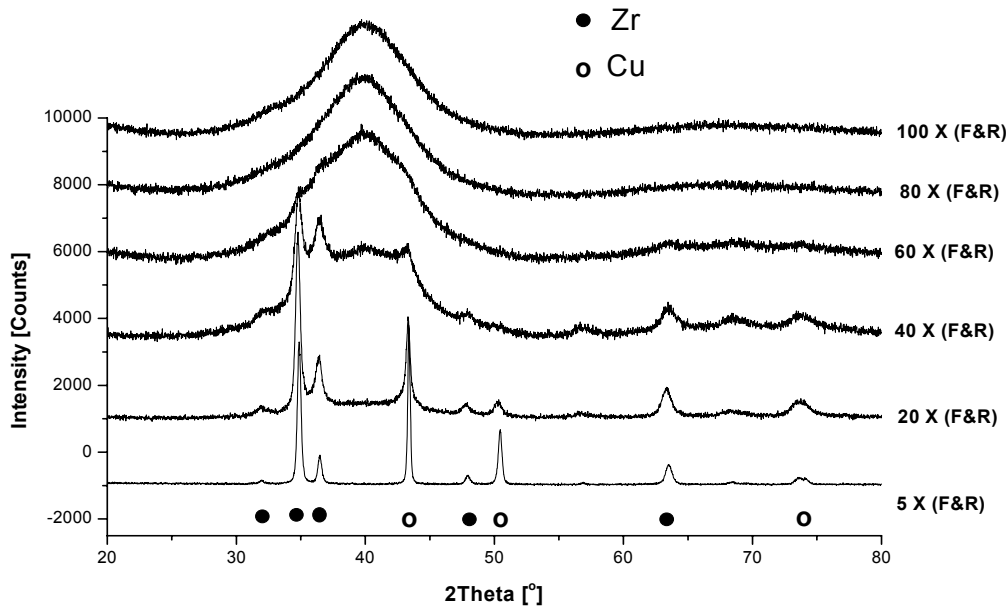


Figure 5.1: XRD scan of as-rolled $\text{Cu}_{60}\text{Zr}_{40}$ multilayer samples after different F&R cycles as indicated in the figure.

The average elemental layer thickness, grain size and amorphous layer thickness estimated from the scanning transmission electron microscopy (STEM), dark-field TEM and high resolution TEM micrographs is shown in Fig. 5.2. In the early stage, cold rolling leads to a fast decrease of the layer thickness down to 20 nm. Further refinement occurs slowly to about 8 nm after severe deformation. The average layer thickness is about 1 μm after 10 F&R cycles and 15 nm after 20 F&R cycles. Further processing up to 40 F&R cycles results in a refinement of the individual layers thickness that varies

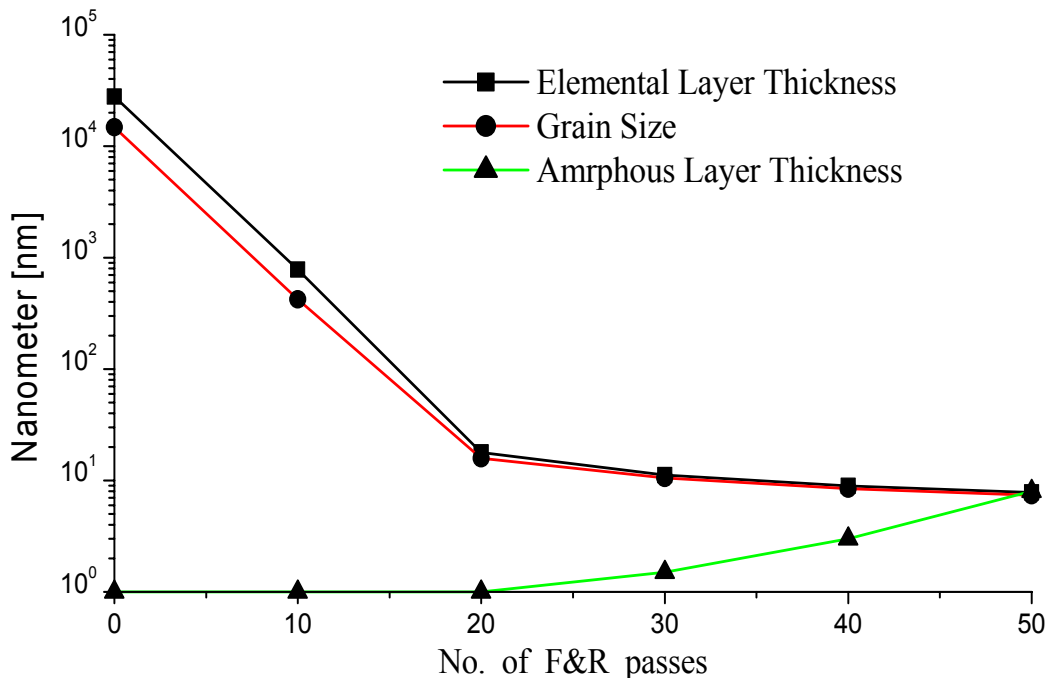


Figure 5.2: Change in elemental layer thickness (■), grain size (●) and amorphous layer thickness (▲) as a function of the F&R cycles.

from 7 to 10 nm (Fig. 5.3). No layer structure was observed after 50 F&R cycles because the sample was transformed almost completely to the amorphous state. Layer thicknesses smaller than 5 nm have not been observed at any stage of the deformation. This can be explained by recent molecular dynamic simulations (see section 2.2.5) which indicate that below a critical grain size (about 5-10 nm) the nucleation of dislocation from the grain boundary is not possible. Therefore, dislocation mechanisms cease to function when the grain sizes or layer thickness are below a critical value. Therefore further deformation occurs by a grain boundary slide mechanism that does not refine the microstructure any more.

Recently, Lund et al. (2003, 2004) have reported by atomistic simulations of the Cu-Zr system that an amorphization reaction occurs when all elemental layers were refined to the length scale of single atoms. Additionally, it is also proposed [Lund et al. 2003, 2004] that during repeated rolling, the individual layers break down due to multiple necking. As a result, no well-aligned layered structure is visible over a large distance. The multiple necking (necking is defined as a local reduction of the layer thickness along the direction of maximum shear) phenomena was first observed by Bordeaux and Yavari (1990) in Pt-Al, Pd-Al, Zr-Al and Ti-Al cold-rolled multilayers. However, in the present study a continuous decrease of the layer thickness to an atomic scale is not observed even after severe deformation. Furthermore, multiple necking is not observed at any stage of the deformation. Rather large differences of the shear modulus values of the constituents are required for necking to occur, which is not the case for the Cu-Zr system (Shear modulus of Cu is 42 GPa and of Zr is 33 GPa). Consequently, a rather homogeneous decrease of the layer thickness was observed in this work.

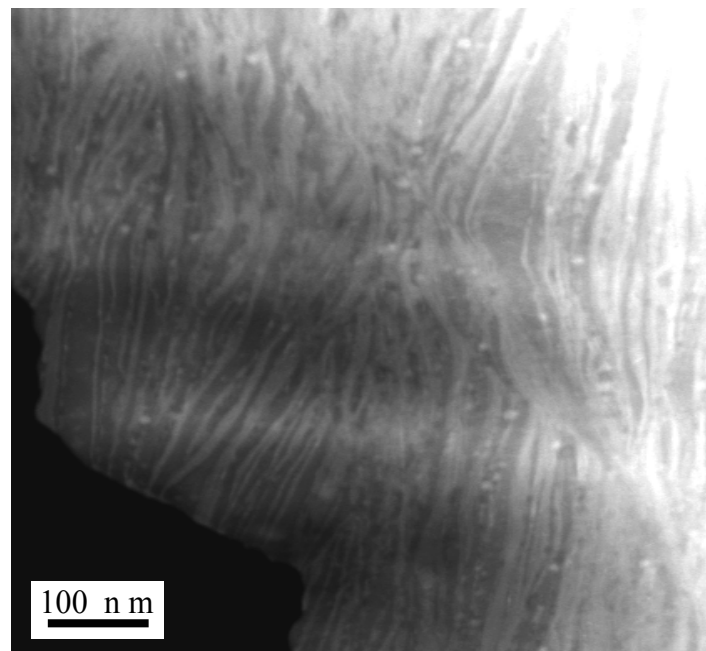


Figure 5.3. STEM micrograph of $\text{Cu}_{60}\text{Zr}_{40}$ composite after 40 F&R passes. The bright lines correspond to Cu layers.

Cross-sectional and plan view TEM investigations have been performed in order to obtain detailed information about the amorphization process at different stages of deformation. Fig.5.4 shows a high resolution cross-sectional TEM image of a $\text{Cu}_{60}\text{Zr}_{40}$ sample that has been rolled for 40 or 50 F&R passes respectively, showing two different areas– one defined with clear lattice fringes, indicating a crystalline structure, and the other without lattice fringes, indicating an amorphous (α) structure. In high resolution TEM, some times clear lattice fringes can not be observed due to the overlapping of two or more crystals under the electron beam. However, figure 5.4 shows that the width of the crystalline and the featureless regions that are aligned in parallel are almost equal. Such a microstructural feature can not be generated by overlapping of crystals. Therefore, it is clear that the region without lattice fringes is constituting an amorphous phase. Additionally, the accompanying selected area electron diffraction (SAED) pictures (inserts in Fig. 5.4) show a diffuse diffraction contrast along with a ring-like intensity distribution that indicates the presence of both amorphous and nanocrystalline phases. From TEM investigations it was confirmed that the rolling procedure first yields an ultrafine layered composite, with an individual layer thickness of about 15 nm after 20 F&R passes before the amorphization reaction starts. After 20 F&R passes, a thin layer of amorphous phase starts to form at the interlayer interface between the approximately 10 nm thick elemental Cu and Zr layers and then continuously grows up to 8 nm after 50 F&R cycles. Further deformation transforms the entire sample to an amorphous phase. It should be noted that a very similar microstructural development (layer-thickness decrease, grain size decrease and amount of amorphous phase present at different stages of deformation) has been observed in $\text{Cu}_{75}\text{Ti}_{25}$ and $\text{Ni}_{36}\text{Zr}_{64}$ multilayer samples. An elemental $\text{Cu}_{75}\text{Ti}_{25}$ sample has been transformed completely to the amorphous phase after 130 F&R passes, whereas $\text{Ni}_{36}\text{Zr}_{64}$ takes 120 F&R cycles to transform completely to the amorphous state.

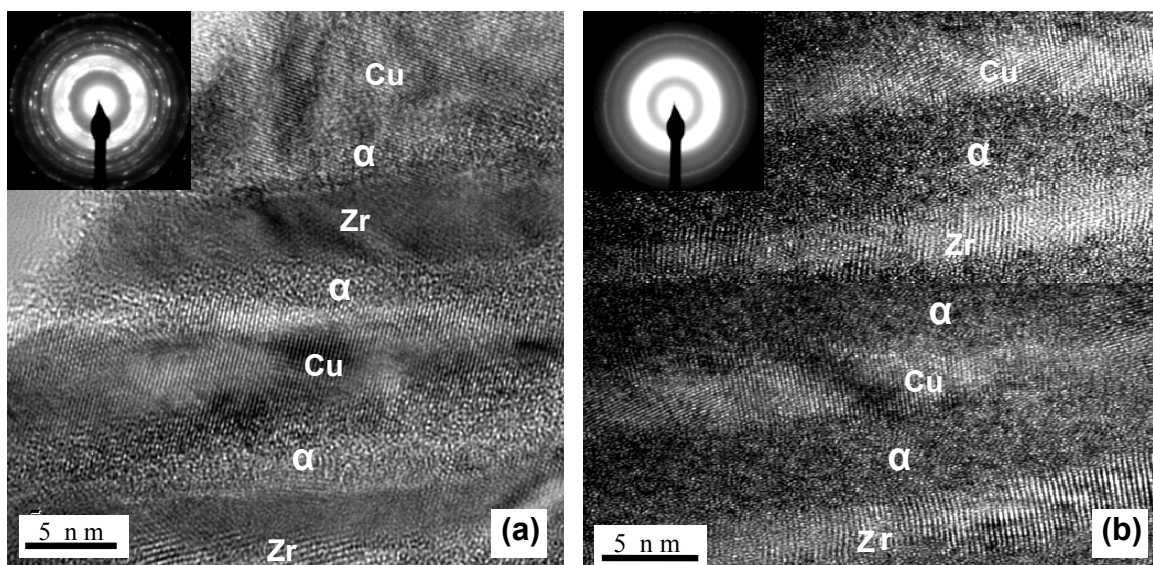


Figure 5.4: High resolution cross-sectional TEM image of $\text{Cu}_{60}\text{Zr}_{40}$ sample after (a) 40 and (b) 50 F&R passes.

5.2 Amorphous phase forming abilities of Binary, Ternary and Quaternary systems

To study the potential of amorphous phase formation of different multicomponent alloy systems and to compare their glass forming abilities, binary $\text{Ni}_{36}\text{Zr}_{64}$, ternary $\text{Ti}_{35}\text{Zr}_{10}\text{Cu}_{55}$ and quaternary $\text{Ti}_{35}\text{Zr}_{10}\text{Cu}_{47}\text{Ni}_8$ samples have been deformed by cold-rolled starting from elemental multilayers. The development of the amorphous phase investigated by X-ray diffraction of the three systems are shown in Fig. 5.5. The processes of solid state reaction for all the systems are apparently similar at the initial stages of cold rolling. Initially both the layer thickness and grain size were reduced to about 20 nm before the amorphization reaction starts at the interface. There is no significant shift in the position of the Bragg peaks as a function of F&R passes, indicating the limited solubility of the constituent phases. After 50 F&R passes for $\text{Ni}_{36}\text{Zr}_{64}$, 40 F&R passes for $\text{Ti}_{35}\text{Zr}_{10}\text{Cu}_{55}$, and 30 F&R passes for $\text{Ti}_{35}\text{Zr}_{10}\text{Cu}_{47}\text{Ni}_8$ a broad diffuse maximum, characteristic of an amorphous phase and centered at about $2\theta = 36.5^\circ$, 41.5° and 41.25° appeared respectively along with some weak diffraction peaks due to residual pure elements. It is seen that each system requires different amounts of deformation to achieve the amorphous state. The quaternary $\text{Ti}_{35}\text{Zr}_{10}\text{Cu}_{47}\text{Ni}_8$ system displays the best glass forming ability and takes only 50 F&R passes to transform almost completely to the amorphous state. Whereas $\text{Ti}_{35}\text{Zr}_{10}\text{Cu}_{55}$ and $\text{Ni}_{36}\text{Zr}_{64}$ systems require 70 and 120 F&R passes respectively for amorphization to occur in a

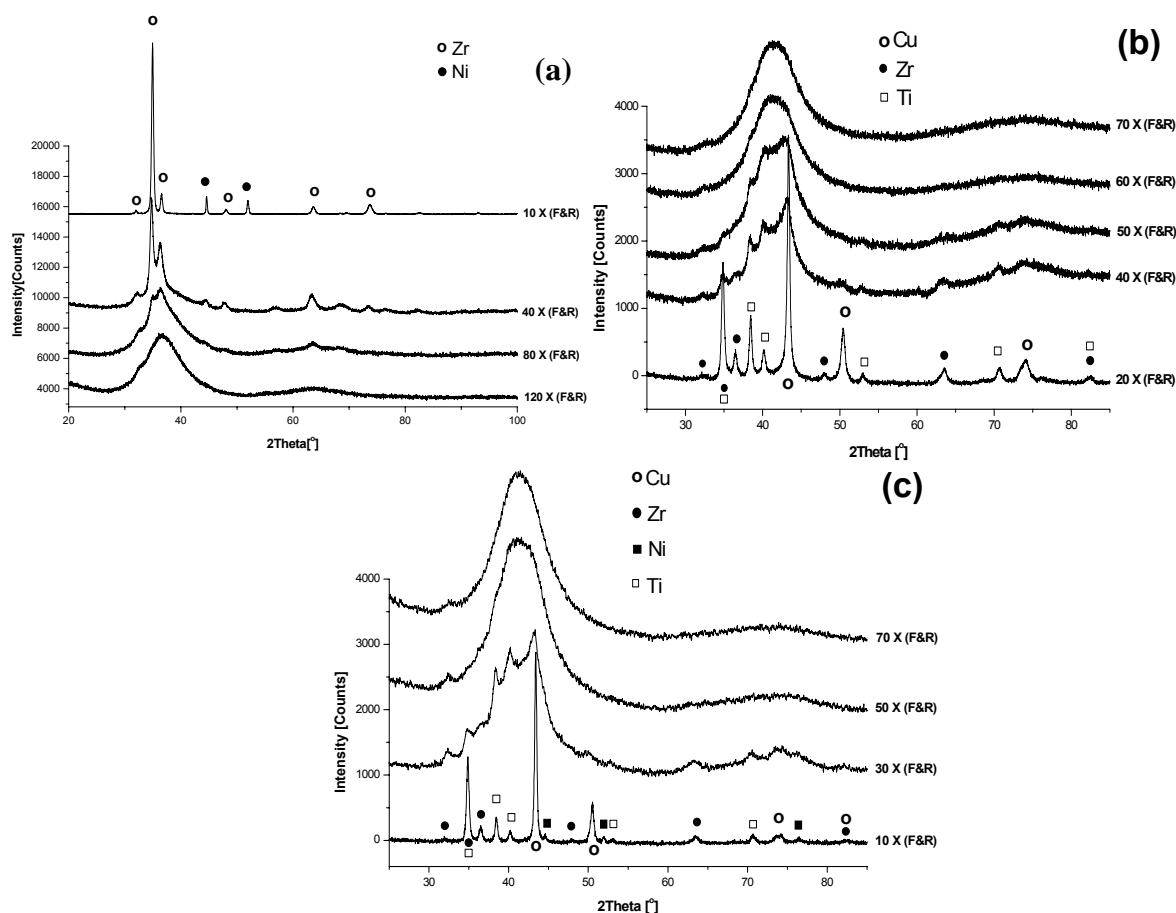


Figure 5.5: XRD scan of three different multilayer samples after different F&R cycles as indicated in the figure: (a) $\text{Ni}_{36}\text{Zr}_{64}$, (b) $\text{Ti}_{35}\text{Zr}_{10}\text{Cu}_{55}$ and (c) $\text{Ti}_{35}\text{Zr}_{10}\text{Cu}_{47}\text{Ni}_8$.

considerable fraction of the sample. The presence of a very small peak at around 32.4° in all the heavily cold-rolled materials indicates the presence of a small amount of α -Zr in the amorphous matrix. There is no indication for the formation of an intermetallic compound at any stages of cold rolling.

From TEM investigations, it was found that, even after very large deformation, some small residual crystallites are present in the amorphous matrix. The high resolution plan view TEM images (Fig. 5.6) of $\text{Ni}_{36}\text{Zr}_{64}$, $\text{Ti}_{35}\text{Zr}_{10}\text{Cu}_{55}$ and $\text{Ti}_{35}\text{Zr}_{10}\text{Cu}_{47}\text{Ni}_8$ samples after 120, 70 and 70 respective F&R passes show that a small fraction of residual crystals ('Cr') with an average grain size of about 4-5 nm are present in the amorphous (α) matrix in all cold rolled samples. Additionally, the accompanying SAED picture (insert in Fig. 5.6) shows a diffuse diffraction contrast along with a ring-like intensity distribution that indicates the presence of nanocrystallites in the amorphous matrix. From lattice fringes calculation, it was confirmed that the remaining crystallites are consisting of unreacted solid solution of pure elements (mostly Zr), but not any intermetallic compounds. It has been observed that the quaternary system shows the best glass forming ability in the solid state.

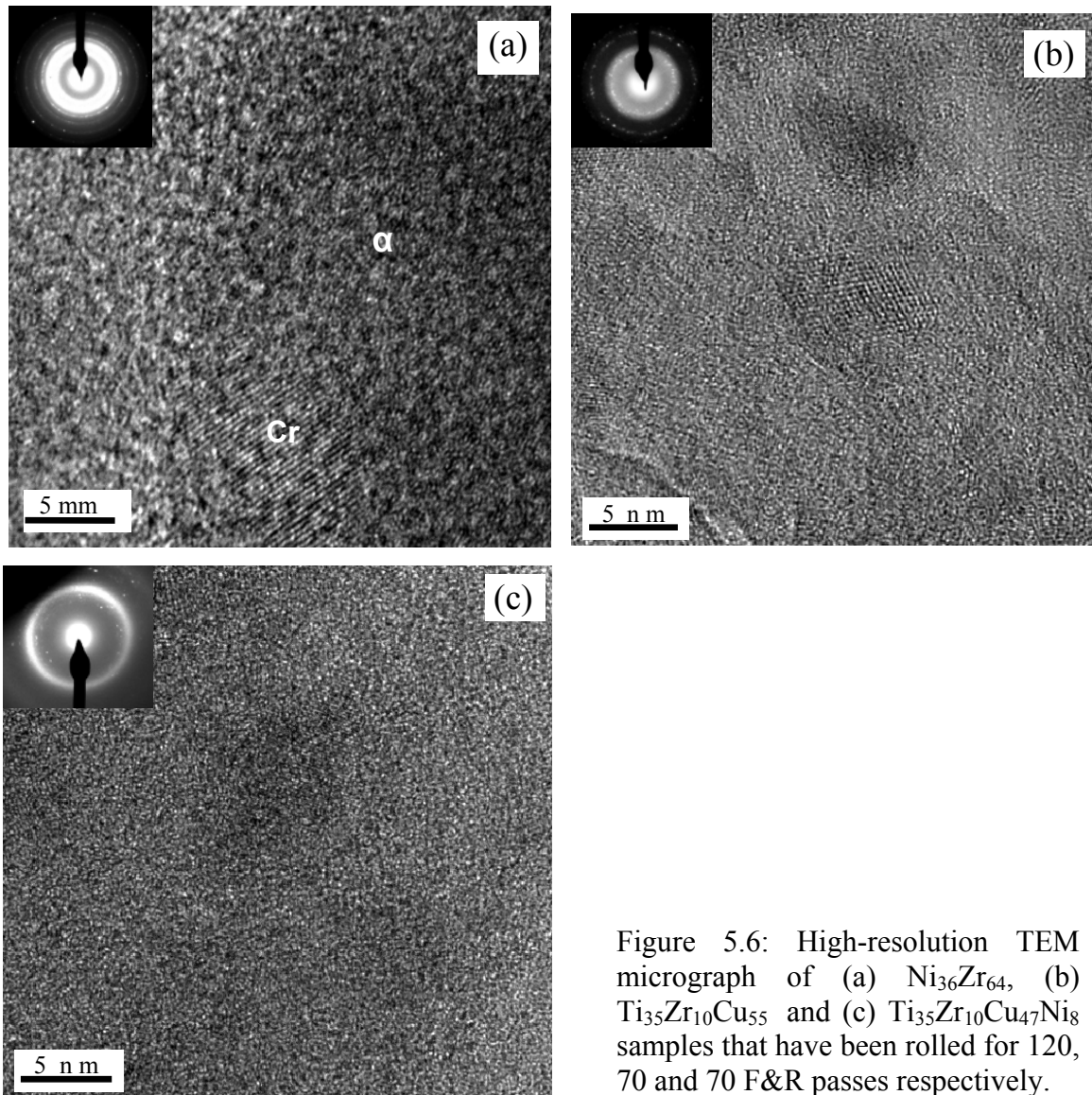


Figure 5.6: High-resolution TEM micrograph of (a) $\text{Ni}_{36}\text{Zr}_{64}$, (b) $\text{Ti}_{35}\text{Zr}_{10}\text{Cu}_{55}$ and (c) $\text{Ti}_{35}\text{Zr}_{10}\text{Cu}_{47}\text{Ni}_8$ samples that have been rolled for 120, 70 and 70 F&R passes respectively.

5.3 Progress of solid state amorphization reaction by repeated cold-rolling

The present results demonstrate that all binary $\text{Cu}_{60}\text{Zr}_{40}$, $\text{Ni}_{36}\text{Zr}_{64}$, ternary $\text{Ti}_{35}\text{Zr}_{10}\text{Cu}_{55}$ and quaternary $\text{Ti}_{35}\text{Zr}_{10}\text{Cu}_{47}\text{Ni}_8$ alloy systems studied were amorphized by repeated cold-rolling from elemental foils at ambient temperature. The same cold rolling technique (i.e. repeated F&R) has been used by [Atzmon et al. 1985] and [Bordeaux et al. 1990] to examine amorphous phase formation in (Cu-Er and Ni-Er) and Al-Pt systems, respectively. In the prior work, some annealing was needed to complete the amorphization reaction. Recently, complete amorphization by cold-rolling has been reported by [Sagel et al. 1998] for a bulk glass forming quaternary Zr-Al-Ni-Cu alloy. In the present paper, we show that almost complete amorphous phase formation by cold rolling in binary, ternary and quaternary systems could be obtained without any thermal annealing. The main key to synthesize fully amorphous phases from pure elemental foils is the application of large plastic deformation to achieve a critical amount of intermixing for amorphization to proceed.

The average elemental layer thickness, grain size and amorphous layer thickness estimated from the STEM, dark-field TEM and HREM micrographs is shown in Fig. 5.2. In the early stage, cold rolling leads to a fast decrease of the layer thickness down to 20 nm. Further refinement occurs slowly to about 8 nm after severe deformation. The average layer thickness is about 1 μm after 10 F&R cycles and 15 nm after 20 F&R cycles. Further processing up to 40 F&R cycles results in a refinement of the individual layer thickness that varies from 7 to 10 nm and a well-aligned layered microstructure is obtained as shown in Fig. 5.3. No layer structure was observed after 50 F&R cycles because the sample reaches an almost completely amorphous state. Layer thicknesses smaller than 4 nm have not been observed at any stage of the deformation.

It is commonly accepted that a solid state amorphization occurs between elements that have a strong negative heat of mixing, ΔH_{mix} , and a large asymmetry of the component interdiffusivities of the elements. In the case of Cu-Zr, Ni-Zr, Ti-Zr-Cu and Ti-Zr-Cu-Ni, both the criteria are satisfied due to the large negative ΔH_{mix} between (Zr, Ti) and (Cu, Ni) [Saunders et al. 1986] and the diffusivities of (Ni, Cu) in the Zr and Ti matrix is known to be extremely rapid [Hood et al. 1972]. Intense cold rolling generates large defects densities, especially dislocations, vacancies and large grain boundary density due to the refinement of the crystallite size, which increases the free energy and eventually adds to the destabilization of the crystalline phase. However, that excess energy is considerably lower (2-3 kJ/mole) than the heat of mixing ΔH_{mix} of pure (Cu, Ni) and (Zr, Ti) and thus seems to have only little effect on the crystal -to-amorphous transformation. The main key for the amorphization to proceed is the forced atomic intermixing to achieve high values of supersaturation. Above the limit for polymorphic transformation, T_0 , the supersaturated solid solution becomes thermodynamically unstable and transforms to an amorphous phase and consequently releases the heat of mixing ($\Delta H_{\text{mix}} \approx 16$ KJ/mole for $\text{Cu}_{60}\text{Zr}_{40}$) which is 5-8 times higher than the energy associated with crystalline defects. In the present study, we observed (by composition analysis from EDX line scan across Cu-Zr interface) that when the concentration of Cu increased above 17 at.% the supersaturated Zr transformed to the amorphous state. The thermodynamics of the transformation of a supersaturated solid solution into the amorphous state can be best understood by the so-called T_0 concept.

Fig. 5.7 shows possible T_0 curves for a eutectic phase diagram. In equilibrium the system forms two solid solutions (α and β) of limited solubilities. The T_0 curves are the loci of temperature—composition points where the free energies of the phases α_{ss} and β_{ss} are equal to the free energies of the liquid phase of the same composition. In other words, T_0 represents the melting point of a specific composition transforming into a liquid of the same composition. In effect, the figure contains two phase diagrams: the solid curves define the equilibrium phase boundaries in the presence of solute partitioning (slow cooling process), whereas the T_0 lines define the metastable boundaries when solute partitioning is suppressed (in the case of rapid cooling). In Fig. 5.7, the T_0 curves for the primary solid solutions rapidly fall with decreasing temperature and near the eutectic point do not cross each other before the intersection with the glass transition temperature, T_g . For such conditions the limit on rapid solidification to a partitionless solid will be terminated by formation of a glass at near-eutectic compositions. Therefore, the crystalline supersaturated solid solution between two T_0 curves and below T_g is not stable but transforms to a glass. However, supersaturated solid solutions can form not only by rapid solidification but also by mechanical alloying. Therefore, if we gradually increase the concentration of solute atoms in the solvent and when the concentration of the supersaturated solid solution increases above the T_0 line (maximum solubility limit), then the sample can transform to the amorphous state.

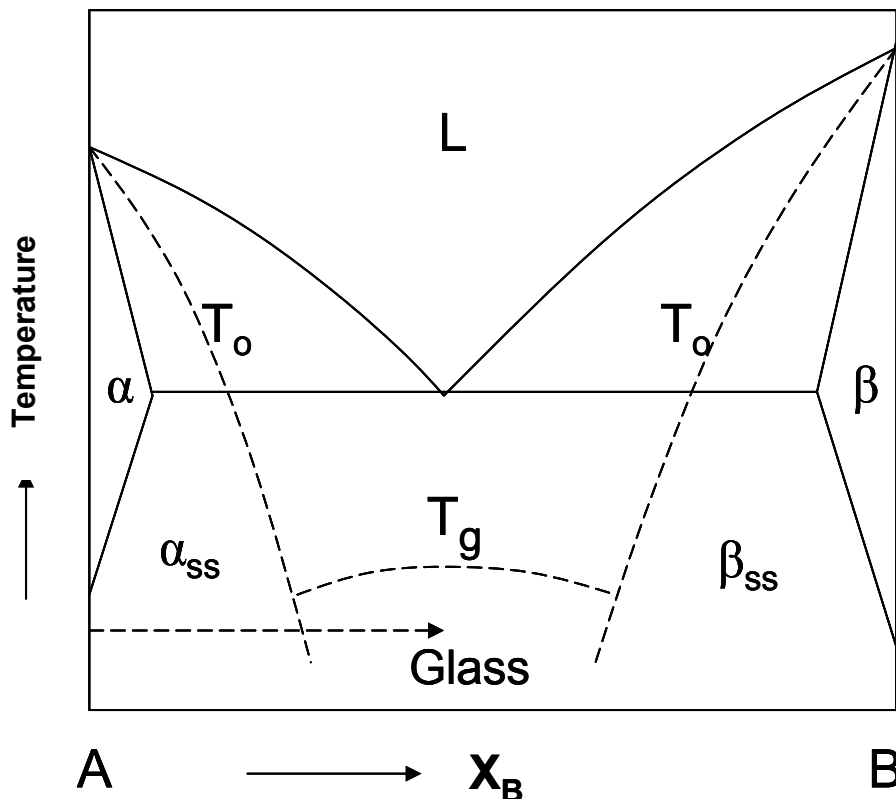


Figure 5.7: Schematic representation of T_0 curves for the liquid to crystal transformation in a eutectic system.

5.4 Mechanical alloying processes

Although mechanical alloying processes have been extensively investigated, the exact mechanism of the mechanical amorphization process is still under debate. The typical values of diffusion coefficients D for Cu and Ni in Zr at ambient temperature is approximately 10^{-22} m²/s, as extrapolated from high temperature diffusion data [Hood et al. 1970, 1972]. This means that essentially no atomic movement would be possible at room temperature. However, we have estimated from a simplified diffusion equation, $x = \sqrt{Dt}$, that the effective diffusion coefficient of Cu and Ni must be around 10^{-15} m²/s from the total diffusion time (20 seconds) and the effective diffusion distance (100 nm) of Cu and Ni in Zr. Therefore, the actual effective diffusion coefficient is 7 orders of magnitude higher than the room temperature diffusion coefficient. It is commonly accepted that diffusivities can be enhanced by several orders of magnitude by a large number of dislocation (pipe diffusion), vacancies and large grain boundary areas (grain boundary diffusivities are much higher than bulk diffusivities) produced by severe deformation. Therefore, it is proposed [Sagel et al. 1998] that the enhanced diffusion, due to the large density of structural defects, is based on a thermally activated atomic jump mechanism. However, it is found that the diffusion coefficient of Cu in α -Zr is around 10^{-15} m²/s at temperatures of about 400°C. Moreover, if we assumed that the mechanical alloying takes place by only thermal diffusion, then the effective local temperature of the sample must be increased to 400°C. However, the amorphous Cu-Zr sample crystallizes below 400°C to form stable intermetallic compounds. Hence, if the equivalent temperature increased to 400°C, then we should expect intermetallic compounds instead of an amorphous phase. Therefore, there must be some additional mechanism responsible for mechanical alloying. In 1995, Bellon et al. suggested that additional alloying is possible by nonequilibrium roughening of interface in crystals under shear when the strain rate is around 10^5 s⁻¹. But, in the present study we maintained a strain rate below 0.5 s⁻¹. Therefore, such mechanism can be applicable for ball milling but not for cold rolling. In this report, we propose a simple deformation model (schematically shown in Fig. 5.9) for mechanical alloying. In the process of repeated cold rolling, the previous rolling direction changes (as described in fig. 5.8) after each folding. As a result, the active slip systems change after each folding as shown in fig. 5.9. Due to the change of slip systems after each folding, the interfaces become rough i.e. Zigzag or wavy (Fig. 5.9b and c). Upon further deformation, clusters of atoms mix with each other (Fig. 5.9d) at the interface due to the random selection of the slip systems at the rough interface. Further deformation then causes atomic scale mixing (Fig. 5.9e) by the same mechanism. Due to the continuous atomic mixing, the crystalline solid solution at the interface transforms into the amorphous phase when the concentration of the solid solution exceeds a critical limit. In the amorphous zone further atomic mixing takes place due to shear deformation which is the only deformation mode of amorphous materials. Fig. 5.10 schematically shows the mechanism that is responsible for atomic mixing within the shear zone. During shear deformation, the atoms, whose large portion remains above the shear plane move away from the shear plane to the above of the shear plane and other atoms whose maximum volume remain below the shear plane move to the bottom direction. Since there are no defined atomic arrangements in the amorphous

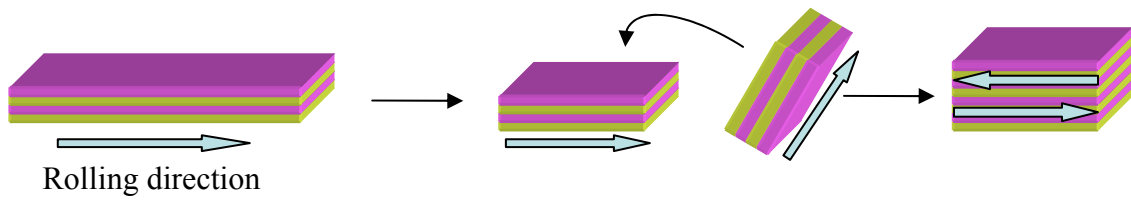


Figure 5.8: Schematic representation of the rolling and folding process. After each folding, previous rolling direction of the upper part of the sample become opposite to that of lower parts of the sample.

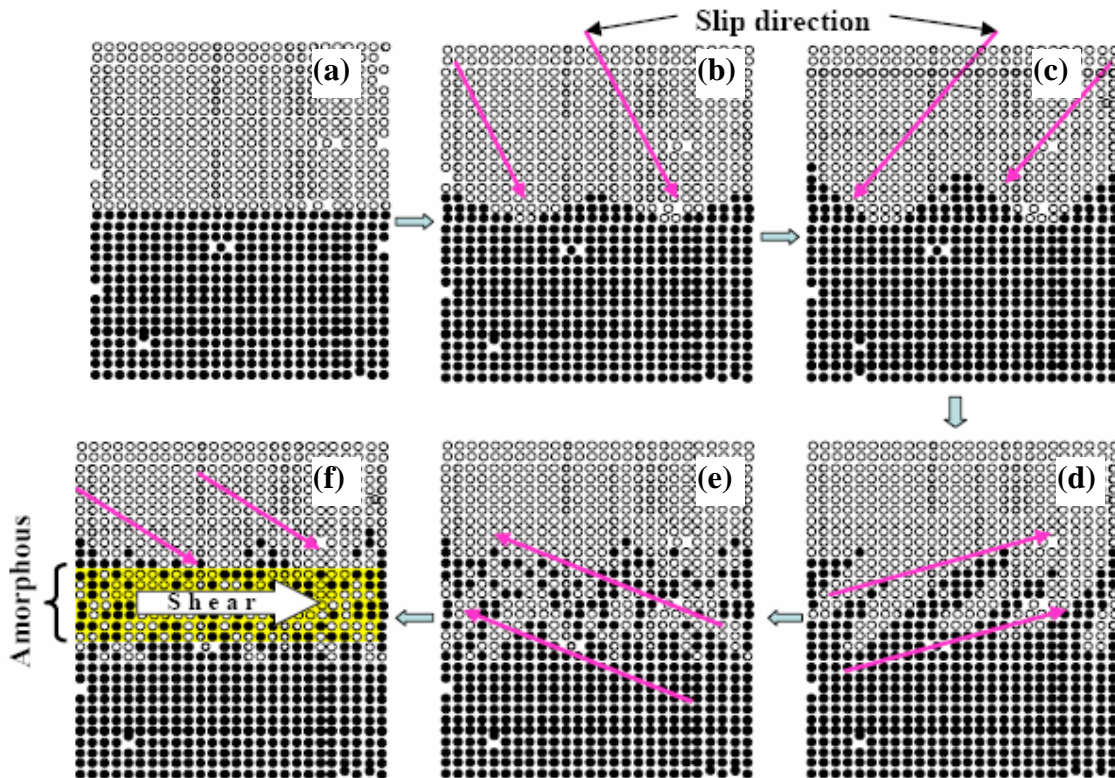


Figure 5.9: Schematic description of the mechanical alloying process due to the formation of rough interfaces during cold rolling.

phase, some atoms need to change their position (move above or below the slip plane) to form a glide plane along which shear deformation can proceed. Consequently, atomic mixing occurs due to the atomic movement from a glide plane to both the directions of the glide plane. We believed that during mechanical alloying at low temperature and low strain rate, atomic mixing mainly occurs by means of mechanical mixing of atoms by random slip (in crystalline phase) and by shear deformation in the amorphous phase which is schematically shown in Fig. 5.9. This phenomena can explain mechanical alloying of immiscible elements (i.e. systems with positive heat of mixing) for example Fe-Cu, Ag-Ni etc. On the other hand, large structural defect densities generated during plastic deformation can increase the effective diffusion coefficient of the elements. Therefore, thermally activated atomic diffusion is also possible during room temperature deformation in alloy systems with zero or negative heat of mixing.

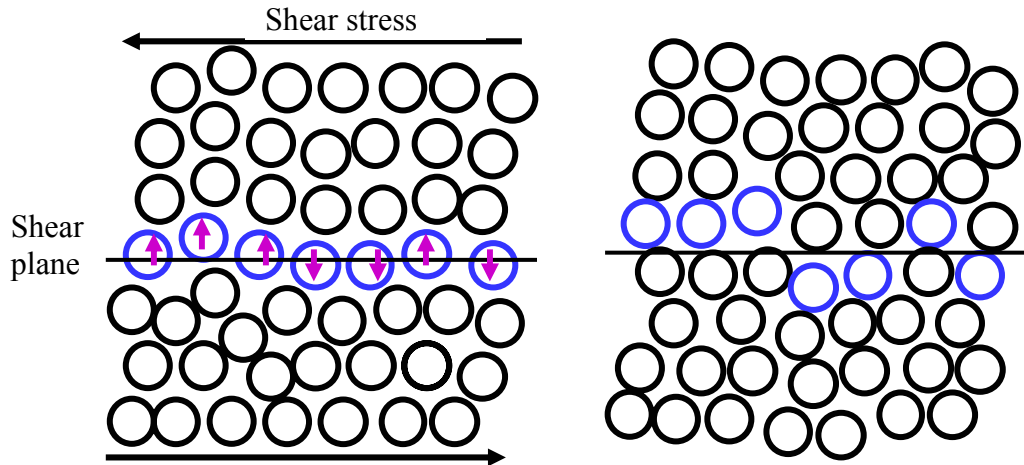


Figure 5.10: Schematic description of atomic mixing during shear deformation in the amorphous phase.

The progress of the solid state amorphization reaction at different stages of deformation are schematically shown in figure 5.11. At the beginning of the solid state reaction i.e., at low deformation levels, the amorphous phase initially forms at the interlayer interface of the multilayer as soon as alloying exceeds the critical value as explained earlier. After each F&R cycle the thickness of the alloying zone increased due to thermally activated atomic diffusion as well as mechanical mixing of the atoms by interface roughening and shearing of the amorphous layer during rolling. Gradually, the whole sample transforms completely to the amorphous state after severe deformation. The observation of a continuously increasing thickness of the amorphous interlayer at the heterophase interface with increasing strain indicates that the solid state amorphization reaction is diffusion controlled and – in a sense – proceeds similarly as any diffusional phase transformation with the exception that the material ahead of the “growth front” needs to attain a thermodynamically unstable state first, before it can transform.

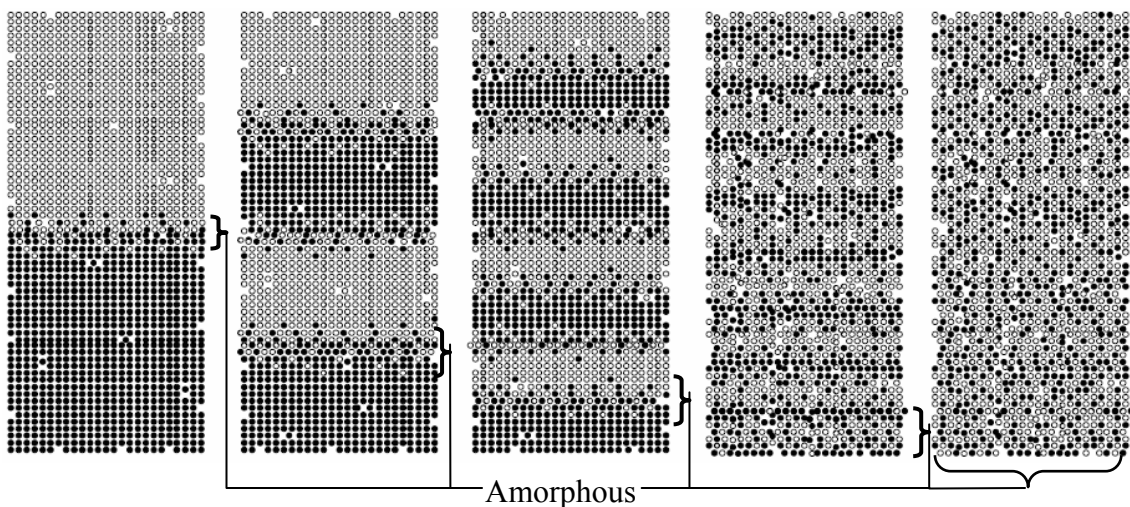


Figure 5.11: Schematic description of the solid state amorphization reaction during cold rolling.

5.5 Suppression of crystal nucleation in amorphous layers with sharp concentration gradients

The thermodynamic and kinetic aspects of the solid state amorphization reaction is described in detail in section 2.3. The usual thermodynamic analysis has shown that in solid-state amorphization the driving force for amorphous-alloy formation is smaller, at least, than that for the formation of some intermetallic compounds and it has suggested that the answer for this problem must lie in the kinetic constraints which restrict the nucleation of intermetallic compounds. However, the usual thermodynamic analysis has not considered the effects of concentration gradients occurring during the early stage of a solid-state amorphization. Desre' et al.(1990, 1991, 1996) suggested on the basis of thermodynamic arguments that sharp concentration gradients present during diffusive mixing facilitate amorphization in solid state reactions by reducing or even suppressing the driving force for crystallization.

Considering the effect of the concentration gradient ∇C on classical nucleation theory, the expression for the Gibbs free energy of nucleation of a compound embryo of dimensions $2r$ from an amorphous phase is approximately given as [Desre' et al. 1990]

$$\Delta G_N = 24\sigma r^2 + 8\rho\Delta G_{pc}(C^*)r^3 + \frac{4}{3}\rho\alpha(\nabla C)^2 r^5 \quad (5.1)$$

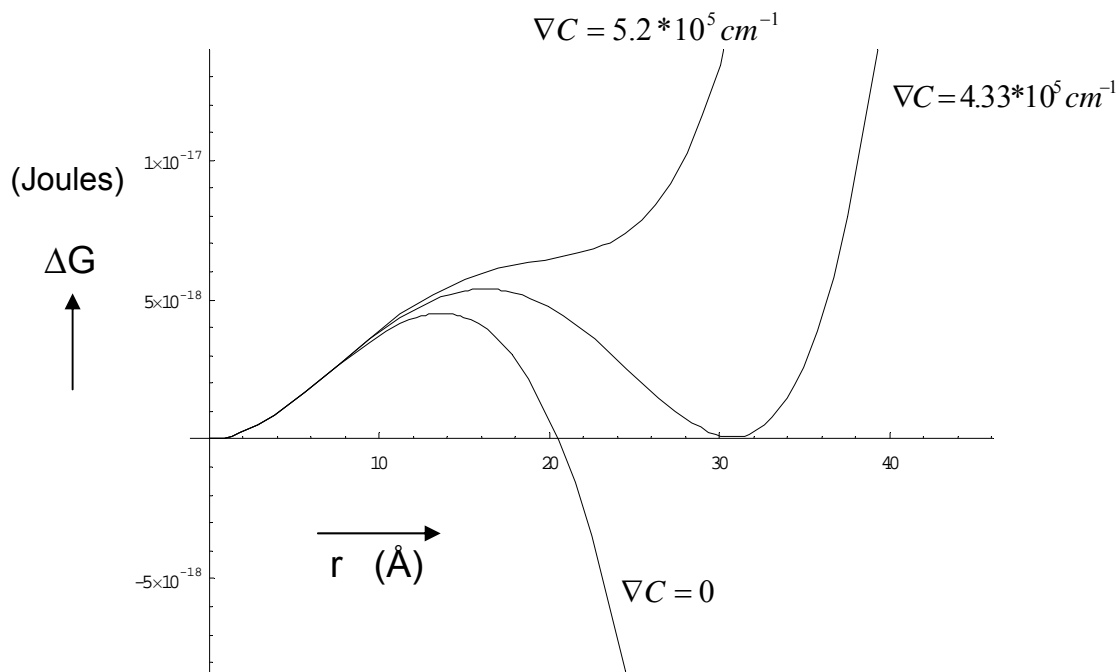


Figure 5.12: Gibbs energy of nucleation of a cubic compound with different concentration gradients ∇C .

Equation 5.1 is used to calculate the effective driving force for nucleation of the $\text{Cu}_{10}\text{Zr}_7$ intermetallic compound from an amorphous $\text{Cu}_{60}\text{Zr}_{40}$ layer under a concentration gradient ∇C . Figure 5.12 shows the influence of an increasingly sharp concentration gradient on ΔG_N for the case of $\text{Cu}_{10}\text{Zr}_7$, which is the equilibrium compound near $\text{Cu}_{60}\text{Zr}_{40}$ composition. From figure 5.12 it can be seen that for a critical gradient $\nabla C_c = 4.33 \cdot 10^5 \text{ cm}^{-1}$, no negative value of ΔG_N is obtained and the minimum is attained at $\Delta G_N = 0$. This implies that for $\nabla C > \nabla C_c$, no driving force is available for nucleation of $\text{Cu}_{10}\text{Zr}_7$. Furthermore, the minimum in $\Delta G_N(r)$ vs r no longer occurs in the ∇C range greater than $5.2 \cdot 10^5/\text{cm}$. Similar calculations also predict that above a critical concentration gradient of around $\nabla C_c = 10^5 \text{ cm}^{-1}$, no driving force is available to nucleate any intermetallic compound from a Ni-Zr amorphous phase. From TEM analysis (EDX line-scan measurements), we estimated that the concentration gradient developed perpendicular to the Cu-Zr interface after 40-F&R passes of a $\text{Cu}_{60}\text{Zr}_{40}$ sample varies between $1.5 \cdot 10^6$ to $2 \cdot 10^6$, which is much higher than the critical concentration gradient ($4.33 \cdot 10^5$) for nucleating an intermetallic compound from the Cu-Zr amorphous phase. In addition, the TEM analysis confirms the presence of an amorphous phase along Cu-Zr interface. Therefore, Desre' model is in good agreement to describe the formation/stability of the amorphous phase under sharp concentration gradients.

Chapter 6

Summary and Outlook

Repeated cold-rolling with intermediate folding presents a versatile and cost-effective alternative to conventional solid-state processing routes that can yield massive specimens of nanocrystalline and amorphous materials at ambient temperature. In previous work, the synthesis of bulk ultrafine-grained samples by severe plastic deformation was mostly limited to grain sizes larger than 100 nm. However, in the present investigations, bulk nanocrystalline samples of Ti and Zr consisting of grains considerably smaller than 100 nm in diameter could be synthesized. In fact, the grain size achieved in pure Ni is about 7–8 nm with a very narrow grain size distribution. It should be noted that the average grain sizes less than 10 nm in pure Ni have not been obtained by any other SPD technique. The comparison between hcp and fcc metals suggest that grain refinement by plastic deformation should proceed more efficiently in systems with a larger number of active slip systems. The formation of a nanocrystalline microstructure during intense cold rolling can be explained in terms of dislocation generation and rearrangement to form a cell- or subgrain structure followed by grain boundary sliding and grain rotation during further deformation, which are the most probable deformation mechanisms in extremely fine-grained nanocrystalline materials. On the basis of the present results, we propose that the main key to produce fine-grained nanocrystalline structures seems to be the requirement of a large plastic strain, which can produce more dislocations, but not necessarily involving a high applied hydrostatic pressure, as e.g. in high-pressure torsion straining. The more dislocations are produced and stored, the more grain boundaries can be built from them. This mechanism, and thus the minimum grain size, is limited by the minimum crystallite size that can accommodate a dislocation and by dynamic recovery that occurs concurrently during the deformation. Rolling of Zr at liquid nitrogen temperature supports this argument. At low working temperature, the dynamic recovery is reduced, which increases the equilibrium dislocation density, hence faster grain refinement is possible at low rolling temperature. Therefore, it should be noted that the lower the working temperature, the faster the grain refinement rates. These results further indicate that processing pathways that are adaptable to the generation of extremely large strain levels at low temperature might provide an efficient way to produce nanostructured materials in bulk quantities for advanced applications. In addition, sequentially combining different severe plastic deformation processes present an alternative route for nanostructure formation. First results on pure Ni indicate that the combination of cold-rolling with high pressure torsion resulted in massive, nanocrystalline materials without texture and with the highest hardness (~ 7 Gpa) observed for Ni. As an outlook of future work it is worth mentioning that combination of different severe plastic deformation (SPD) techniques with repeated cold-rolling offer a wide range of options for tailoring the microstructure and the shape and quantity of the product nanostructure and – at the same time – present a wide field yet to be explored.

In addition, repeated cold-rolling also allows for synthesizing bulk amorphous materials, which is attractive concerning the analyses of the basic underlying mechanisms of solid state amorphization. Specifically, the geometry of the elemental layers is highly defined compared to ball milled samples and the deformation proceeds at a comparatively low strain rate, which avoids increasing the temperature locally during processing as is commonly observed during ball milling. Fully amorphous samples of different binary $\text{Cu}_{60}\text{Zr}_{40}$, $\text{Ni}_{36}\text{Zr}_{64}$, ternary $\text{Ti}_{35}\text{Zr}_{10}\text{Cu}_{55}$ and quaternary $\text{Zr}_{65}\text{Al}_{7.5}\text{Cu}_{17.5}\text{Ni}_{10}$ and $\text{Ti}_{35}\text{Zr}_{10}\text{Cu}_{47}\text{Ni}_8$ elemental multilayers have been synthesized at ambient temperature by repeated cold-rolling. The main key for the amorphization to proceed seems forced atomic intermixing to achieve high values of supersaturation. Above the limit for polymorphic transformation, the supersaturated solid solution becomes unstable and transforms to an amorphous phase. In addition, sharp concentration gradients present during diffusion mixing facilitate amorphization in solid state reactions by reducing or suppressing the driving force for crystallization. The present experimental results indicate that during mechanical alloying at ambient temperature and low strain rate, atomic mixing mainly occurs by means of “mechanical” mixing of atoms by random slip (in the crystalline phase) and by shear deformation in the amorphous phase. At the beginning of the solid state reaction i.e., at low deformation levels, the amorphous phase initially forms at the interlayer interface of the multilayer as soon as alloying exceeds the critical value of supersaturation. After each F&R cycle the thickness of the alloying zone increases due to thermally activated atomic diffusion as well as to mechanical mixing of the atoms by interface roughening and shearing of the amorphous layer during rolling. Gradually, the whole sample transforms completely to the amorphous state after severe deformation. The observation of a continuously increasing thickness of the amorphous interlayer at the heterophase interface with increasing strain indicates that the solid state amorphization reaction is diffusion (thermally activated atomic diffusion combined with forced intermixing) controlled and – in a sense – proceeds similarly as any diffusional phase transformation with the exception that the material ahead of the “growth front” needs to attain a thermodynamically unstable state first, before it can transform. Recently, it has found that repeated cold-rolling represents a powerful technique to create supersaturated solid solution or even amorphous phase between immiscible elements. However, the exact mechanisms of the atomic level mixing of immiscible elements are poorly understood at present. Moreover, the properties of alloys of immiscible elements have not been studied systematically and present many opportunities for future research of the alloys created between immiscible elements.

Appendix

A.1. Estimation of the strain in High Pressure Torsion (HPT)

The principle of HPT processing is depicted schematically in Fig A.1. Figure A.1(b) shows the variables used in estimating the strain imposed in HPT where, for a small rotation, $d\theta$, and displacement, dl , it follows that $dl = rd\theta$, where r is the radius of the disk and the shear strain, $d\gamma$, is given by

$$\begin{aligned} d\gamma &= dl/h_0 \text{ where } h_0 \text{ is the disk thickness.} \\ &= rd\theta/h_0 \end{aligned}$$

The corresponding equivalent engineering strain is given as , $e = \frac{d\gamma}{\sqrt{3}}$.

Therefore, the true strain, $\varepsilon = \ln(1+e)$

$$= \ln\left(1 + \frac{rd\theta}{\sqrt{3}h_0}\right)$$

For one complete rotation, $\theta = 2\pi$, therefore, true strain is given by:

$$\varepsilon = \ln\left(1 + \frac{2\pi r}{\sqrt{3}h_0}\right) \quad (1)$$

2nd approach:

The true strain is given as, $\varepsilon = \ln\left(\frac{\text{final_length}}{\text{initial_length}}\right)$

$$\text{or, } \varepsilon = \ln\left(\frac{2\pi r}{h_0}\right) \quad (2)$$

because after one full rotation the vertical small metal slit, h_0 , becomes the periphery ($2\pi r$) of the disk. Therefore, the true strain of the disk ($h_0 = 0.3$ mm and $r = 5$ mm) after one rotation is 4.1 from equation (1) and 4.65 from equation (2).

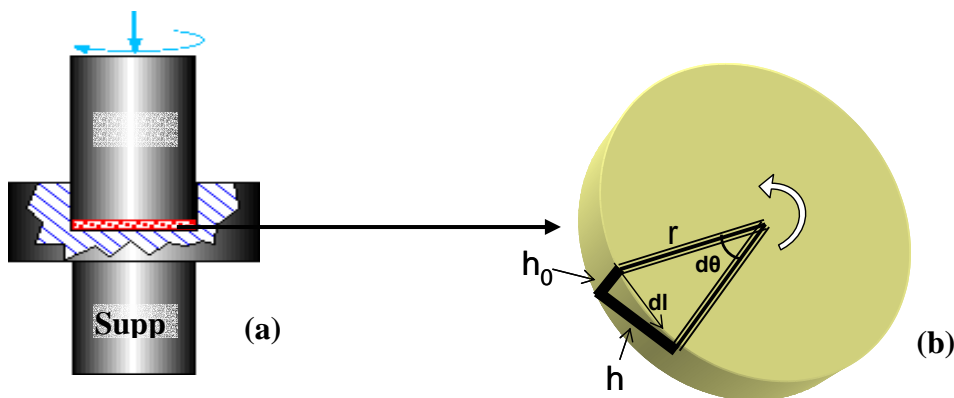


Figure A.1: Schematic diagram of the HPT process.

A.2. Estimation of the strain in Equal Channel Angular Pressing (ECAP)

The principle of ECAP is illustrated schematically in figure A.2, where two channels of equal cross-section intersect at an angle Φ . In Fig. A.2(b), a small element in the sample, initially a square in cross-section with dimension given by $abcd$, becomes deformed by shear on passage through the die into the configuration given by $a'b'c'd'$. Using the notation in Fig. A.2(b), it follows that the shear strain, γ , is given by $a'q/qd'$, where $qd' = ad$ and $ab' = dc' = a'p = pq = ad \cot(\Phi/2)$ so that $a'q = 2ad \cot(\Phi/2)$.

$$\text{Therefore, the shear strain, } \gamma = \frac{a'q}{qd'} = \frac{2ad \cot(\phi/2)}{ad}$$

$$\text{or, } \gamma = 2 \cot(\Phi/2)$$

$$\text{For } \Phi = 90^\circ, \gamma = 2.$$

$$\text{The equivalent engineering strain, } e = \frac{\gamma}{\sqrt{3}} = \frac{2}{\sqrt{3}}.$$

$$\begin{aligned} \text{The true strain, } \varepsilon &= \ln(1+e) \\ &= \ln(1+2/\sqrt{3}) \\ &= 0.77 \end{aligned}$$

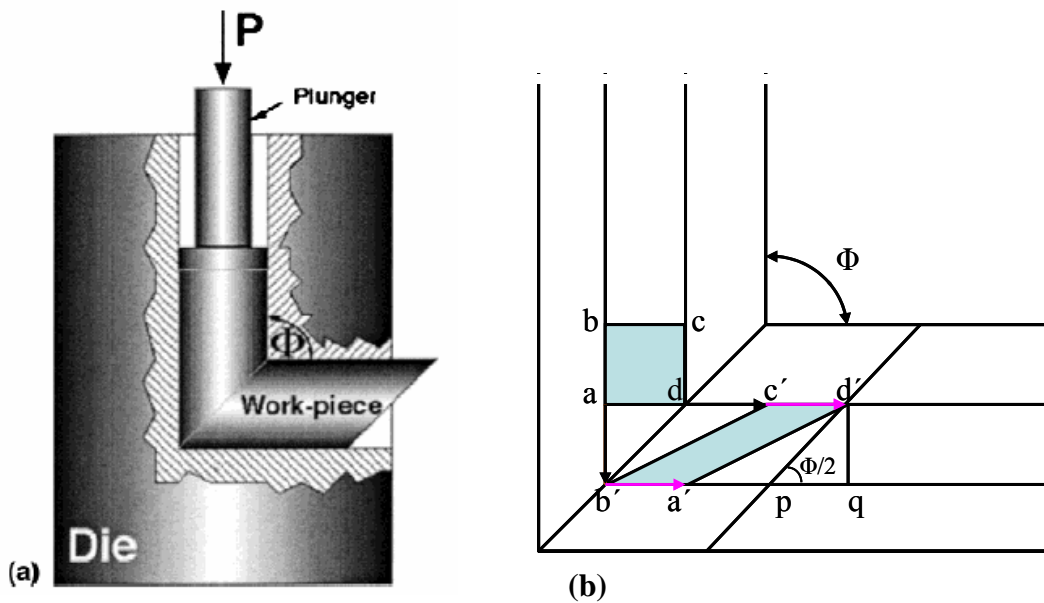


Figure A.2: Schematic illustration of an ECAP process.

2nd approach:

The true strain is defined as, $\varepsilon = \ln\left(\frac{\text{final_length}}{\text{initial_length}}\right)$

$$\begin{aligned} &= \ln(a'd'/ad) = \ln\left(\frac{\sqrt{(qd')^2 + (qa')^2}}{ad}\right) \\ &= \ln\left(\frac{\sqrt{(ad)^2 + (2pq)^2}}{ad}\right) = \ln\left(\frac{\sqrt{(ad)^2 + (2ad)^2}}{ad}\right) \text{ for } \Phi = 90^\circ. \\ &= \ln(\sqrt{5} ad/ad) \end{aligned}$$

Therefore, $\varepsilon = \ln(\sqrt{5} ad/ad) = 0.8$.

A.3. Strain in the rolling and folding (F&R) process

The cold-rolling process is schematically illustrated in Fig. A.3. The multilayer sample is gradually reduced to 50% of its initial thickness, t , by 10 subsequent passes and then the sample was cut in two halves and folded. Assuming the von Mises yield criteria and plane strain conditions, i.e. no lateral spreading, the true plastic strain after one folding is expressed by:

$$\varepsilon = \frac{2}{\sqrt{3}} \ln\left(\frac{t/2}{t}\right)$$

$$\text{or, } \varepsilon = \frac{2}{\sqrt{3}} \ln\left(\frac{1}{2}\right) = 0.8$$

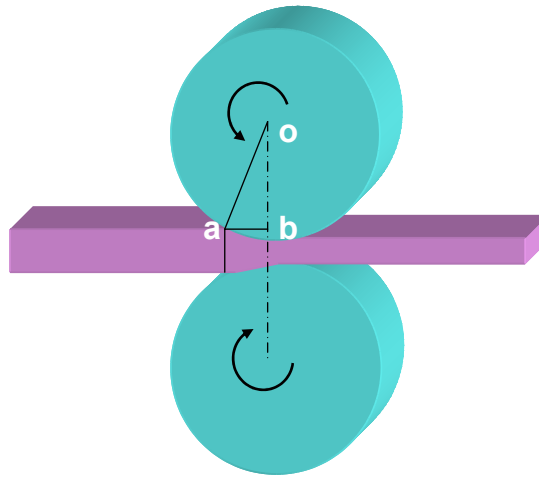


Figure A.3: A schematic representation of the cold-rolling process.

Strain rate:

The deformation time and strain rate were calculated from the geometry and the roll velocity. Diameter of the roll = 150 mm.

Circumferential roll velocity = 16.7 mm/s.

In figure 3, radius of the roll, $OA = 75$ mm.

$$OB = 75 - \frac{1}{2} * (\text{thickness reduction})$$

$$= 75 - 0.1 = 74.9 \text{ mm}$$

Hence, $AB = 3.87$ mm.

The time of deformation = $3.87/16.7 = 0.2322$ sec.

Since total 50% deformation takes place by 10 subsequent passes, therefore, the true

strain rate is given as, $\dot{\varepsilon} = \frac{0.8}{0.2322 * 10} = 0.344 \text{ s}^{-1}$

References

- [1] Atzmon M, Veerhoeven JR, Gibson ER, Johnson WL, *Appl. Phys. Lett.* 45 (1984) 1052.
- [2] Atzmon M, Unruh KM, Johnson WL, *J. Appl. Phys.* 58 (1985) 3865.
- [3] Bellon P, Averback RS, *Phys. Rev. Lett.* 74 (1995) 1819.
- [4] Bordeaux F, Yavari R, *Z. Metallkde.* 81 (1990) 130.
- [5] Carter CB, Holmes SM, *Phil. Mag.* 35 (1977) 1161.
- [6] Cerezo A, Godfrey TJ, Smith GDW, *Rev. Sci. Instrum.* 59 (1988) 862.
- [7] Chen YG, Liu BX, *Appl. Phys. Lett.* 68 (1996) 3096.
- [8] Chokshi AH, Rosen A, Karch J, Gleiter H, *Scripta Metall.* 23 (1989) 1679.
- [9] Clemens BM, *Phys. Rev. B* 33 (1986) 7615.
- [10] Torre FD, Swygenhoven HV, Victoria M, *Acta Mater.* 50 (2002) 3957.
- [11] Desré PJ, Yavari R, *Phys. Rev. Lett.* 64 (1990) 1533.
- [12] Desré PJ, *Acta Metall. Mater.* 39 (1991) 2309.
- [13] Desré PJ, Hodaj F, *Acta Mater.* 44 (1996) 4485.
- [14] Dieter GE, "Mechanical Metallurgy", SI Metric Edition, McGraw-Hill, London-New York (1988) p.174.
- [15] Dinda GP, Rösner H, Wilde G, *Ultrafine Grained Materials III*, Edited by YT Zhu et al., TMS 2004, pp. 309-314.
- [16] Dinda GP, Rösner H, Wilde G, *Scripta Mater.* 52 (2005) 577.
- [17] Dinda GP, Rösner H, Wilde G, *Solid State Phenomena* 101-102 (2005a) 55.
- [18] Dinda GP, Rösner H, Wilde G, *Mater. Sci. Eng. A*, 410-411 (2005) 328.
- [19] Dinda GP, Rösner H, Wilde G, *J. Non. Cryst. Solids*, in press.
- [20] Ebrahimi F, Bourne GR, Kelly MS, Matthews TE, *Nanost. Mater.* 11 (1999) 343.
- [21] El-Sharik AM, Erb U, Palumbo G, Aust KT, *Scripta Metall. Mater.* 27 (1992) 1185.
- [22] Erb U, *Nanost. Mater.* 6 (1995) 533.
- [23] Gertsman VY, Hoffmann M, Gleiter H, Birringer R, *Acta Metall. Mater.* 42 (1994) 3539.
- [24] Gleiter H, *Prog. Mater. Sci.* 33 (1989) 223.
- [25] Gleiter H, *Acta Mater.* 48 (2000) 1.
- [26] Grigoriev IS, *Handbook of physical quantities*, CRC Press, (1997).
- [27] Hahn H., Mondal P, Padmanabhan KA, *Nanostruc. Mater.* 9 (1997) 603.
- [28] He G, Eckert J, Loser W, Schultz L, *Nature Mater.* 2 (2003) 33.
- [29] He Y, Poon SJ, Shiflet GJ. *Science* 241 (1998) 1640.
- [30] Hellstern E, Schultz L, *Appl. Phys. Lett.* 48 (1986) 124.
- [31] Hellstern E, Schultz L, *Mater. Sci. Eng.* 93 (1987) 213.
- [32] Hirth JP, Lothe J, *Theory of dislocations*, Krieger Publishing Company, Malabar, FL (1992).
- [33] Hood GM, *Diffusion Processes*, edited by Sherwood et al., (London: Gordon & Breach), (1970) p. 361.
- [34] Hood GM, Schultz RJ, *Scripta metall.* 41 (1972) 329.
- [35] Hono K, *Prog. Met. Sci.* 47 (2002) 621.

- [36] Hu EL, Shaw DT, In: Nanostructure Science and Technology, ed. by RW Siegel (1999).
- [37] Hu EL, Roco MC (Kluwer Academic Publ: Dordrecht, 1999), p. 15.
- [38] Hughes GD, Smith SD, Pande CS, Johnson HR, Armstrong RW, Scripta Metall. 20 (1986) 93.
- [39] Hughes DA, Hansen N, Acta Mater. 48 (2000) 2985.
- [40] Huang X, Tsuji N, Hansen N, Minamino Y, Mater. Sci. Eng. A340 (2003) 265.
- [41] Inoue A, Zhang T, Masumoto T, Mater. Trans. JIM 31 (1990) 177.
- [42] Inoue A, Zhang T, Masumoto T, Mater. Trans. JIM 31 (1990a) 425.
- [43] Inoue A, Masumoto T, Mater. Sci. Eng. A173 (1993) 1.
- [44] Kim JJ, Choi Y, Suresh S, Argon AS, Science 295 (2002) 654.
- [45] Klement W, Willens RH, Duwez P, Nature 187 (1960) 869.
- [46] Koch CC. Nanostruct. Mater. 9 (1997) 13.
- [47] Kui HW, Greer AL, Turnbull D, Appl. Phys. Lett. 45 (1984) 615.
- [48] Kwak JS, Chi EJ, Choi JD, Park SW, Naik HK, So MG, Lee SM, J. Apl. Phys. 78 (1995) 983.
- [49] Lee JC, Seok HK, Suh JY, Acta Mater. 50 (2002) 4005.
- [50] Liebermann HH, editor. Rapidly solidified alloys: Processes, structures, properties, applications. New York, Marcel Dekker, 1993.
- [51] Liu BX, Zhang ZJ, Jin O, Pan F, MRS Proc. 396 (1996) 71.
- [52] Lu L, Li SX, Scripta Mater. 45 (2001) 1163.
- [53] Lund AC, Schuh CA, Appl. Phys. Lett. 82 (2003) 2017.
- [54] Lund AC, Schuh CA, Acta Mater. 52 (2004) 2123.
- [55] Markmann J, Bunzel P, Rosner H, Liu KW, Padmanabhan KA, Birringer R, Gleiter H, Weissmüller J, Scripta Mater. 49 (2003) 637.
- [56] McFadden SX, Mishra RS, Valiev RZ, Zhilyaev AP, Mukherjee AK, Nature 398 (1999) 684.
- [57] Meng WJ, Nieh CW, Johnson WL, Appl. Phys. Lett. 51 (1987) 1693.
- [58] Neishi K, Horita Z, Langdon TG, Mater. Sci. Eng. A325 (2002) 54.
- [59] Ovidko LA, Science 295 (2002) 2386.
- [60] Padmanabhan KA, Dinda GP, Hahn H, Gleiter H, Scripta Mater. submitted.
- [61] Pan F, Chen YG, Liu BX, Appl. Phys. Lett. 67 (1995) 780.
- [62] Peker A, Johnson WL, Appl. Phys. Lett. 63 (1993) 2342.
- [63] Phillpot SR, Wolf D, Gleiter H, Scripta Metall. Mater. 33 (1995) 1245.
- [64] Raab GJ, Valiev RZ, Lowe TC, Zhu T, Mater. Sci. Engg. A382 (2004) 30.
- [65] Rosner H, Markmann J, Weissmuller J, Phil. Mag. Lett. 84 (2004) 321.
- [66] Sagel A, Sieber H, Fecht HJ, Perepezko JH, Acta Mater. 46 (1998) 4233.
- [67] Saito Y, Tsuji N, Utsunomiya H, Sakai T, Hong RG, Scripta Mater. 39 (1998) 1221.
- [68] Saito Y, Utsunomiya H, Suzuki H, Sakai T, Scripta Mater. 42 (2000) 1139.
- [69] Sanders PG, Eastman JA, Weertman JR, Acta Mater. 45 (1997) 4019.
- [70] Saunders N, Miodownik AP, J. Mater. Res. 1 (1986) 38.
- [71] Sauvage X, Wetscher F, Pareige P, Acta Mater. 53 (2005) 2135.
- [72] Schiotz J, DiTolla FD, Jacobsen KW, Nature 391 (1998) 561.
- [73] Schiotz J, Verge T, DiTolla FD, Jacobsen KW, Phys. Rev. B60 (1999) 1971.
- [74] Schiotz J, Jacobsen KW, Science 301 (2003) 1357.

- [75] Schröder H, Samwer K, Phys. Rev. Lett. 54 (1985) 197.
- [76] Schwarz RB, Johnson WL, Phys. Rev. Lett. 51 (1983) 415.
- [77] Schwarz RB, Koch CC, Appl. Phys. Lett. 49 (1986) 146.
- [78] Schwarz RB, Rubin JB. J Alloys and Compounds 194 (1993) 189.
- [79] Segal VM, Reznikov VI, Drobyshevskij AE, Kopylov VI, Metally 1 (1981) 115.
- [80] Sheng HW, Wilde G, Ma E, Acta Mater. 50 (2002) 475.
- [81] Smirnova NA, Levit VI, Pilyugin VI, Kuznetsov RI, Davydova LS, Sazonova VA, Fiz. Met. Metalloved 61 (1986) 1170.
- [82] Suryanarayana C, editor. Non-equilibrium processing of materials. Oxford: Pergamon Press, (1999).
- [83] Swygenhoven HV, Science 296 (2002) 66.
- [84] Swygenhoven HV, Derlet PM, Froseth AG, Nature Materials 3 (2004) 399.
- [85] Valiev RZ, Krasilnikov NA, Tsenev NK, Mater. Sci. Engg. A137 (1991) 35.
- [86] Valiev RZ, Korznikov AV, Mulyukov RR, Mater. Sci. Engg. A168 (1993) 141.
- [87] Valiev RZ, Islamgaliev RK, Alexandrov IV, Prog. Mater. Sci. 45 (2000) 103.
- [88] Valiev RZ, Nature Mater. 3 (2004) 511.
- [89] Wang Y, Chen M, Zhou F, Ma E, Nature 419 (2002) 912.
- [90] Warren BE, X-ray diffraction, New York: Dover (1990).
- [91] Weissmuller J, Markmann J, Adv. Eng. Mat. 7 (2005) 202.
- [92] Wilde G, Görler GP, Willnecker R, Dietz G, Appl. Phys. Lett. 65 (1994) 397.
- [93] Wilde G, Sieber H, Perepezko JH, Scripta Mater. 40 (1999) 779.
- [94] Wilde G, Sieber H, Perepezko JH, J. Non.Cryst. Solids 250-252 (1999) 621.
- [95] Wilde G, Boucharat N, Hebert RJ, Rosner H, Tong WS, Perepezko JH, Adv. Engr. Mat. 5 (2003) 125.
- [96] Wilde G, Dinda GP, Rösner H, Adv. Eng. Mat. 7 (2005) 11.
- [97] Wilde G, Boucharat N, Dinda GP, Hebert RJ, Rösner H, Valiev RZ, Mater. Sci. Forum 503-504 (2006) 425.
- [98] Yamakov V, Wolf D, Phillpot SR, Mukherjee AK, Gleiter H, Nature Mater. 1 (2002) 45.
- [99] Yamakov V, Wolf D, Phillpot SR, Gleiter H, Acta Mater. 50 (2002a) 61.
- [100] Yamakov V, Wolf D, Phillpot SR, Mukherjee AK, Gleiter H, Phil. Mag. Lett. 83 (2003) 385.
- [101] Yamakov V, Wolf D, Phillpot SR, Mukherjee AK, Gleiter H, Nature Mater. 3 (2004) 43.
- [102] Zhang ZJ, Liu BX, J. Appl. Phys. 76 (1994) 3351.
- [103] Zehetbauer MJ, Stüwe HP, Vorhauer A, Schafner E, Kohout J, Adv. Engr. Mat. 5 (2003) 330.
- [104] Zheng Y, Phys. Rev. B45 (1992) 7451.
- [105] Zhilyaev AP, Lee S, Nurislamova GV, Valiev RZ, Langdon TG, Scripta Mater. 44 (2001) 2753.
- [106] Zhorin VA, Shashkin DP, Yenikopyan NS, DAN SSSR 278 (1984) 144.
- [107] Zhou F, Liao XZ, Zhu YT, Dallek S, Lavernia EJ, Acta Mater. 51 (2003) 2777.